Electronic Transport Properties of Highly Doped Layered Semiconductors and Their Heterostructures

高濃度にドープされた層状半導体およびそのヘテロ構造の

電子輸送特性（英文）

Hiroto Ogura

小倉　宏斗

Department of Physics, Graduate School of Science,
Tokyo Metropolitan University

2023

Contents

Chapter 1: Introduction..1

1.1 Pn junction 1

1.2 Tunnel diodes 2

1.3 Tunneling field effect transistors (TFETs) 3

1.4 Transition Metal Dichalcogenides 7

1.5 Carrier Doping of TMDCs 9

1.6 Vertical Heterostructures of TMDCs 12

1.7 In-Plane Heterostructures of TMDCs.. 14

1.8 Purposes 18

Chapter 2: Experimental Methods 19

2.1 Mechanical Exfoliation 19

2.2 Chemical Vapor Deposition (CVD) 19

2.3 Photolithography 20

2.4 Plasma Etching 23

2.5 Electrical Measurement 24

Chapter 3: Multilayer In-Plane Heterostructures Based on Transition Metal Dichalcogenides for Advanced Electronics..............................26

3.1 Introduction 26

3.2 Experimental Methods 27

3.3 Results and Discussions 29

3.3.1 Multilayer WSe_2/MoS_2 Heterostructures. 29

3.3.2 Multilayer $Nb_xMo_{1-x}S_2/MoS_2$ Heterostructures. 39

3.4 Conclusions 55

Chapter 4: Air-Stable and Efficient Electron Doping of Monolayer MoS_2 by Salt–Crown Ether Treatment 56

4.1 Introduction 56

4.2 Experimental Methods 57

4.3 Results and Discussions 59

4.4 Conclusions 68

Chapter 5: Conclusions 70

Acknowledgements 71

References 73

List of Publications 85

Chapter 1:

Introduction

1.1 Pn Junction

A pn junction which is formed by connecting p-type and n-type semiconductors is the most conventional structure for semiconductor devices.[1] Figure 1.1a shows schematic images of non-degenerate p-type and n-type semiconductors with their band structures. For p-type semiconductors, the Fermi level (E_F) is close to the valence band maximum (VBM; E_v). In contrast, for n-type semiconductors, E_F is close to the conduction band minimum (CBM; E_c). After the construction of a p-n junction (Figure 1.1b), hole (electron) carriers diffuse from p-type (n-type) to n-type (p-type) semiconductors due to the carrier concentration gradient. Donor and acceptor ions are thus formed, which produces a built-in electric field in the depletion region. It is noted that E_F of p- and n-type semiconductors lies at the same energy level at equilibrium. This p-n junction exhibits rectifying current-voltage (I-V) characteristics as shown in Figure 1.1c. Figure 1.1d shows band diagrams of a pn junction for forward and reverse bias. Under forward bias, the built-in potential decreases, and current is based on carrier diffusion and recombination. Under reverse bias, the built-in potential increases, and the current is lower than that under forward bias because the carrier transport is based on minority carrier diffusion and carrier generation. The transport properties of a pn junction can be described by the following Shockley diode equation.

$$I = I_s \left\{ exp\left(\frac{qV}{\eta k_B T}\right) - 1 \right\} \tag{1.1}$$

Here, I_s is the reverse bias saturation current, η is the ideality factor, and T is the temperature. q and k_B are constants, the elementary charge and Boltzmann constant, respectively. The quality of pn junctions can be discussed by the ideality factor η at low-voltage forward bias. In a conventional pn junction, η varies from 1 to 2. For $\eta = 1$, diffusion current is dominant which is the ideal diode property. In contrast, for $\eta = 2$, the recombination current component is dominant.

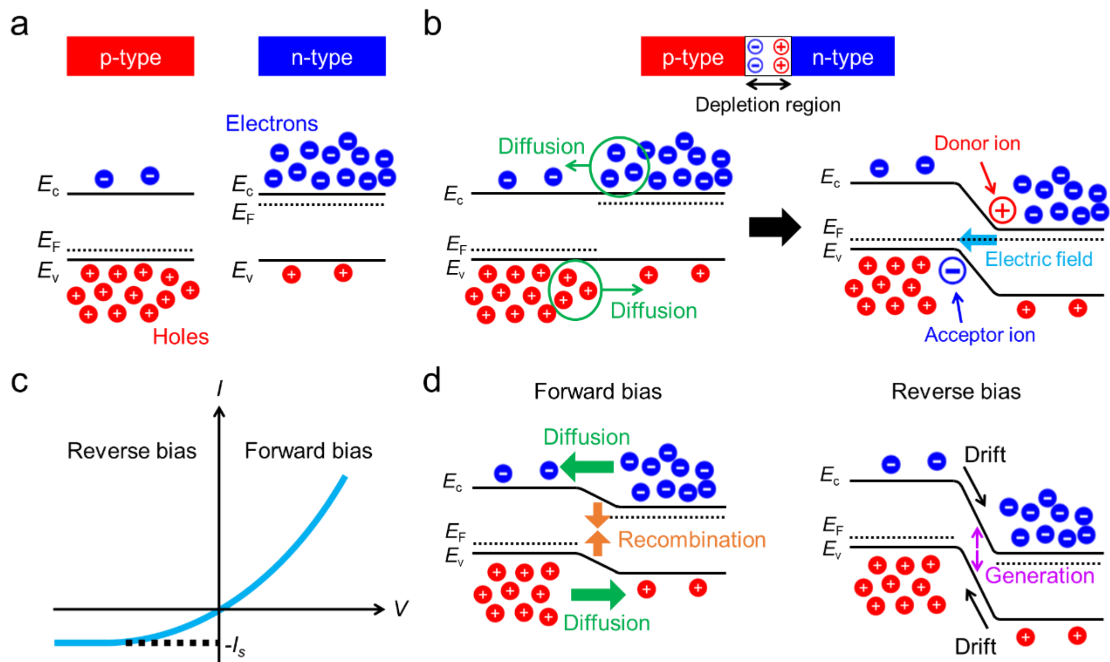

Figure 1.1 (a) Individual p- and n-type semiconductors and their energy bands. (b) P-n junction and its energy band before and after reaching equilibrium. (c) I-V curve of a pn junction. (d) Band diagrams of a pn junction under forward and reverse bias.

1.2 Tunnel Diodes

For degenerate semiconductors, E_F is located inside the valence band (conduction band) due to high-concentration hole (electron) doping. Pn junctions with such degenerate semiconductors are tunnel diodes, which exhibit tunneling current and negative differential resistance (NDR) based on a broken gap band alignment. Such tunnel diodes were firstly demonstrated by Esaki in 1958 [2] and have been actively studied since then. Figure 1.2 shows an I-V curve and band diagrams of conventional tunnel diodes. At equilibrium ($V = 0$ V), the band alignment is a broken gap (type III) with an overlap between the valence band of the p-type semiconductor and conduction band of the n-type semiconductor. Under a small forward bias ($0 < V < V_p$), electrons in the conduction band of the n-type semiconductor tunnel to the empty states in the valence band of the p-type semiconductor. For $V = V_p$, this tunneling current reaches its peak with a maximal overlap between the occupied conduction band states and unoccupied valence band states. Further increases in voltage lead to decreases in the tunneling current because the overlap region is reduced. After reaching the valley of the NDR, the current increases with the voltage again due to the transition from the tunneling current to the diffusion current. Under reverse bias, electrons tunnel from the filled valence band states of the p-type semiconductor to the empty conduction band states of the n-type semiconductor. These I-V characteristics can be described by the

following equation.

$$I = I_p \left(\frac{V}{V_p}\right) exp\left(1 - \frac{V}{V_p}\right) + I_0 exp\left(\frac{qV}{k_B T}\right) \tag{1.2}$$

Here, I_p is the peak current of the NDR at $V = V_p$. The first and second terms in this equation represent the tunneling current and diffusion current, respectively.

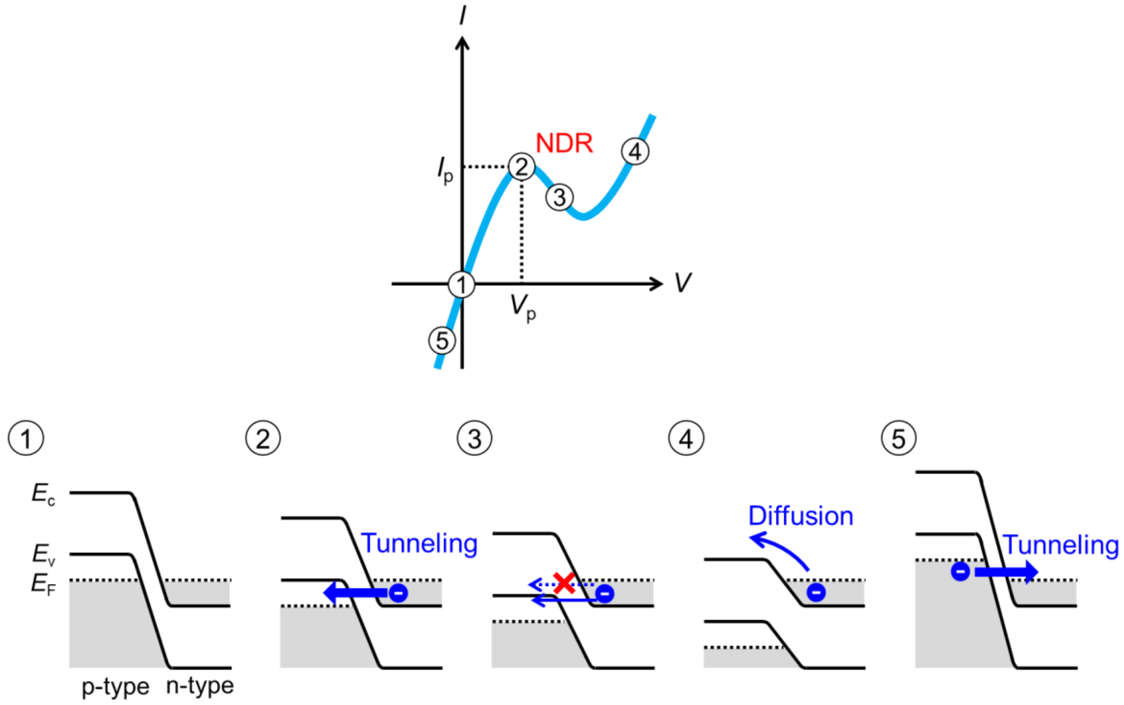

Figure 1.2 I-V curve and band diagrams of conventional tunnel diodes

1.3 Tunneling Field Effect Transistors (TFETs)

Tunneling field-effect transistors (TFETs) are the other device applications based on electron tunneling and a broken gap (type III) band alignment.

The most conventional FETs are metal-oxide-semiconductor FETs (MOSFETs). Figure 1.3a shows the device structure and band diagrams of an n-type MOSFET. The n-type MOSFET is composed of n-type source/drain, a p-type channel, and a gate electrode. The MOSFET can switch ON/OFF states by application of a gate voltage (V_g). In the OFF state, the drain current (I_d) cannot flow due to the large band offset between the source and channel. In the ON state, electrons can diffuse from the source to the channel due to shrinkage of the band offset by V_g.

TFETs can also switch ON/OFF states by application of V_g, however, I_d is dominated by electron tunneling. Figure 1.3b shows the structure and band diagrams of an n-type TFET. The n-type TFET consists of a p-type source, an intrinsic channel, an n-type drain, and a gate electrode. In the OFF state, electrons cannot move from the source to the channel. In the ON state, electrons

can tunnel from the valence band of the source to the conduction band of the channel due to the formation of a broken-gap band alignment by the application of V_g.

The gate tunability of FETs is defined by subthreshold swing (SS), i.e., the gate voltage required to increase the drain current by one order of magnitude.

$$SS = \frac{dV_g}{d(\log_{10} I_d)} \tag{1.3}$$

For conventional MOSFETs, SS can be described by the following equation.

$$SS \geq \ln(10)\frac{k_B T}{q} \tag{1.4}$$

Equation (1.4) is derived from the thermal carrier emission and Boltzmann distribution as follows.[3] As shown in Figure 1.3c, before application of a gate voltage, the barrier height between the source and channel is H, and the total drain current is $I_0 + I_{tunnel1} + I_{tunnel2}$, where I_0 is the thermionic emission current and $I_{tunnel1}$ and $I_{tunnel2}$ are tunneling currents through the barrier. Assuming the best electrostatics, the barrier height is H-ΔV_g at a gate voltage of ΔV_g and the thermionic emission current is described by $I_0 e^{\frac{q\Delta V_g}{k_B T}}$, where k_B is the Boltzmann constant and T is the temperature. Therefore, the total drain current is $I_0 e^{\frac{q\Delta V_g}{k_B T}} + I_{tunnel2}$ after application of a gate voltage. SS can be expressed as

$$SS = \frac{dV_g}{d(\log_{10} I_d)} = \frac{\Delta V_g}{\log_{10}\left(\frac{I_0 e^{\frac{q\Delta V_g}{k_B T}} + I_{tunnel2}}{I_0 + I_{tunnel1} + I_{tunnel2}}\right)} \tag{1.5}$$

Due to

$$\frac{I_0 e^{\frac{q\Delta V_g}{k_B T}} + I_{tunnel2}}{I_0 + I_{tunnel1} + I_{tunnel2}} < \frac{I_0 e^{\frac{q\Delta V_g}{k_B T}}}{I_0} \tag{1.6}$$

we can obtain

$$SS = \frac{\Delta V_g}{\log_{10}\left(\frac{I_0 e^{\frac{q\Delta V_g}{k_B T}} + I_{tunnel2}}{I_0 + I_{tunnel1} + I_{tunnel2}}\right)} > \frac{\Delta V_g}{\log_{10}\left(\frac{I_0 e^{\frac{q\Delta V_g}{k_B T}}}{I_0}\right)}$$

$$= \frac{\ln(10)\,\Delta V_g}{\ln\left(\frac{I_0 e^{\frac{q\Delta V_g}{k_B T}}}{I_0}\right)}$$

$$= \frac{\ln(10)\,\Delta V_g}{\ln\left(e^{\frac{q\Delta V_g}{k_B T}}\right)}$$

$$= \frac{\ln(10)\,\Delta V_g}{\frac{q\Delta V_g}{k_B T}}$$

$$= \ln(10)\frac{k_B T}{q} \qquad (1.7)$$

The fundamental SS limit of MOSFETs is estimated from this equation to be 60 mV dec^{-1} at 300 K. In contrast, TFETs can break through the 60 mV dec^{-1} limit as shown in Figure 1.3d because the carrier transport is derived from electron tunneling.

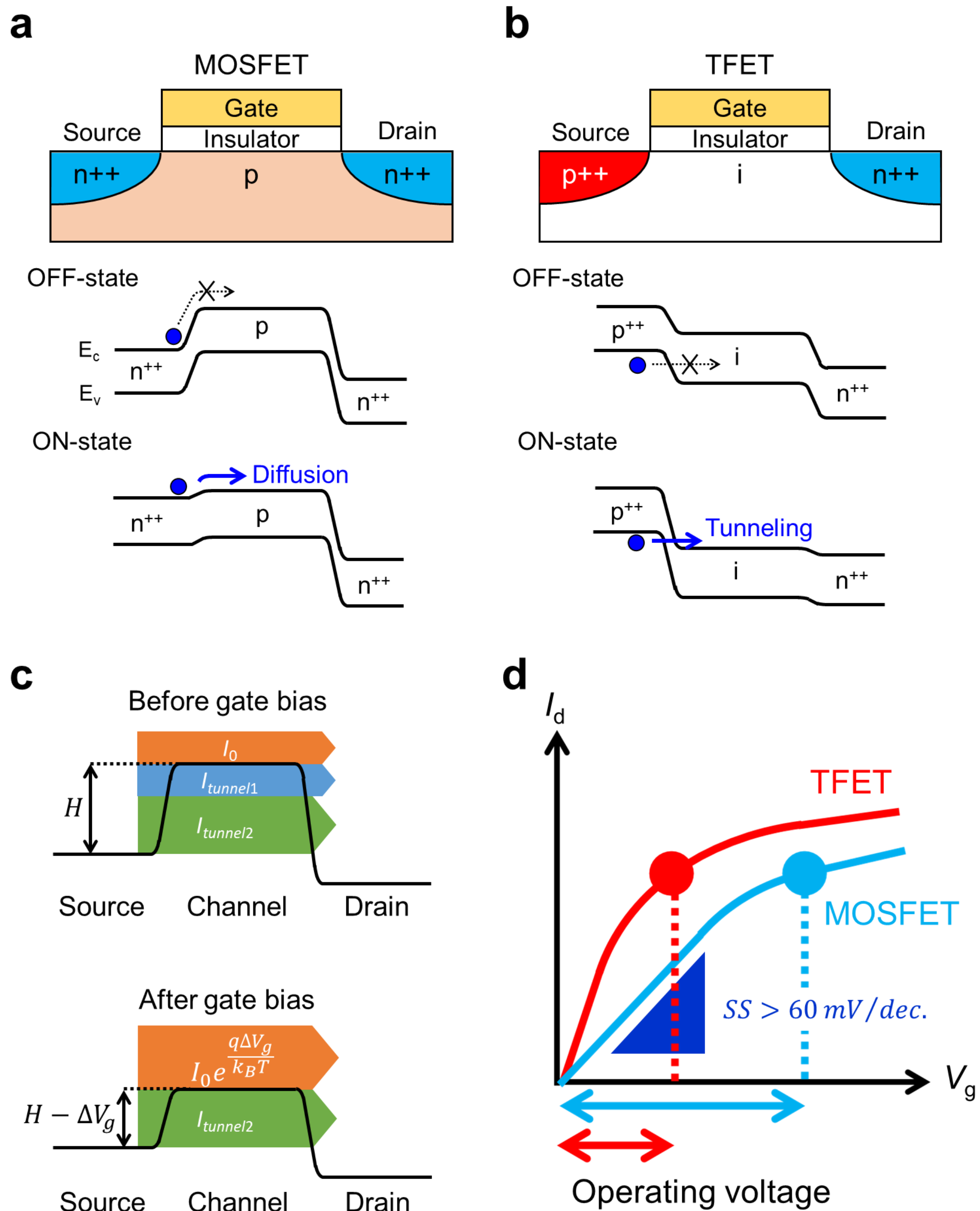

Figure 1.3 Structures and band diagrams of n-type (a) MOSFETs and (b) TFETs. (c) Band diagrams and transport characteristics of a MOSFET before and after application of a gate voltage (ΔV_g). (d) I_d-V_g curves for n-type MOSFETs and TFETs.

The mechanism of SS < 60mV dec^{-1} can be explained by the energy filtering effect of the Fermi distribution.[4-6] Figure 1.4 shows detailed band diagrams of an n-type TFET for the OFF state and ON state. In the OFF state, electrons cannot tunnel because the VBM of the source is

located below the CBM of the channel. The energy band of the channel is downshifted by application of a positive gate voltage. In the ON state, electrons can tunnel from the filled valence band states of the source to the empty conduction band states of the channel. The electrons that can contribute to tunneling current are distributed only in a small energy window $\Delta\phi$. In other words, the Fermi distribution of the electron carriers from the source is cut off. This energy filtering effect makes it possible to realize SS < 60mV dec^{-1}.

To achieve high-performance TFETs, it is essential to explore alternative semiconductor materials and high-concentration doping.

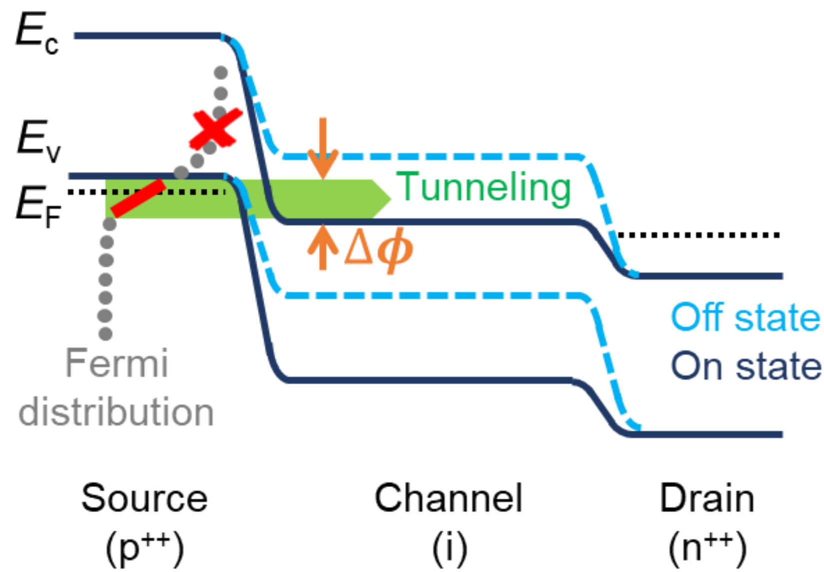

Figure 1.4 Schematic band diagram for the off- and on-states in an n-type TFET. The gray circles and red line in the source region indicate the Fermi-Dirac distribution.

1.4 Transition Metal Dichalcogenides

In recent years, transition metal dichalcogenides (TMDCs) have attracted much attention as new components for electronic and optoelectronic devices due to their layered dangling-bond-free structures with scalability down to atomic thickness and promising semiconducting properties.[7-15] Figure 1.5 shows schematic images of monolayer and multilayer TMDCs. For monolayers, the structures are composed of one transition metal layer sandwiched between two chalcogen layers with covalent bonding. Multilayer TMDCs are formed by vertical stacking of monolayers via van der Waals (vdW) interactions. The structures can be summarized by the chemical formula MX_2, where M is a transition metal and X is a chalcogen. TMDCs exhibit various electronic states depending on the chemical composition and thickness.[16] In particular, much effort has been devoted to investigate group-6 TMDCs, such as MoS_2 and WSe_2, and to elucidate their semiconducting properties, such as the high on/off current ratio, high mobility, and

direct/indirect bandgap nature.

Figure 1.6 shows the history of the previous studies on TMDCs. In the 1950s, bulk TMDCs were studied with respect to their lubricating functions and tuning of the properties by intercalation.[17, 18] In 2005, Novoselov *et al*. demonstrated monolayer TMDC flakes by mechanical exfoliation of bulk TMDC crystals using adhesive tapes.[19] Since 2010, various properties such as the optical response and electronic transport characteristics of atomically thin TMDCs have been actively investigated. For example, Mak *et al*. demonstrated a significant increase of the photoluminescence (PL) intensity for monolayer MoS_2 compared with the multilayer crystals due to a crossover from an indirect- to a direct- bandgap nature with a decrease in the number of layers.[20] Radisavljevic *et al*. demonstrated monolayer MoS_2 field-effect transistors (FETs) with high on/off current ratios.[21] These reports have promoted research with respect to device applications of TMDCs for electronics and optoelectronics. Furthermore, heterostructures with a wide variety of TMDC combinations have also attracted much attention for advanced electronics and optoelectronics since 2013.[22, 23]

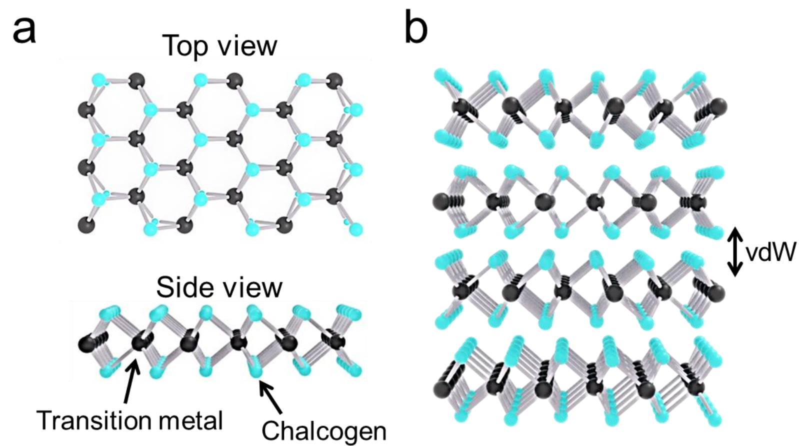

Figure 1.5 Schematic images of (a) monolayer and (b) bulk TMDCs.

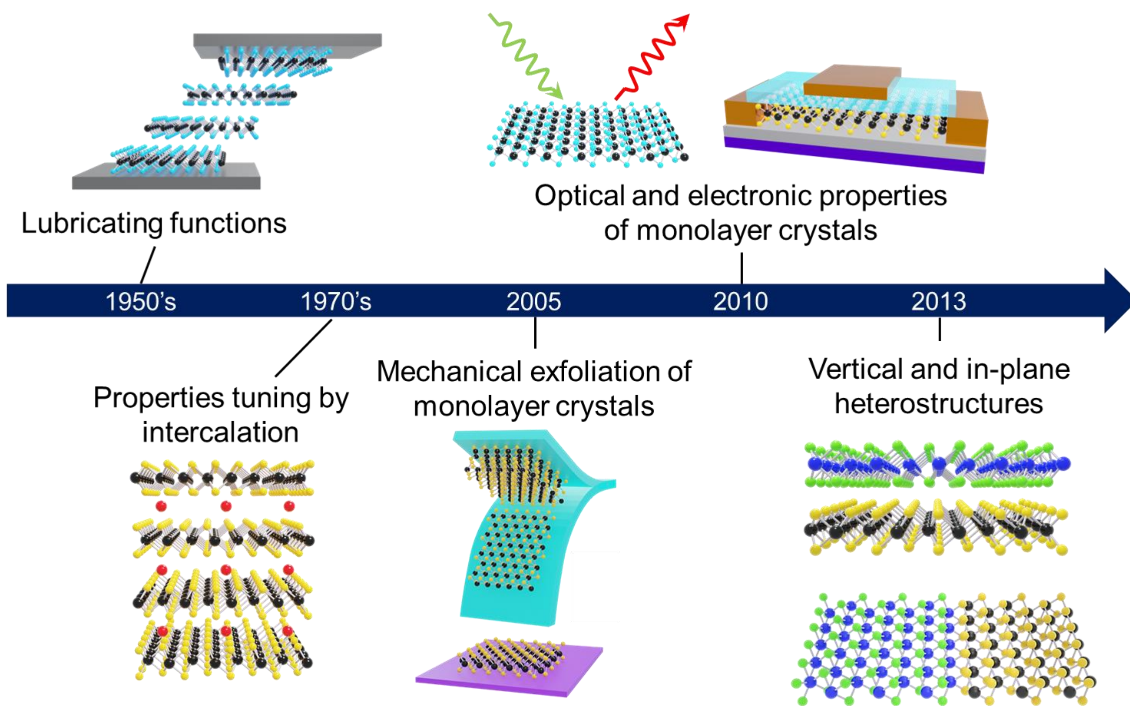

Figure 1.6 Timeline of the previous studies of TMDCs. [17-23]

1.5 Carrier Doping of TMDCs

Elemental Substitution

Elemental substitution is the most conventional method for carrier doping of semiconductors.[1] For typical three-dimensional semiconductors such as silicon, p-type doping can be achieved by substituting host atoms with dopant atoms that have one less outermost electron than the host atoms. In contrast, semiconductors of which the host atoms are substituted by impurity atoms with one more outermost electron exhibit n-type behavior.

The same substitutional doping mechanism can be applied to TMDC semiconductors. For example, p-type (n-type) doping can be realized by replacing Mo/W atoms with Nb (Re) in group-6 TMDCs such as MoS_2, WS_2, and WSe_2 (Figure 1.7a).[14, 24-28] For example, Suh *et al.* demonstrated stable and high-concentration p-type doping of MoS_2 by Nb substitution.[24] They performed the synthesis of bulk $Nb_xMo_{1-x}S_2$ single crystals through a chemical vapor transport (CVT) process. After the CVT synthesis, the multilayer $Nb_xMo_{1-x}S_2$ flake prepared by mechanical exfoliation exhibited a very high hole density of *ca.* 3.0×10^{19} cm^{-3}, which suggests degenerate p-type doping.

Such multilayer $Nb_xMo_{1-x}S_2$ flakes can be used as the components of 2D TFETs due to the degenerate p-type doping. Nakamura *et al.* demonstrated 2D TFETs of vertical $MoS_2/Nb_xMo_{1-x}S_2$ heterostructures with hexagonal boron nitride (h-BN) gate insulators.[29] They used MoS_2 and $Nb_xMo_{1-x}S_2$ as the n-type channel and p^+-type source, respectively, and the 2D

TFETs achieved very low SS values below 60 mV dec^{-1}.

While degenerate doping can be achieved in multilayer TMDC crystals, high-concentration doping is difficult in atomically thin TMDC crystals, especially monolayer TMDCs. This can be explained by two reasons. One is the higher ionization energy of dopant atoms in monolayer TMDCs than in multilayer TMDCs, as illustrated in Figure 1.7b. This is because the screening of coulombic interactions in monolayer TMDCs is weaker than in multilayer TMDCs due to the strong confinement of electron and holes in ultrathin structures, which results in lower dielectric properties (Figure 1.7c).[28, 30-32] Noh *et al*. reported the theoretically larger ionization energy of Nb or Re atoms in free-standing monolayer MoS_2 compared to that in bulk MoS_2.[32] This theoretical calculation also predicted that the ionization energy of the dopant atoms can be reduced by sandwiching the monolayer MoS_2 between dielectrics such as SiO_2 and HfO_2. Gao *et al*. reported an experimental demonstration where the Nb and Re atoms were not fully ionized in monolayer MoS_2 prepared by metalorganic chemical vapor deposition (MOCVD).[28] The other reason for the difficulty in the high-concentration doping of atomically thin TMDCs is unintentional defects. In the case of MoS_2 fabricated by mechanical exfoliation or CVD, most defects are V_s sulfur vacancies (Figure 1.7d) that behave as electron dopants. [33, 34] Fang *et al*. reported that exfoliated bilayer $Nb_xMo_{1-x}S_2$ exhibited n-type characteristics because the concentration of sulfur vacancies became larger than that of Nb, whereas bulk $Nb_xMo_{1-x}S_2$ flakes exhibited degenerate p-type electrical conductivity.[34]

For these reasons, multilayer TMDCs are more promising to obtain degenerate semiconductors by substitutional doping compared to monolayer TMDCs.

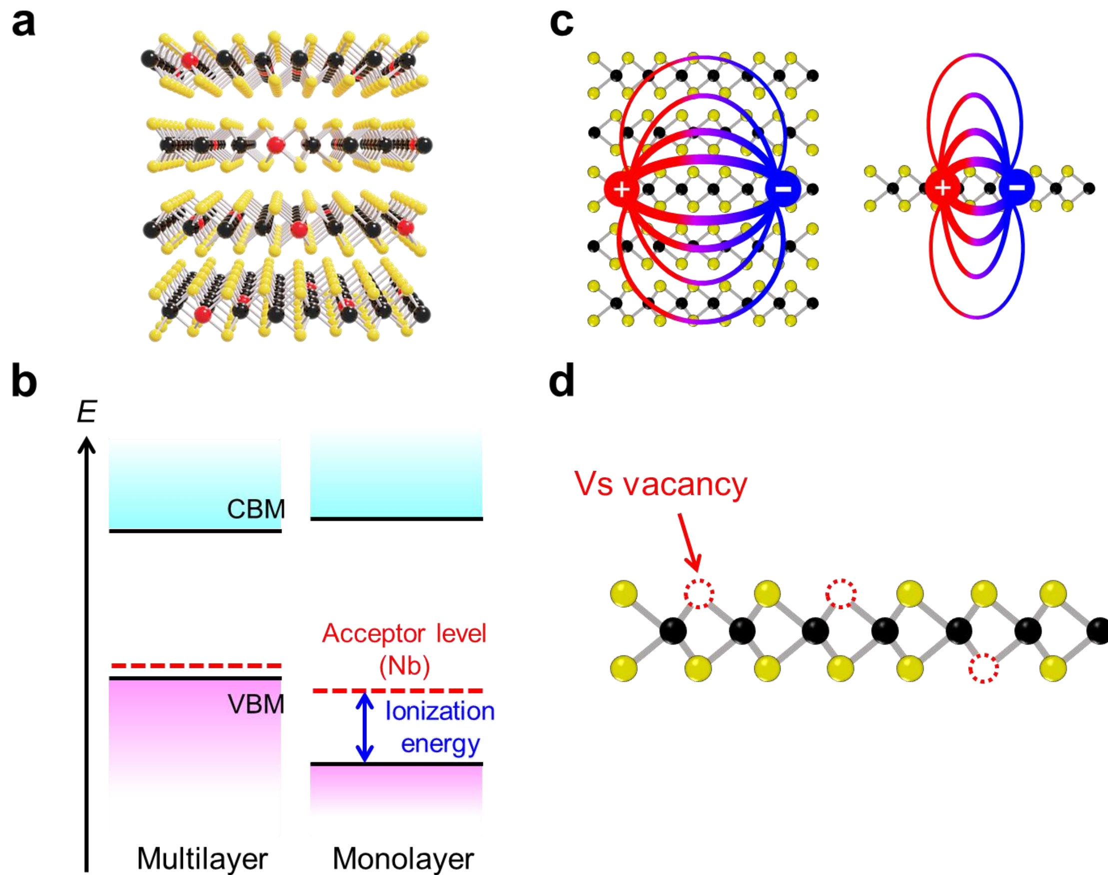

Figure 1.7 (a) Schematic illustration of a TMDC crystal with substitutional doping. (b) Band alignment of multilayer and monolayer TMDCs with Nb substitutional doping. (c) Dielectric screening of coulombic interactions in multilayer and monolayer TMDCs. (d) V_s sulfur vacancies of MoS_2.

Chemical doping

Chemical doping is another method for the carrier doping of TMDC thin films. The doping mechanism is based on surface charge transfer from the dopant to TMDCs (Figure 1.8a).[35-44] Fang et al. demonstrated degenerate surface charge transfer doping with K.[36] K can behave as an electron dopant due to its low electron affinity. The K-doped MoS_2 and WSe_2 showed very high electron densities of *ca*. 1.0×10^{13} cm^{-2} and *ca*. 2.5×10^{12} cm^{-2}, respectively. However, K is an unstable dopant in air due to the oxidation of K. To explore air-stable chemical doping, Kiriya *et al*. studied surface charge transfer doping with benzyl viologen (BV).[37] The BV-doped MoS_2 exhibited degenerate n-type behavior with a high electron density of *ca*. 1.2×10^{13} cm^{-2} and an electron mobility of 24.7 cm^{2} V^{-1} s^{-1}. Ji *et al*. demonstrated both p-type and n-type chemical doping of WSe_2 using 4-nitrobenzenediazonium and diethylenetriamine, respectively.[38] The

doped WSe_2 showed improved on/off current ratios and hole (electron) mobility of *ca*. 82 (25) $cm^2\ V^{-1}\ s^{-1}$. In addition, device applications were also performed, such as complementary MOS (CMOS) inverters and pn junctions by position selective doping. To develop such chemical doping techniques, other dopants such as p-toluene sulfonic acid (PTSA), amorphous titanium suboxide (ATO), and poly(vinyl-alcohol) (PVA) were also utilized.[41, 42, 44] However, there are still room for improvement in terms of the doping efficiency and stability of doped TMDCs (Figure1.8b).

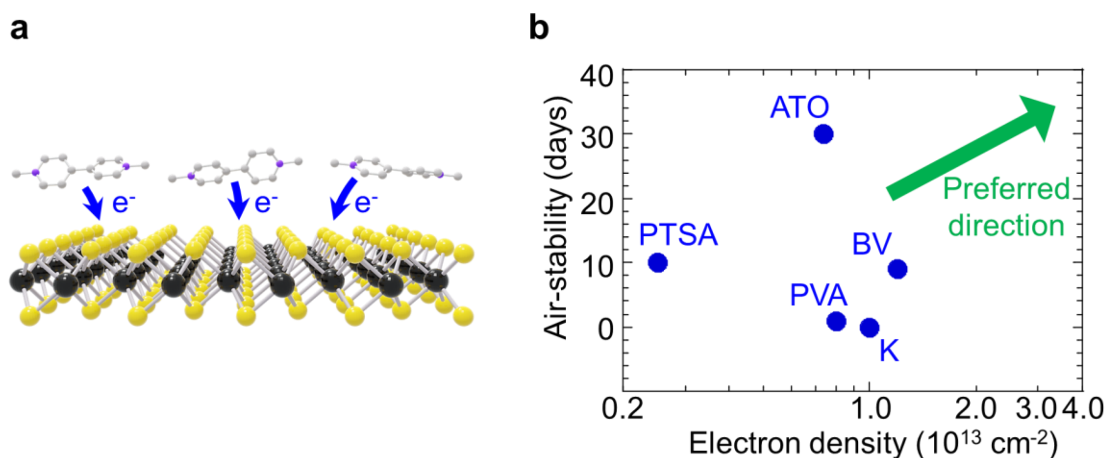

Figure 1.8 (a) Schematic illustration of chemical doping based on surface charge transfer.[37] (b) Comparison of previous chemical electron doping of MoS_2 that reported the electron density and air-stability of doped MoS_2. [36, 37, 41, 42, 44]

1.6 Vertical Heterostructures of TMDCs

Vertical heterostructures (Figure 1.9) fabricated by stacking one TMDC onto another material are the most popular TMDC-based heterostructures.[3, 22, 29, 45-56] These vertical heterostructures can be versatile platforms for device applications due to their atomically sharp interfaces derived from vdW interactions and dangling bond-free layered structures. Many vertical heterostructures using TMDCs have been demonstrated for electronic and optoelectronic devices to date. In particular, most reported TMDC-based tunnel diodes and TFETs are based on vertical heterostructures. For example, Roy *et al*. reported tunnel diodes of MoS_2/WSe_2 vertical heterostructures with dual gates.[46] They realized highly doped pn junctions by the gate tuning of MoS_2 and WSe_2. The heterostructures exhibited NDR at low temperatures that supported electron tunneling and type III band alignment. The same research group also reported the p-type TFETs using $SnSe_2/WSe_2$ heterostructures with a single back gate. The TFETs exhibited no temperature-dependent SS, which confirmed the electron tunneling current.[48]

In addition to such TMDC/TMDC heterostructures, similar vertical heterostructures

composed of TMDCs and other materials have also been used for tunnel diodes and TFETs. Yan *et al*. demonstrated tunnel diodes based on vertical $SnSe_2$/black phosphorus (BP) heterostructures. The tunnel diodes showed NDR even at room temperature.[47] Sarkar *et al*. demonstrated subthermionic TFETs with an atomically thin MoS_2 channel for the first time..[3] The TFETs were based on vertical 2D/3D heterostructures of the MoS_2 channel and p^+-Ge source. Electron tunneling at the p^+-Ge/MoS_2 heterointerface was confirmed by observation of the NDR trend. Furthermore, the p^+-Ge/MoS_2 TFETs exhibited a very low SS of 31.1 mV dec^{-1}, which is an average for 4 decades of drain current at room temperature. Table 1 shows a summary of the tunnel diodes and TFETs based on vertical heterostructures. Although tunnel diodes and TFETs have been demonstrated using a wide variety of material combinations, the realization of SS values lower than 60 mV dec^{-1} is still a challenge. Moreover, no tunnel diodes or TFETs based on in-plane heterostructures have been reported.

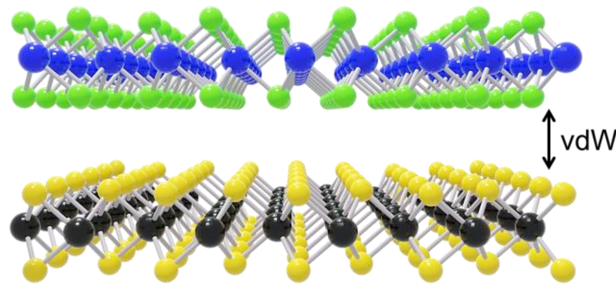

Figure 1.9 (a) Schematic illustration of a TMDC vertical heterostructure.

Table 1 Summary of tunnel diodes and TFETs based on 2D vertical heterostructures.

References	Material	NDR or NDR trend	SS (mV/dec)
[46]	MoS_2/WSe_2	NDR (150 K)	*ca.* 130
[3]	Ge/MoS_2	NDR trend (300K)	31.1
[47]	$BP/SnSe_2$	NDR (300 K)	
[48]	$WSe_2/SnSe_2$	NDR (77K)	*ca.* 140
[49]	BP/ReS_2	NDR (300K)	
[50]	MoS_2/WSe_2	NDR (300K)	
[51]	$SnSe_2/WSe_2$	NDR trend (RT)	37
[52]	BP/MoS_2	NDR trend (RT)	55
[53]	MoS_2/WSe_2	NDR trend (240 K)	*ca.* 400
[54]	$WSe_2/SnSe_2$	NDR (RT)	90
[55]	BP/ReS_2	NDR (RT)	
[29]	MoS_2/WSe_2	NDR trend (160K)	< 60
[56]	MoS_2/WSe_2		36

1.7 In-Plane Heterostructures of TMDCs

TMDC-based in-plane heterostructures composed of different crystals with covalent bonding are also promising for electronics and optoelectronics applications. [23, 28, 46, 57-82] In particular, in-plane heterostructures can be synthesized by CVD (Figure 1.10), which enables scalable and position-selective growth toward device integration.[28, 66] To realize high-performance device applications, monolayer in-plane heterostructures with various TMDC combinations including MoS_2, WS_2, $MoSe_2$, and WSe_2 are actively under investigation. Huang *et al.* demonstrated in-plane heterostructures of monolayer $MoSe_2/WSe_2$ with very high crystalline quality for the first time.[57] Duan *et al.* reported the epitaxial growth of $MoS_2/MoSe_2$ and WS_2/WSe_2 in-plane heterostructures using TMDC bulk powders as precursors.[58] In particular, they first demonstrated

that a pn diode can be formed by the WS_2/WSe_2 in plane heterostructure. Gong *et al*. reported the controllable synthesis of both in-plane and vertical heterostructures,[23] where the vertical heterostructures were fabricated at a growth temperature of *ca*. 850 °C, whereas the lower growth temperature of *ca*. 650 °C led to the synthesis of in-plane heterostructures. These previous works firstly demonstrated the fabrication of TMDC in-plane heterostructures with high crystalline quality through a CVD process. In contrast, the changes in the composition of TMDCs were not sharp due to alloy formation in the range of more than *ca*. 10 nm from the heterointerfaces.

Many previous studies on CVD growth have been reported as attempts to achieve further progress with in-plane heterostructures. Li *et al*. achieved epitaxial synthesis of WSe_2/MoS_2 in-plane heterostructures with atomically sharp interfaces through a two-step CVD process. [46] The WSe_2/MoS_2 in-plane heterostructures also exhibited rectifying characteristics and photovoltaic effects as pn diodes. The two-step CVD growth of in-plane heterostructures with atomically sharp interfaces was also performed by Zhang *et al*.;[65] they designed a robust CVD growth system that could change the carrier gas flow direction to cool the first synthesized crystals and reduce thermal degradation. WS_2/WSe_2 grown by this robust epitaxial synthesis exhibited diode properties with a rectification ratio of 10^5.

A one-step CVD growth system was also developed. Sahoo *et al*. demonstrated the one-pot growth of in-plane heterostructures to achieve both high-quality heterointerfaces and scalability. [67] The composition of TMDC crystals can be controlled only by changing the carrier gas under water vapor conditions. This approach can also control the crystal size *in situ*. Furthermore, the $MoSe_2/WSe_2$ and MoS_2/WS_2 in-plane heterostructures fabricated by the one-pot growth showed rectifying IV curves and photocurrents, which indicated the formation of pn diodes. Similar sequential growth was also demonstrated by Wada *et al*.[76] Their lab-built CVD system enabled large-scale growth of high-quality in-plane heterostructures by moving the precursors with a magnet. They also realized efficient circularly polarized electroluminescence at the WS_2/WSe_2 interfaces by electronic double layer doping using ion gels.

In addition to such monolayer TMDC in-plane heterostructures, bilayer in-plane heterostructures have also been studied for high-performance device applications. Sahoo *et al*. reported bilayer in-plane heterostructures of MoS_2/WS_2 and $MoSe_2/WSe_2$ grown by the one-pot growth. [70] The bilayer heterostructures exhibited diode properties with a rectification current one order of magnitude higher and improved photovoltaic/electroluminescent effects compared to monolayer in-plane heterostructures.

The in-plane heterostructures as discussed here were used for pn junctions based on a staggered gap (type II) band alignment. In contrast, detailed studies of the electronic states of in-plane heterostructures were also reported. Zhang *et al*. reported visualization of the band alignment of monolayer WSe_2/MoS_2 in-plane heterostructures with scanning tunneling

spectroscopy (STS).[69] They demonstrated a straddling (type I) band alignment due to band bending derived from strain effects. STS measurements of band bending were also performed by Kobayashi *et al.* [63] for bilayer in-plane heterostructures that consisted of bilayer WS_2 and vertical MoS_2/WS_2. A one-dimensional confining potential due to band bending was exhibited at the heterointerface of the in-plane heterostructures.

The electronic states of in-plane heterostructures are also controlled by intentional alloy formation. Kobayashi *et al.* demonstrated the one-step synthesis of monolayer $Mo_{1-x}W_xS_2$ alloys. [83] The band gap of monolayer $Mo_{1-x}W_xS_2$ can be tuned by changing the W composition, *x*. Pu *et al.* reported color-tunable light-emitting diodes based on $WS_{2(1-x)}Se_{2x}$.[78] The light emission energy of $WS_{2(1-x)}Se_{2x}$ was gradually changed from 1.7 to 2.1 eV due to band gap tuning by control of the S (Se) composition. Nugera *et al.* reported band gap engineering by the synthesis of in-plane heterostructures based on different monolayer TMDC alloys.[79] They fabricated monolayer $MoS_{2(1-x)}Se_{2x}/WS_{2(1-x)}Se_{2x}$ heterostructures that exhibited continuously controlled band gaps. Furthermore, bilayer and trilayer in-plane heterostructures of TMDC alloys were also realized with tuning of the compositions. These previous studies indicate that alloy formation is also effective to control the electronic states of the TMDC heterostructures.

To construct nanostructured devices for advanced electronics, 2D multi-heterostructures and superlattices are also important. Xie *et al.* reported atomically thin superlattices synthesized by MOCVD.[68] The MOCVD system can precisely control the composition and width of TMDCs by changing the chalcogen precursors, where the width of the WS_2 and WSe_2 layers can be decreased down to *ca*. 20 nm. Kobayashi *et al.* also demonstrated similar epitaxial growth of multi-heterostructures.[71] The $WS_2/MoS_2/WS_2$ multi-heterostructures that have zigzag heterointerfaces without alloy formation were grown by MOCVD. The MOCVD was also employed to realize the synthesis of MoS_2 nanoribbons from the edges of WS_2 crystals.

Many previous studies have reported TMDC-based in-plane heterostructures and superlattices; however, the carrier density of TMDC crystals that consist of such CVD-grown in-plane heterostructures is not typically high (*ca.* 10^{11}–10^{12} cm^{-2}) due to the lack of intentional doping. The fabrication of in-plane heterostructures with high-concentration doping is thus important to improve the electronic and optoelectronic device performance. Okada *et al.* demonstrated in-plane pn junctions based on monolayer MoS_2/Nb-doped MoS_2 ($Nb_xMo_{1-x}S_2$).[75] The MoS_2 and $Nb_xMo_{1-x}S_2$ respectively exhibited n-type and highly doped p-type behavior, and the $MoS_2/Nb_xMo_{1-x}S_2$ exhibited typical rectifying properties. Vu *et al.* reported monolayer Nb-doped WS_2/MoS_2 in-plane heterostructures for high-detectivity photodiodes.[77] They performed selective Nb substitution in the WS_2 region at different atomic ratios from 0 at% to 8.1 at% estimated by Nb/(W+Nb). WS_2 with 8.1 at% Nb substitution showed a high hole density of 1.16×10^{13} cm^{-2}. In particular, the Nb-doped WS_2/MoS_2 at 8.1 at% Nb substitution showed

superior photoinduced current and detectivity compared to other CVD-grown TMDC-based pn junctions.

Although such TMDC-based in-plane pn junctions with substitutional doping have attracted much attention for advanced electronics and optoelectronics, tunnel diodes and TFETs based on in-plane heterostructures have been less explored due to the difficulty in high-concentration carrier doping by elemental substitution for atomically thin structures, as discussed in section 1.5.

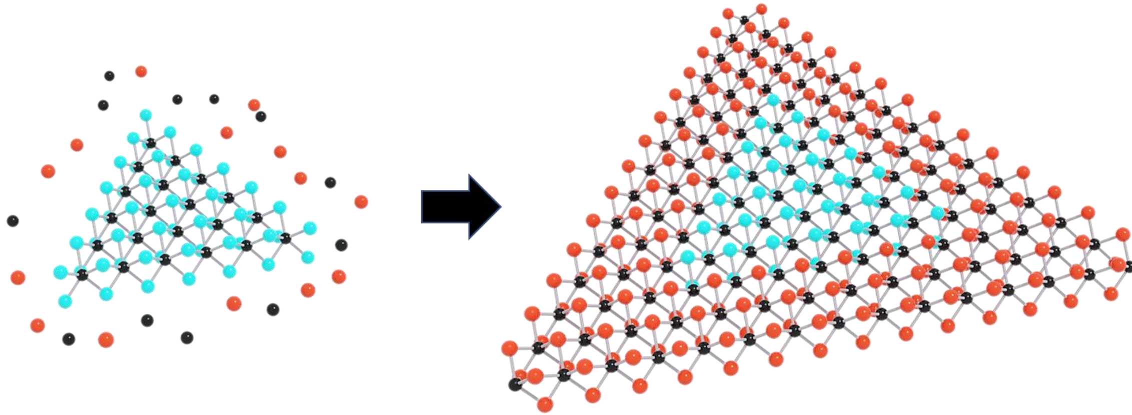

Figure 1.10 Schematic illustration of CVD growth of TMDC in-plane heterostructures.

1.8 Purposes of This Work

TMDCs and their heterostructures have attracted much attention for advanced electronics. However, in-plane heterostructures with high-concentration doping is still challenging due to the low dielectric properties of monolayers. In particular, tunnel diodes and TFETs based on TMDC in-plane heterostructures have not been reported. It is also important to optimize the doping processes for air-stable and efficient doping of monolayer TMDCs. Therefore, we define the purposes of this work as follows.

1. Fabrication and electronic transport properties of multilayer in-plane heterostructures based on TMDCs.

To solve the issue of the difficulty in obtaining TMDC in-plane heterostructures with high-concentration doping, multilayer TMDCs were employed. Structural analysis and electronic transport measurements of multilayer WSe_2/MoS_2 and $Nb_xMo_{1-x}S_2/MoS_2$ in-plane heterostructures were then performed.

2. Air-stable and efficient electron doping of monolayer MoS_2 by salt-crown ether treatment

To achieve high-concentration doping of monolayer TMDCs, surface charge transfer by chemical doping was determined to be effective. However, there is still room for improvement to achieve both doping efficiency and air-stability. In this work, we demonstrated the chemical electron doping of monolayer MoS_2 with KOH/benzo-18-crown-6. The doped MoS_2 exhibited a very high electron concentration of 3.4×10^{13} cm^{-2} and air-stability of *ca*. 1 month.

Chapter 2:

Experimental Methods

2.1 Mechanical Exfoliation

Mechanical exfoliation is one of the primary methods for the preparation of TMDC thin crystals (Figure 2.1a). Bulk TMDC crystals (Figure 2.1b) can be synthesized by the chemical vapor transport method.[84] In bulk TMDC crystals, monolayers are weakly bonded via vdW forces. Therefore, thin crystals can be fabricated by peeling off the bulk crystals with adhesive tape (Figure 2.1c). The peeled flakes on the adhesive tape are transferred to a polydimethylsiloxane (PDMS) sheet (Figure 2.1d) and the PDMS sheet is then stamped on the sample substrate. Figure 2.1e shows an optical micrograph image of the exfoliated flakes on a SiO_2/Si substrate. Many large flakes with widths of *ca*. 100 μm are thus fabricated.

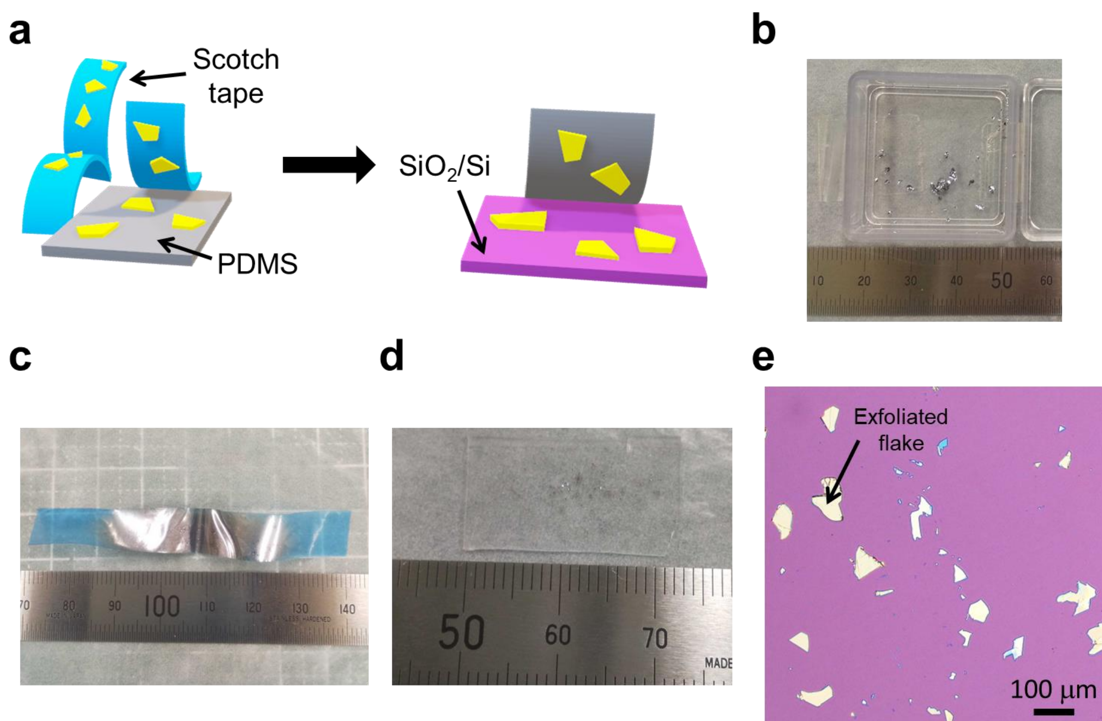

Figure 2.1 (a) Schematic illustration of the mechanical exfoliation process. Photographs of (b) bulk TMDC crystals, (c) scotch tape, and (d) PDMS gel film. (e) Optical micrograph image of exfoliated TMDC crystals.

2.2 Chemical Vapor Deposition (CVD)

CVD is another effective method for the synthesis of TMDC thin crystals. This method can achieve scalable growth of high-quality TMDC thin crystals down to monolayers. The CVD

growth process of TMDCs is based on (i) the sublimation of solid precursors, (ii) the supply of sublimated precursors to a substrate by carrier gas flow, (iii) the diffusion of sublimated precursors on the substrate, and (iv) the nucleation of crystals. Figure 2.2a shows a schematic image of typical CVD apparatus employed for MoS_2 synthesis. MoO_2 and S precursors are heated by furnaces, and N_2 is typically used as a carrier gas. Alkali metal halogen compounds such as KBr can promote MoS_2 growth by lowering the sublimation point of MoO_2. Other TMDCs such as WS_2, $MoSe_2$, and WSe_2 can also be synthesized by changing the precursors and carrier gas. For example, WSe_2 crystals can be grown by the supply of sublimated WO_3 and Se with a N_2/H_2 gas flow. Figure 2.2b shows our in-house-built CVD apparatus. This system can provide many monolayer MoS_2 crystals, as shown in Figure 2.2c. Furthermore, CVD growth is also effective for the preparation of TMDC heterostructures. In our experiments, TMDC heterostructures are prepared by MoS_2 growth from the edges of exfoliated flakes (Figure 2.2d)

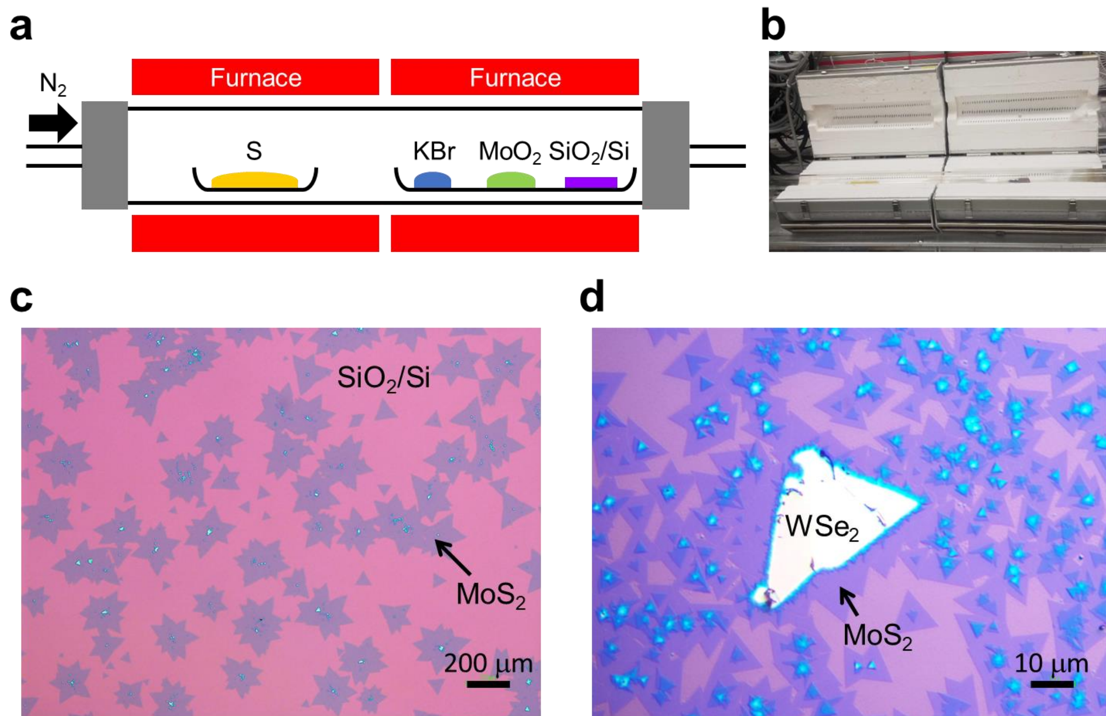

Figure 2.2 (a) Schematic illustration of the CVD apparatus employed for MoS_2 synthesis. (b) Photograph of our in-house-built CVD system. Optical micrograph images of (c) monolayer MoS_2 and (d) WSe_2/MoS_2 heterostructures on SiO_2/Si substrates. The WSe_2/MoS_2 heterostructures are prepared by CVD growth of MoS_2 after exfoliation of the WSe_2 flakes.

2.3 Photolithography

Device fabrication is required to investigate the electronic transport properties of the TMDC samples. The most typical method for nanoscale device fabrication is photolithography.

Figure 2.3a shows a schematic illustration of the photolithography process. To perform this process, (i) a sample substrate is firstly prepared. (ii) Photoresist is coated on the sample substrate. (iii) To define the geometry of the electrode, only selected areas are exposed to ultraviolet (UV) light. (iv) After UV light exposure, the photoresist can be developed by immersion of the substrate in a developer solution. The photoresist in the exposed area is removed because the solubility in the developer is enhanced by UV exposure. In contrast, the photoresist in the unexposed areas is not removed. (v) To make the electrode, contact metals are evaporated onto the substrate after photoresist development. (vi) The actual electrode can be fabricated by a lift-off process. The evaporated metal in the undeveloped area is removed with the residual photoresist. In contrast, the evaporated metal in the developed area remains on the substrate. Figures 2.3b-d show optical micrographs of the actual sample during the photolithography process.

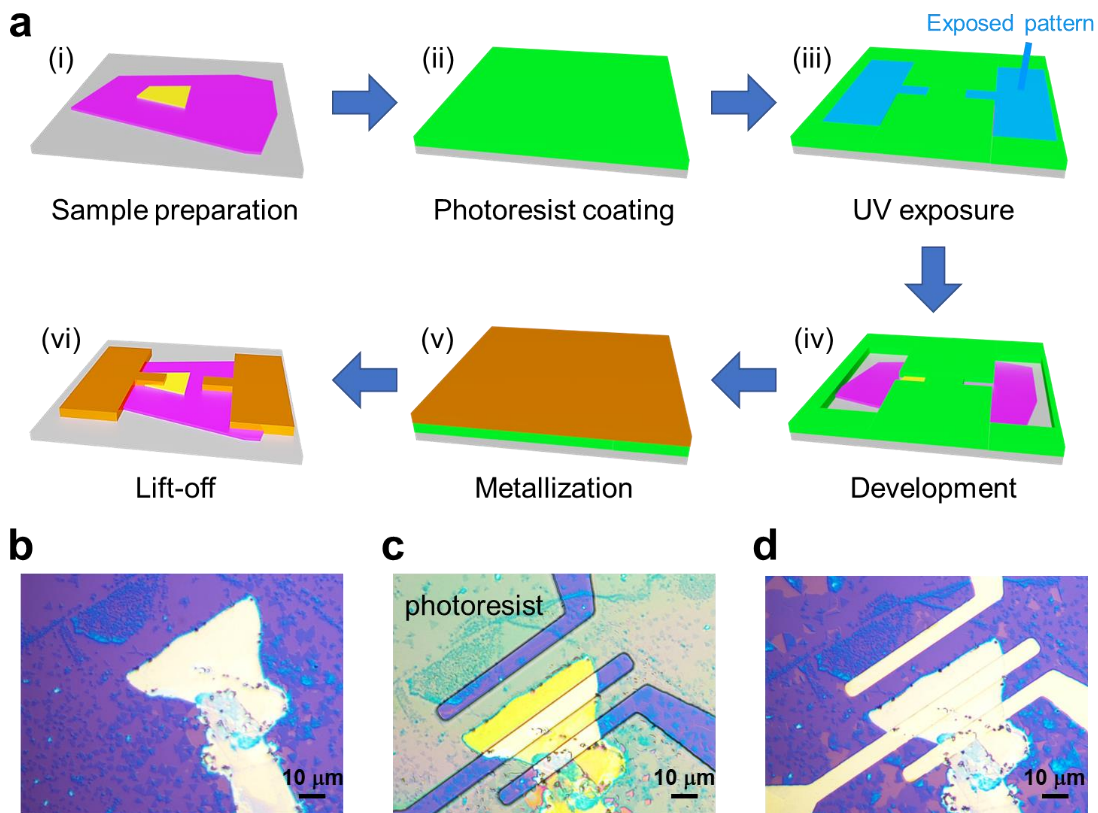

Figure 2.3 (a) Schematic illustration of the photolithography process. Optical micrographs of the sample during (b) preparation, (c) photoresist coating and development, and (d) device fabrication.

Our experimental photolithography process consists of the following steps.

(i) To remove the impurities on the sample substrate, the substrate is warmed on a hot plate (HP-1SA, AS ONE, Figure 2.4a) at 100 °C for 1 min.

(ii) The prepared sample substrate is hydrophobized with 1,1,1,3,3,3-hexamethyldisilazane (HMDS; Tokyo Chemical Industry Co., Ltd., Figure 2.4b). HMDS is dropped onto the sample substrate and spin-coated. The spin coating steps are 500 rpm/5 s + 2000 rpm/60 s. Figure 2.4c shows a photograph of the spin coater (K-359S1, Kyowa Riken Co., Ltd.)

(iii) The sample substrate is warmed on a hot plate at 100 °C for 1 min.

(iv) The photoresist (AZ-P 1350, Merck Performance Materials, Figure 2.4d) is dropped and spin-coated on the substrate under the same conditions as that for the HMDS treatment in step (ii).

(v) To remove the solvents and moisture in the photoresist, the substrate is warmed on a hot plate at 100 °C for 5 min.

(vi) To design the electrode patterns, the sample substrate is exposed to UV-light. A photograph of the maskless photolithography system (PALET, Neoark Corporation) is shown in Figures 2.4e,f. The UV exposure conditions can be controlled by changing the UV intensity, exposure time, and focus offset (Figure 2.4g). This process was performed with a UV intensity of 20%, an exposure time of 1 s, and a focus offset of -10 μm.

(vii) Development of the photoresist by immersion of the substrate in the developer (MR-D7, Mitani Micronics Co., Ltd.) for 1 min.

(viii) Immersion of the substrate in pure water for 1 min.

(ix) Evaporation of metals under vacuum conditions. Au (20 nm)/In (5 nm) were evaporated by resistive thermal evaporation. The evaporation rates of In and Au were *ca*. 0.02 nm s^{-1} and *ca*. 0.05 nm s^{-1}, respectively. Figure 2.4h shows a photograph of the evaporation equipment (EX-200, Ulvac).

(x) Lift-off process of the substrate. The substrate is immersed in acetone and slightly shaken on a shaker (Figure 2.4i) for 30 min.

(xi) To remove the resist residue and other adsorbates, the substrate is annealed at 300 °C under vacuum (*ca*. 10^{-4} Pa) for 60 min. Figure 2.4j shows the electrical furnace used for the annealing process.

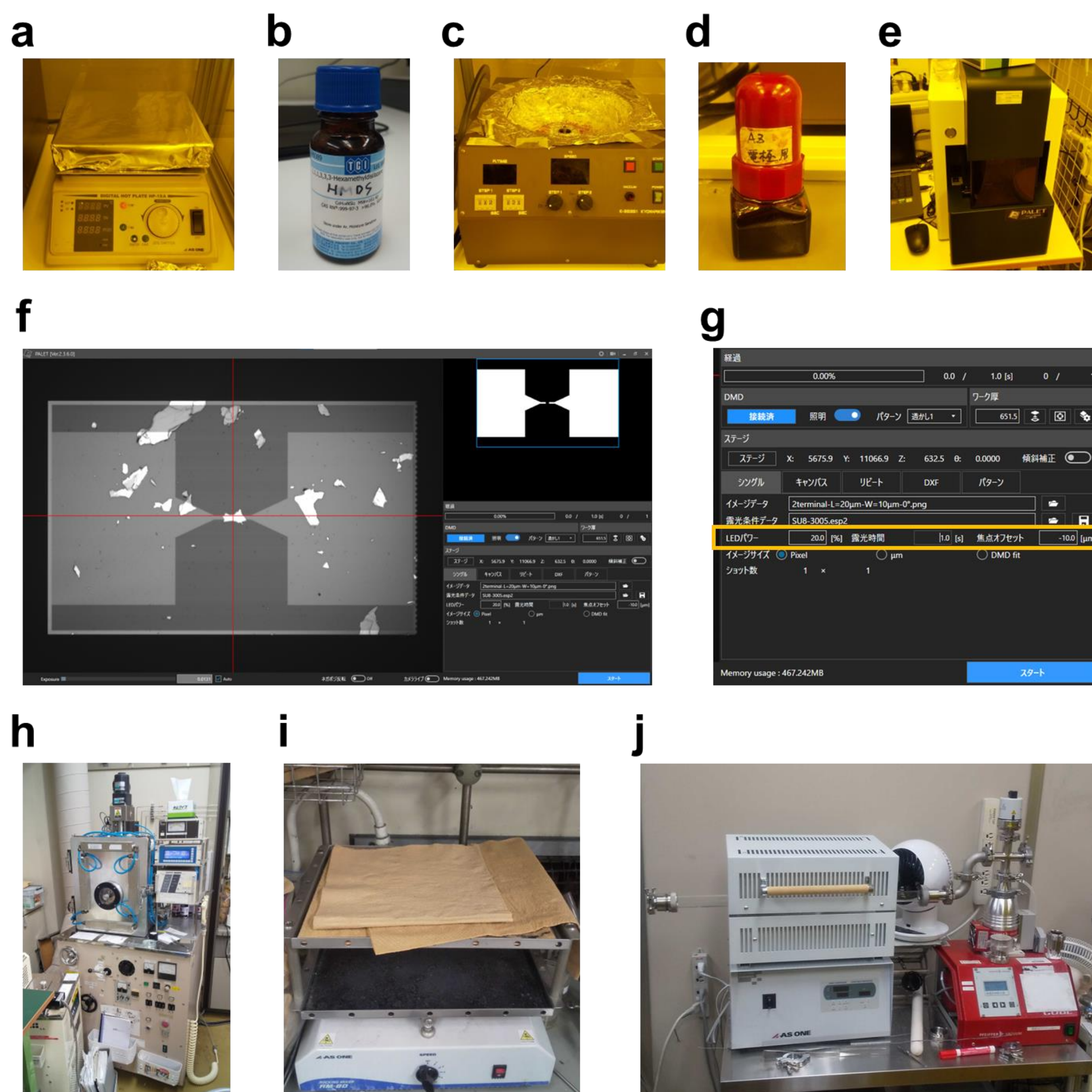

Figure 2.4 Photographs of the (a) hot plate, (b) HMDS, (c) spin coater, (d) photoresist, and (e) maskless lithography system. (f, g) Screen shots of the application (PALET) for maskless photolithography. Photographs of the (h) evaporation equipment, (i) shaker, and (j) electrical furnace for vacuum annealing.

2.4 Plasma Etching

Plasma etching is effective to control the shape of the channel materials. For example, monolayer TMDC crystals can be etched by O_2 plasma. The channel shape can be controlled by combining photolithography and plasma etching (Figure 2.5a). Although the monolayer TMDC crystal is etched by exposure to O_2 plasma, the rest of the monolayer region is not etched due to protection by the photoresist. Figures 2.5b,c show optical micrographs of the sample before and after the O_2 plasma etching. The monolayer MoS_2 is etched except for the area under the

photoresist. In these experiments, the devices were etched by plasma irradiation for 1 min using a Tergeo plasma cleaner (Pie Scientific, Figure 2.5d) at 49 W in air.

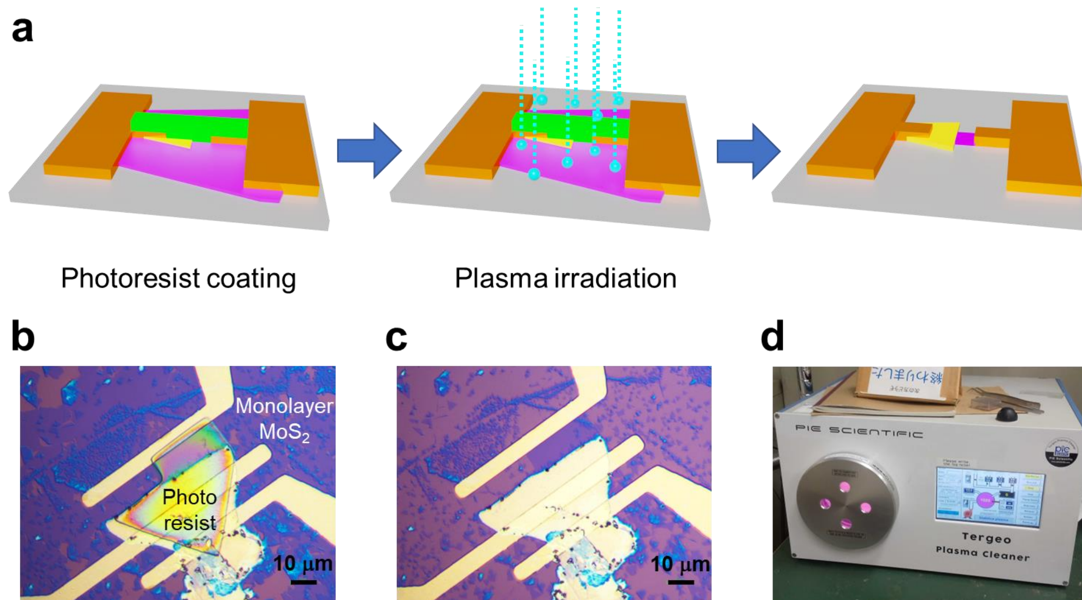

Figure 2.5 (a) Schematic illustration of the etching process. Optical micrographs of the device (b) with photoresist coating and (c) after plasma irradiation. (d) Photograph of the Tergeo plasma cleaner.

2.5 Electrical Measurement

The carrier transport properties were measured using a probe station (Riko International Ltd., Figure 2.6a) with a semiconductor parameter analyzer (4200A-SCS, Keithley, Figure 2.6b) connected in the configuration. The temperature was controlled using a closed cycle helium cryostat (Helium compressor unit CKW-21, Sumitomo Heavy Industries Ltd, Figure 2.6c). In this study, three terminals of source, drain, and gate electrodes were used for FET measurements (Figure 2.6d). The carrier density of the samples was controlled by back-gating through the SiO_2/Si substrate.

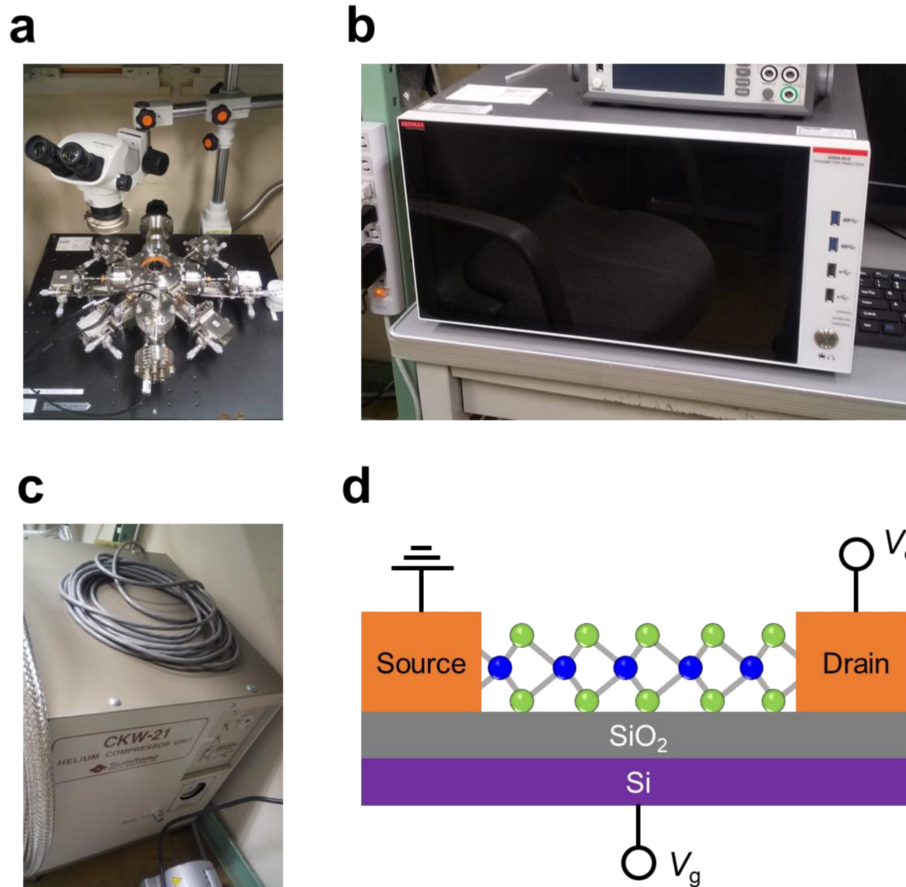

Figure 2.6 Photographs of the (a) probe station, (b) semiconductor parameter analyzer, and (c) cryostat. (d) Schematic illustration of a back-gated TMDC FET.

Chapter 3:

Multilayer In-Plane Heterostructures Based on Transition Metal Dichalcogenides for Advanced Electronics

3.1 Introduction

Semiconductor heterostructures play an important role in the development of modern low-dimensional physics and optical/electronic device applications. Recently, transition metal dichalcogenides (TMDCs) have attracted much attention due to their future device applications. [7-15] For their device applications, the use of in-plane heterostructures based on TMDCs provides a scalable way to create basic device structures, including pn junctions, semiconductor heterojunctions, and metal/semiconductor junctions.[23, 28, 46, 57-83] Such structures have been used to demonstrate various devices, including field-effect transistors, pn diodes, photodetectors, and light-emitting diodes. Importantly, in-plane heterostructures can be prepared through scalable vapor-phase growth processes, such as chemical vapor deposition (CVD). The recent progress in growth techniques also enables scalable and position-selective growth toward device integration. [28, 66, 85]

To maximize the potential of in-plane heterostructures in device applications, further control of their structure and electronic properties is important. To date, such in-plane heterostructures have been realized through the combination of semiconducting monolayer TMDCs, including MoS_2, WS_2, $MoSe_2$, and WSe_2.[23, 28, 46, 57-59, 61-69, 71-78, 80-82] In addition, bilayer and trilayer TMDC heterostructures have also been demonstrated.[60, 63, 70, 79] Furthermore, a similar growth process was extended to multilayer-based in-plane heterostructures of GeS and SnS.[86, 87] However, no studies on in-plane heterostructures based on multilayer TMDCs have been reported. Generally, multilayer TMDCs have high carrier mobilities.[88-93] More importantly, a high carrier density of up to $\sim 3 \times 10^{19}$ cm^{-3} was achieved by substitutional doping of Nb into multilayer MoS_2, realizing a degenerate p-type semiconductor of TMDCs.[24, 29] This is due to the lower ionization energies of substitutional dopants in multilayer MoS_2.[28, 31, 32] In other words, the low dielectric properties of monolayers prevent the generation of high concentrations of thermally-excited carriers from doped impurities. Multilayer TMDCs are therefore appropriate for highly doped pn junction-based device applications such as tunnel diodes and tunneling field-effect transistors (TFETs). Nakamura et al. recently demonstrated TFETs with a very low subthreshold swing below 60

mV/dec using vertical heterostructures of n-type trilayer MoS_2 and multilayer $Nb_xMo_{1-x}S_2$ as the p^+-type source.[29] This finding motivates us to fabricate in-plane heterostructures based on multilayer TMDCs.

Here, we report the fabrication and characterization of in-plane heterostructures based on multilayer TMDCs. Multilayer MoS_2 was grown from the edges of exfoliated multilayer WSe_2 and $Nb_xMo_{1-x}S_2$ flakes. This paper is organized as follows. The first part describes the structure analysis and electronic transport properties of the multilayer WSe_2/MoS_2 heterostructures. In particular, cross-sectional electron microscopy observations of the WSe_2/MoS_2 heterostructures confirm the edge-initiated epitaxial growth of multilayer MoS_2 from the edge of WSe_2 with an abrupt change of compositions within a region of ~2 nm around the interface. In addition to the lateral growth, the multilayer MoS_2 was also grown on the surface of exfoliated WSe_2 flakes. In the second part, we investigated the structures and electronic transport properties of the multilayer $Nb_xMo_{1-x}S_2/MoS_2$ heterostructures. Transport measurements show a change in the band alignment from a staggered gap to a broken gap induced by electrostatic electron doping of MoS_2. First-principles calculations also support the staggered gap band alignment for $Nb_xMo_{1-x}S_2/MoS_2$.

3.2 Experimental Methods

Sample preparation

$Nb_xMo_{1-x}S_2$ bulk crystals were purchased from HQ Graphene. WSe_2 bulk crystals were grown using a chemical vapor transport technique.[84] Multilayer $Nb_xMo_{1-x}S_2$ and WSe_2 flakes were prepared by mechanical exfoliation of bulk crystals on SiO_2 (285 nm)/Si substrates. MoS_2 was grown via salt-assisted CVD using a lab-made setup with two electric furnaces.[94, 95] The exfoliated $Nb_xMo_{1-x}S_2$ or WSe_2 flakes on SiO_2/Si substrates were placed in a quartz tube, and MoO_2 powder (40−70 mg), KBr powder (3−8 mg) and sulfur flakes (2−3 g) were placed 1, 2, and 30 cm upstream from the substrates, respectively. The quartz tube was then filled with N_2 gas at flow rates of 150−300 sccm. The temperatures of the substrate and powders were gradually increased to 700−850 °C using one of the electric furnaces. After the set-point temperature was reached, the sulfur flakes were heated at 175−180 °C for 2−5 min using the second electric furnace to supply sulfur vapor to the substrate. After growth, the quartz tube was immediately cooled using an electric fan.

Device Fabrication and Transport Measurements

Two-terminal electrodes were fabricated by photolithography. The samples on SiO_2/Si substrates were spin-coated with an AZ P1350 photoresist (Merck Performance Materials), followed by an exposure/development process. Au (20 nm)/In (5 nm) was deposited by resistive

thermal evaporation (ULVAC, EX-200). After evaporation, the contact metals were lifted off by acetone. The devices were plasma-etched for 1 min using a Tergeo plasma cleaner (Pie Scientific) at 49 W under air. The devices were then annealed at 300 °C under vacuum (~10^{-3} Pa) for 60 min before the transport measurements. The carrier transport properties were measured using a cryogenic probe station (Riko International LTD) with a semiconductor parameter analyzer (KEITHLEY, 4200A-SCS).

Characterizations

Raman and PL measurements were carried out at 532 nm excitation in a backscattering configuration using a microspectrometer (Renishaw, inVia). Topographic images were acquired in noncontact mode using a scanning probe microscope (Park Systems, NX10). Cross-sectional TEM specimens were prepared using the focused ion beam method. TEM images were taken at an acceleration voltage of 200 kV using a high-resolution transmission electron microscope (Hitachi High Technologies Corporation, H-9500). For STEM observations, HAADF images and EDS elemental mappings were collected at room temperature using a JEM-ARM200F (Cold FEG) equipped with a CEOS ASCOR corrector and a 100 mm2 SDD detector (JED-2300) operated at 120 kV. XRF measurements were conducted using JSX-1000S instrument (JEOL).

Computational Methods

All theoretical calculations were conducted using the STATE program package[96, 97] based on the density functional theory.[98, 99] The exchange-correlation potential energy between electrons was treated by the generalized gradient approximation with a Perdew-Burke-Ernzerhof functional.[100] Ultrasoft pseudopotentials were adopted to describe the interaction between valence electrons and ions.[101] The valence wave functions and deficit charge density were expanded in terms of plane-wave basis sets with cutoff energies of 25 and 225 Ry, respectively. Brillouin-zone integration was carried out with 6 × 6 × 1 and 1 × 6 × 1- k-meshes for 3 × 3 and 18 × 3 supercells, respectively. Internal atomic coordinates under the fixed lattice parameters corresponding to those of experimental MoS_2 were optimized until the force acting on atoms was less than 1.33×10^{-3} hartree. To exclude the unphysical dipole interaction with the periodic images normal to the sheet, we used the effective screening medium method.[102, 103]

3.3 Results and Discussions

3.3.1 Multilayer WSe_2/MoS_2 Heterostructures.

Structure analysis

Figure 3.1a shows a schematic image of the present growth process of TMDC-based multilayer heterostructures. First, WSe_2 flakes were mechanically exfoliated onto SiO_2/Si substrates by using a polydimethylsiloxane (PDMS) sheet. CVD growth of MoS_2 was then conducted with these substrates. Figure 3.1b shows an optical micrograph image of the exfoliated WSe_2. The present exfoliated WSe_2 is a white flake due to its thick, multilayered structure. After the growth of MoS_2, blue and purple regions can be seen around the edges of the WSe_2 flake (Figure 3.1c). Topographic images of these samples were obtained by AFM, as shown in Figure 3.1d,e. The exfoliated WSe_2 flake shows a sharp edge, whereas step-like height profiles can be observed at the edge of the WSe_2 flake after the MoS_2 CVD process, which suggests the growth of multilayer MoS_2. The white spots on the WSe_2 region in the topographic image of WSe_2/MoS_2 (Figure 3.1e) probably correspond to products derived from incomplete sulfurization of MoO_2 similar to the previous study.[104] The structures and components of flakes were also characterized by Raman and PL spectroscopy. Figure 3.1f shows an optical micrograph image and Raman/PL intensity maps around the heterointerface. The A1g modes (410 cm^{-1}) of multilayer MoS_2 are observed only at the edges of WSe_2 in the intensity map. As shown in Figure 3.1g, the Raman spectra in the white flake exhibit multiple peaks in the region from 250 to 410 cm^{-1}, assigned to the Raman modes of WSe_2 (250, 256, 372, and 394 cm^{-1}) and MoS_2 (383 and 408 cm^{-1}). For this sample, the thickness of the MoS_2 on the WSe_2 flake is estimated to be more than 6 layers from the peak frequency difference of 25 cm^{-1} between the E^1_{2g} and A_{1g} modes.[105] This indicates that multilayer MoS_2 can be grown on the surface of WSe_2. At the edge of the WSe_2 flake, only the E^1_{2g} and A_{1g} peaks of MoS_2 are observed at 384 cm^{-1} and 408–410 cm^{-1}, respectively. Although only the MoS_2 Raman modes are also exhibited in the purple area of the optical micrograph image, the peak frequencies of both the E^1_{2g} and A_{1g} modes are shifted, and their difference is reduced from 26 cm^{-1} to 19 cm^{-1}. This indicates that the MoS_2 layer number decreases from multilayer to monolayer away from the WSe_2 flake.[105] The presence of monolayer MoS_2 is also supported by the PL map and spectra of the A-exciton at 1.83 eV (Figure 3.1f,h). The PL intensities slightly change depending on the measured spots due to inhomogeneous lattice strain, charged impurities, and structural defects of the CVD-grown crystal (Figure 3.2).[76, 83] Figure 3.2a,b shows optical micrograph images at another region on the WSe_2/MoS_2 sample in Figure 3.1. Figure 3.2c,d shows the PL map and spectra around the heterointerface in Figure 3.2b. The PL intensity of monolayer MoS_2 is relatively uniform, unlike the region in Figure 3.1. This indicates that the quality of the

CVD-grown MoS_2 on SiO_2 surface depends on the location of the sample. These results support the growth of multilayer MoS_2 from the edge and on the surface of the multilayer WSe_2, indicating the formation of multilayer-based in-plane and vertical heterostructures.

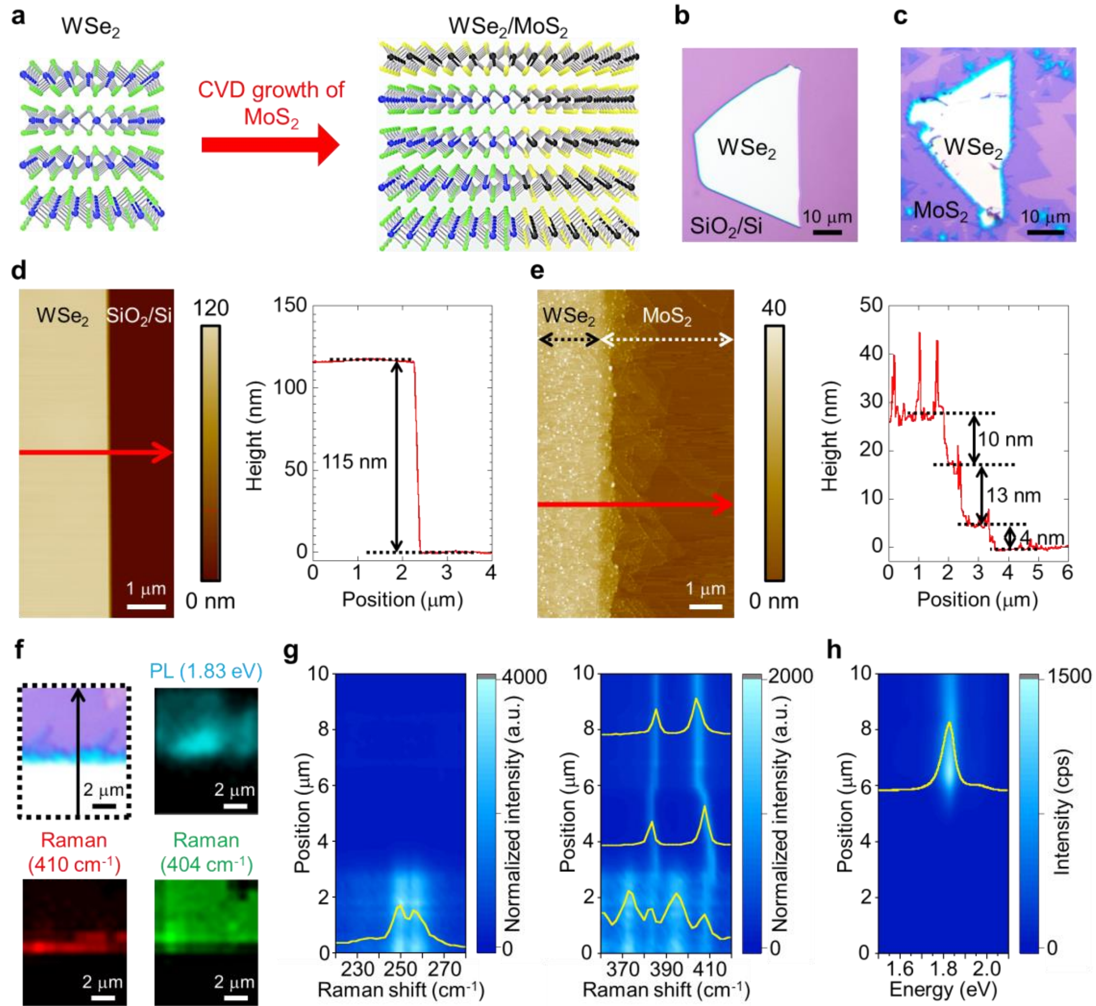

Figure 3.1 (a) Schematics of the fabrication of a multilayer WSe_2/MoS_2 heterostructure, where multilayer MoS_2 was grown from the edge and on the surface of multilayer WSe_2. The blue, black, green and yellow balls represent the W, Mo, Se and S atoms, respectively. Optical micrographs of (b) exfoliated WSe_2 and (c) the WSe_2/MoS_2 heterostructure. AFM images and height profiles of (d) exfoliated WSe_2 and (e) the WSe_2/MoS_2 heterostructure. The height profiles were measured along the red arrows in the AFM images. (f) Optical micrograph image and Raman/PL intensity maps around the WSe_2/MoS_2 heterointerface. Line scans of (g) Raman and (h) PL spectra of the WSe_2/MoS_2 flake measured at 0.2 mm intervals along the black arrow in (f). In (g), the Raman spectra were normalized at the intensity of MoS_2 A_{1g} mode.

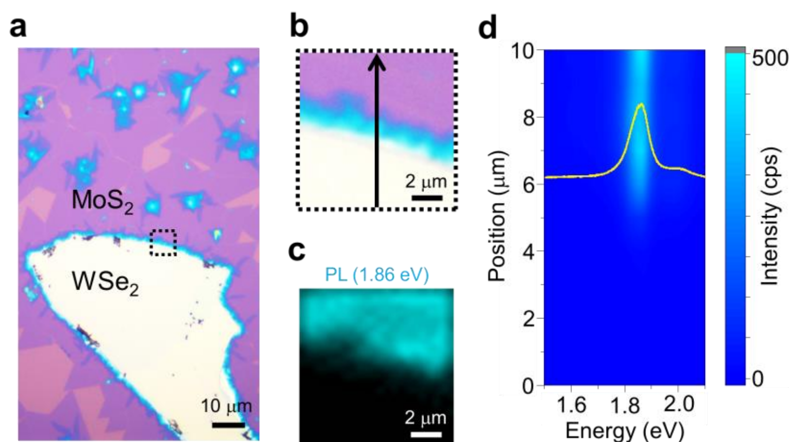

Figure 3.2 (a) Optical micrograph image at another region on the same WSe_2/MoS_2 sample in Figure 3.1. (b) Optical micrograph and (c) PL intensity map images around the WSe_2/MoS_2 heterointerface indicated by the dotted black square in (a). (d) Line scans of PL spectra of the WSe_2/MoS_2 measured along the black arrow in (b).

We confirmed that the growth temperature is an important factor to control the thickness uniformity of laterally-grown MoS_2. Figure 3.3 presents the optical micrograph images and Raman spectra of WSe_2/MoS_2 heterostructures grown at different growth temperatures of MoS_2. At 720 °C (Figure 3.3a), the Raman spectra of the white flake exhibit multiple peaks corresponding to the Raman modes of WSe_2 (249, 258, 372, and 395 cm^{-1}) and MoS_2 (383 and 408 cm^{-1}). The thickness of the MoS_2 on the WSe_2 flake is estimated to be more than 6 layers due to the peak frequency difference of 25 cm^{-1} between the E^1_{2g} and A_{1g} modes.[105] Similar vertical growth at 780 °C is also illustrated in Figure 3.3b for comparison. It is noteworthy that the width of laterally-grown multilayer MoS_2 increases from 1 mm at 720 °C (Figure 3.3a) to 4 mm at 780 °C (Figure 3.3b). These findings indicate that the growth temperature plays a significant role in enhancing the thickness uniformity of laterally-grown MoS_2.

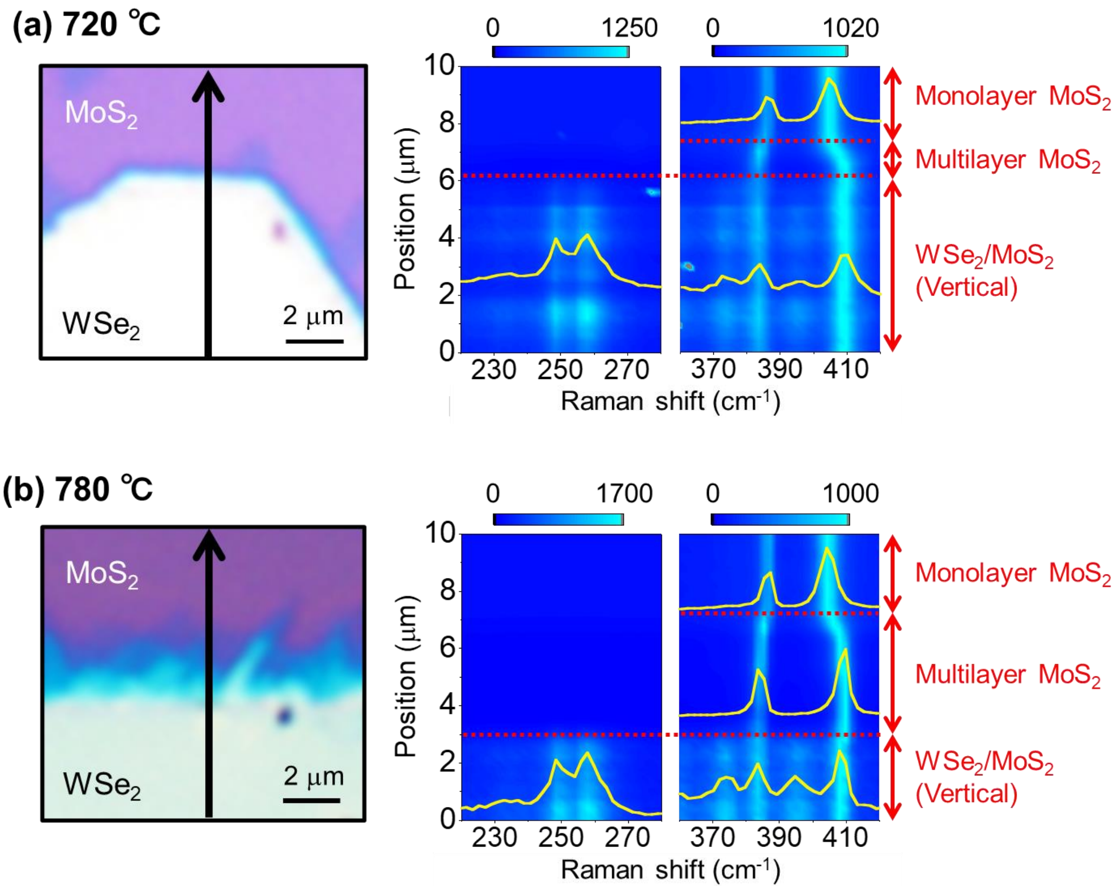

Figure 3.3 Optical micrograph images and Raman spectra of the WSe_2/MoS_2 heterostructures grown at (a) 720 °C and (b) 780 °C. The Raman spectra were measured at 0.2 mm intervals along the black arrows in the optical micrograph images. The Raman spectra were normalized at the intensity of MoS_2 A_{1g} mode.

To further confirm the interface structure of the in-plane heterostructures, we performed cross-sectional transmission electron microscopy (TEM) and high-angle annular dark field scanning transmission electron microscopy (HAADF-STEM) observations of the WSe_2/MoS_2 heterostructure. Figure 3.4a shows a TEM image of the WSe_2/MoS_2 heterostructure. The flake has a thickness of ~100 nm and has two different contrasts. The thickness of the flake decreases from four layers to a monolayer in the right region, as shown in Figure 3.4b,c.

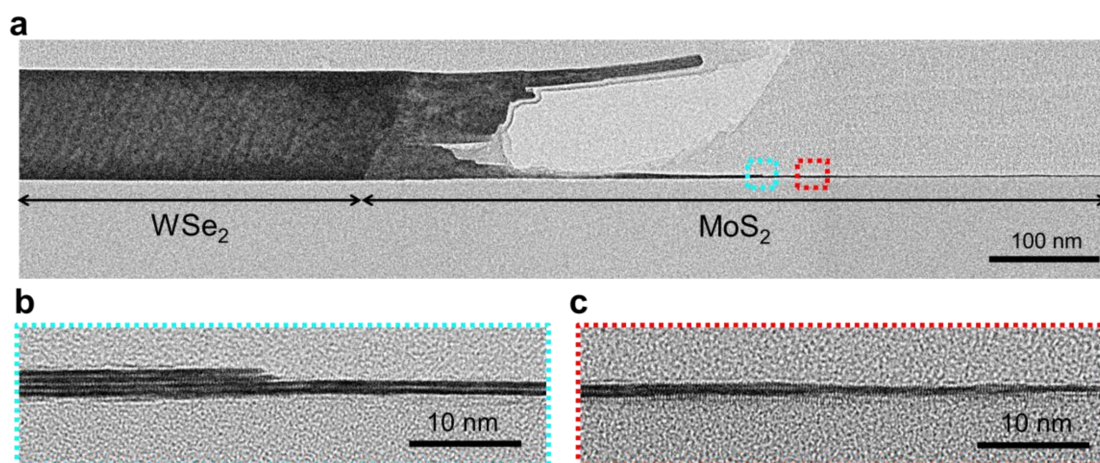

Figure 3.4 (a) Cross-sectional TEM image of the WSe_2/MoS_2 heterostructure. Cross-sectional TEM image of the MoS_2 areas indicated by the (b) dotted light blue and (c) red squares in Figure 3.4a.

Figures 3.5a shows HAADF-STEM images around the interface with different contrasts. The bright and dark contrasts correspond to the WSe_2 and MoS_2 regions, respectively, because the contrast of the HAADF-STEM image is roughly proportional to the nth power of the atomic number (Z^n).[106] The presence of WSe_2 and MoS_2 is also confirmed by energy-dispersive X-ray spectroscopy (EDS) mapping (Figure 3.5b). In the EDS maps, the left and right regions contain W/Se and Mo/S atoms, respectively, and there is an abrupt composition change across the interface. Figure 3.5c shows the high-resolution HAADF-STEM image at the lower part of the heterostructure in contact with the substrate surface. The multilayer MoS_2 grows from the edge of the WSe_2, presenting the formation of in-plane heterostructures of multilayer TMDCs with an abrupt change of composition. It is noted that the abrupt composition change occurs within ~2 nm as confirmed by the intensity profiles of HAADF-STEM images (Figure 3.5d−g). These results are consistent with the Raman and PL results in Figure 3.1f−h.

The TEM and HAADF-STEM images also provide additional features of the present multilayer-based heterostructures. First, the present WSe_2 has 2H stacking, and the same stacking structure can also be seen for MoS_2 (Figure 3.5h,i). This indicates epitaxial growth of MoS_2, as observed for the growth of monolayer in-plane heterostructures. Second, we also found that a dislocation is formed in MoS_2 due to a 5 % lattice mismatch of the c-axis between MoS_2 (1.23 nm) and WSe_2 (1.296 nm),[107, 108] which is indicated by the yellow arrow in Figure 3.5i. We note that the misfit dislocation should also be introduced within each monolayer due to 4% the lattice mismatch of bulk MoS_2 (0.315 nm)[107] and bulk WSe_2 (0.328 nm)[108] as well as the case of monolayer in-plane heterostructures.[69, 76]

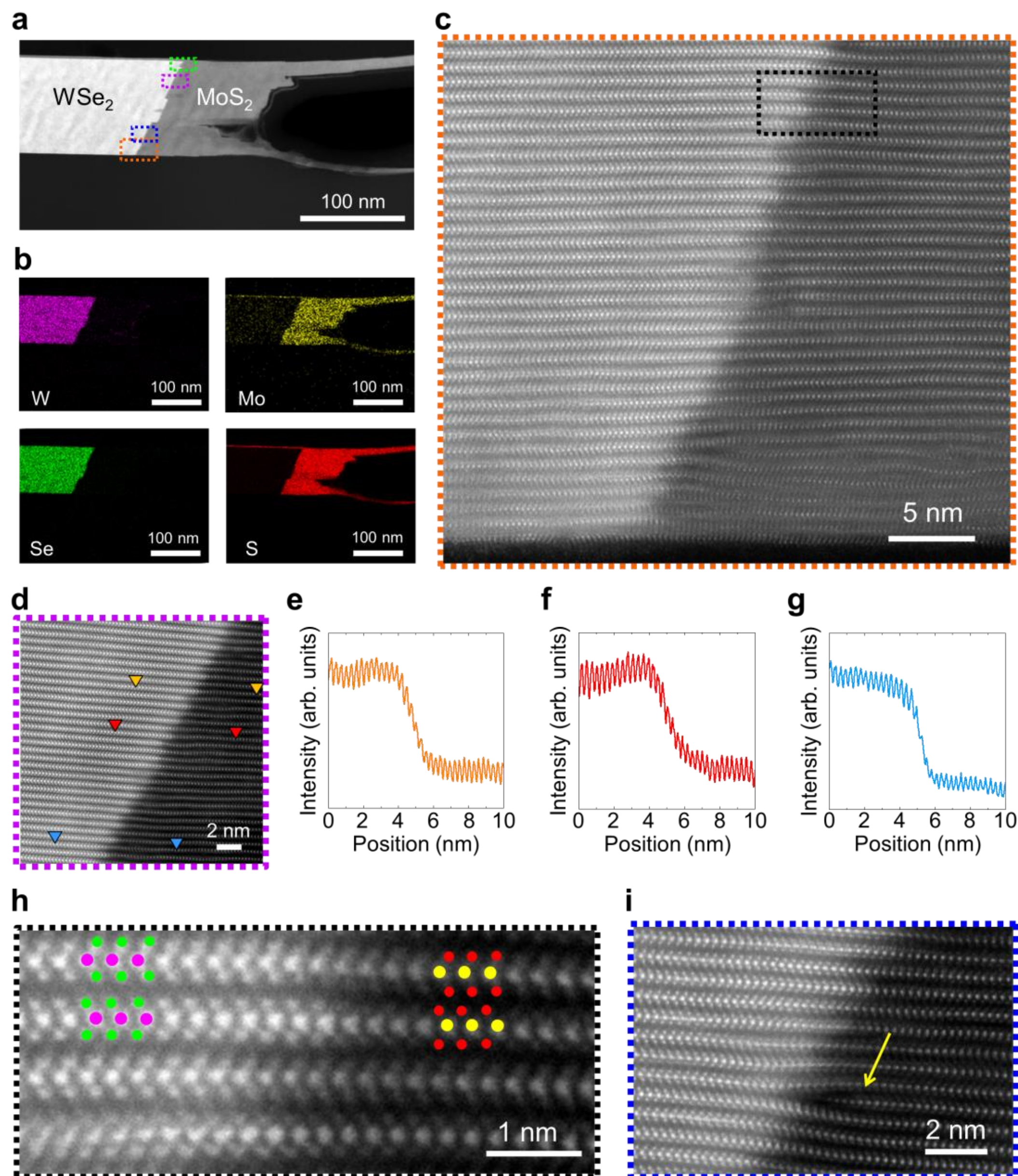

Figure 3.5 (a) Cross-sectional HAADF-STEM image of the WSe_2/MoS_2 heterostructure. (b) EDS mapping images for W-L, Se-K, Mo-K, and S-K lines in the same area as Figure 3.5a. (c) High-resolution HAADF-STEM image at the lower part of the heterointerface. (d) High-resolution HAADF-STEM images at the heterointerface indicated by the dotted purple square. Intensity profiles of the HAADF-STEM image measured at the regions between (e) orange, (f) red, and (g) blue triangles in Figure 3.5d. (h) Atomic-resolution HAADF-STEM image at the heterointerface indicated by the dotted black square in Figure 3.5c The pink, green, yellow, and red dots correspond to W, Se, Mo, and S atoms, respectively. (i) High-resolution HAADF-STEM images at the heterointerface indicated by the dotted blue squares in Figure 3.5a. The yellow arrow indicates a dislocation of MoS_2.

Moreover, the HAADF-STEM images and EDS mapping reveal that trilayer MoS_2 was grown on top of WSe_2 (Figures 3.5b and 3.6), presenting the formation of multilayer-based vertical heterostructures in addition to in-plane heterostructures. Figure 3.6b,c shows a high-resolution HAADF-STEM images around the top of the WSe_2 flake and indicates the growth of trilayer MoS_2 on WSe_2. The vertical growth of MoS_2 on WSe_2 is probably derived from the surface diffusion and nucleation of precursors on the exfoliated flakes. Similar vertical growth has been demonstrated under high concentrations of metal precursors.[109] It is noteworthy that this vertical growth of MoS_2 could be suppressed by the surface passivation of the WSe_2 flakes with insulating films such as SiO_2.

The diffusion of precursors on the flakes also introduces more extended lateral growth at the top layers compared to the middle layers (Figures 3.4a and 3.5a). This morphology is different from the uniform multilayers of SnS/GeS in-plane heterostructures.[86, 87] This implies that the growth mechanism of present MoS_2 differs from that of GeS grown from SnS on mica substrates. In the case of SnS/GeS heterostructures, the GeS vapor seems to have a much higher affinity to the{110} edge facets of SnS than the surfaces of SnS and mica substrates utilized. This is also supported by the fact that homogeneous nucleation has never been observed for pure GeS crystals on mica substrates. In contrast, in the present study, pure MoS_2 can also nucleate even on the surfaces of SiO_2 and WSe_2 due to the strong affinity of MoS_2 precursors to these surfaces. The control affinity may serve as a crucial means of enhancing the uniformity of multilayer growth in the in-plane heterostructures, in addition to the growth temperature as depicted in Figure3.3. We note that the growth rates of top layers could be influenced by the surface area and edge facet structure of exfoliated flakes because the structures of CVD-grown MoS_2 are different between WSe_2 and $Nb_xMo_{1-x}S_2$ flakes (Figures 3.4a and 3.11a). In this study, the multilayer WSe_2 flake has the slanted edge due to the mechanical exfoliation process (Figures 3.4a and 3.5a). In contrast, in previous works, seed flakes were prepared by vapor growth process. For example, the multilayer SnS/GeS was fabricated by GeS growth from the edges of the pre-synthesized SnS seed flakes, resulting in the formation of vertical edge facet.[86, 87] To create similar vertical edge facets, it would be effective to adapt the same two-step growth process or area-selective plasma etching of exfoliated flakes.[110]

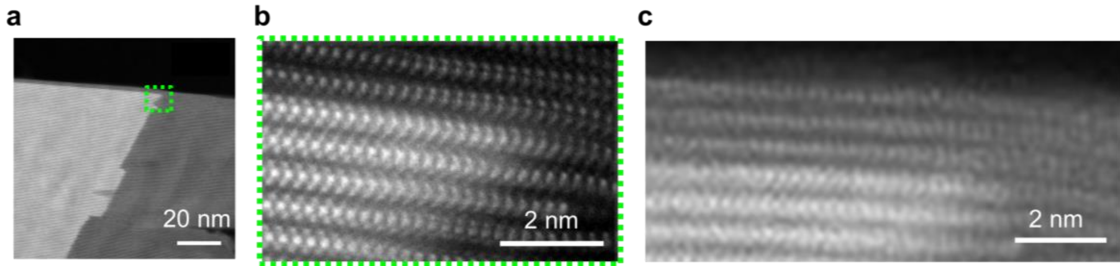

Figure 3.6 (a) Cross-sectional HAADF-STEM image at the higher part of the WSe_2/MoS_2 heterointerface. (b) Atomic-resolution HAADF-STEM image at the heterointerface indicated by the dotted light green square. (c) High-resolution HAADF-STEM images at the same area as Figure 3.6b

Electronic transport properties

To investigate the electrical transport properties of the WSe_2, MoS_2, and WSe_2/MoS_2 heterostructures, back-gate FETs with Au/In electrodes were fabricated on SiO_2/Si substrates as shown in Figure 2.6d. Figure 3.7 shows the temperature-dependent I_d-V_g and I_d-V_d curves of the exfoliated multilayer WSe_2, CVD-grown monolayer MoS_2, and CVD-grown multilayer MoS_2. The exfoliated multilayer WSe_2 exhibits ambipolar characteristics at all temperature conditions (Figure 3.7a). In contrast, The FETs of CVD-grown monolayer and multilayer MoS_2 exhibit typical n-type characteristics (Figure 3.7b,c); the corresponding FET of monolayer MoS_2 exhibits an electron mobility of 12 $cm^2V^{-1}s^{-1}$ and an on/off ratio of 10^7 for an applied V_g ranging from −50 to 50 V at 300 K. These values are comparable to those of previous studies,[111, 112] which supports the high quality of MoS_2 grown by the present CVD growth. The decreases in the drain current are caused by high contact resistance, which is supported by the nonlinear I_d-V_d curves at low temperatures (Figure 3.7d−f)

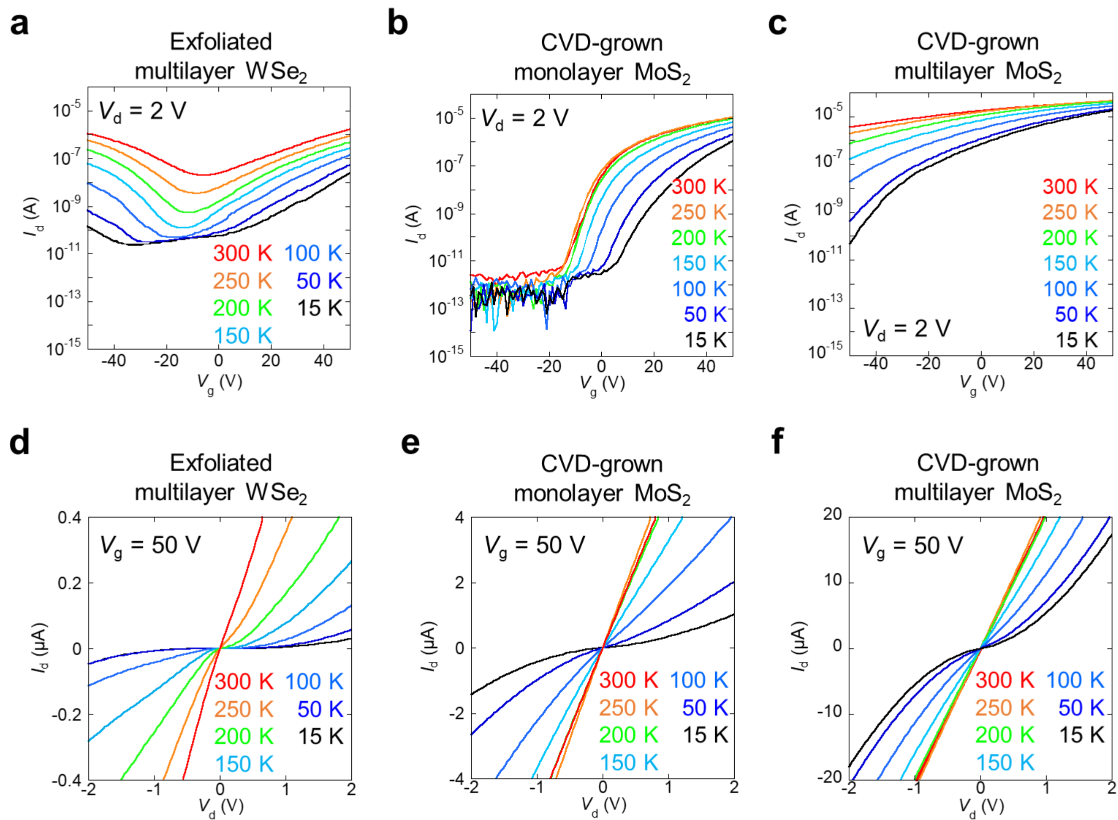

Figure 3.7 Temperature-dependent I_d-V_g curves of (a) exfoliated multilayer WSe_2, (b) CVD-grown monolayer MoS_2, (c) CVD-grown multilayer MoS_2. Temperature-dependent I_d-V_d curves of (d) exfoliated multilayer WSe_2, (e) CVD-grown monolayer MoS_2, (f) CVD-grown multilayer MoS_2. The devices were fabricated for the samples after MoS_2 CVD.

Figure 3.8 a,b shows a schematic and optical micrograph images of the WSe_2/MoS_2 device with Au/In electrodes and a SiO_2/Si substrate. Figure 3.8c shows the I_d-V_d characteristics at different V_g and 15 K. For $V_g < 0$ V, I_d is less than 10^{-11} A because monolayer MoS_2 is in the off state (Figure 3.7b). For $V_g > 0$ V, the drain current increases with increasing gate voltage because electrons are doped into both WSe_2 and MoS_2 by positive gate voltages. However, electronic characteristics derived from electron tunneling is not observed because the multilayer WSe_2 is a nondegenerate ambipolar semiconductor (Figure 3.7a). Figure 3.8d–f shows the temperature dependence of the I_d-V_d and I_d-V_g curves. The drain current decreases with decreasing temperature, which is due to the temperature-dependent contact resistance (Figure 3.7d–f). Furthermore, at high temperatures, the drain current decreases for V_g ranging from −20 V to −10 V (Figure 3.8e,f). This result reflects the high resistive state of ambipolar WSe_2 (Figure 3.7a).

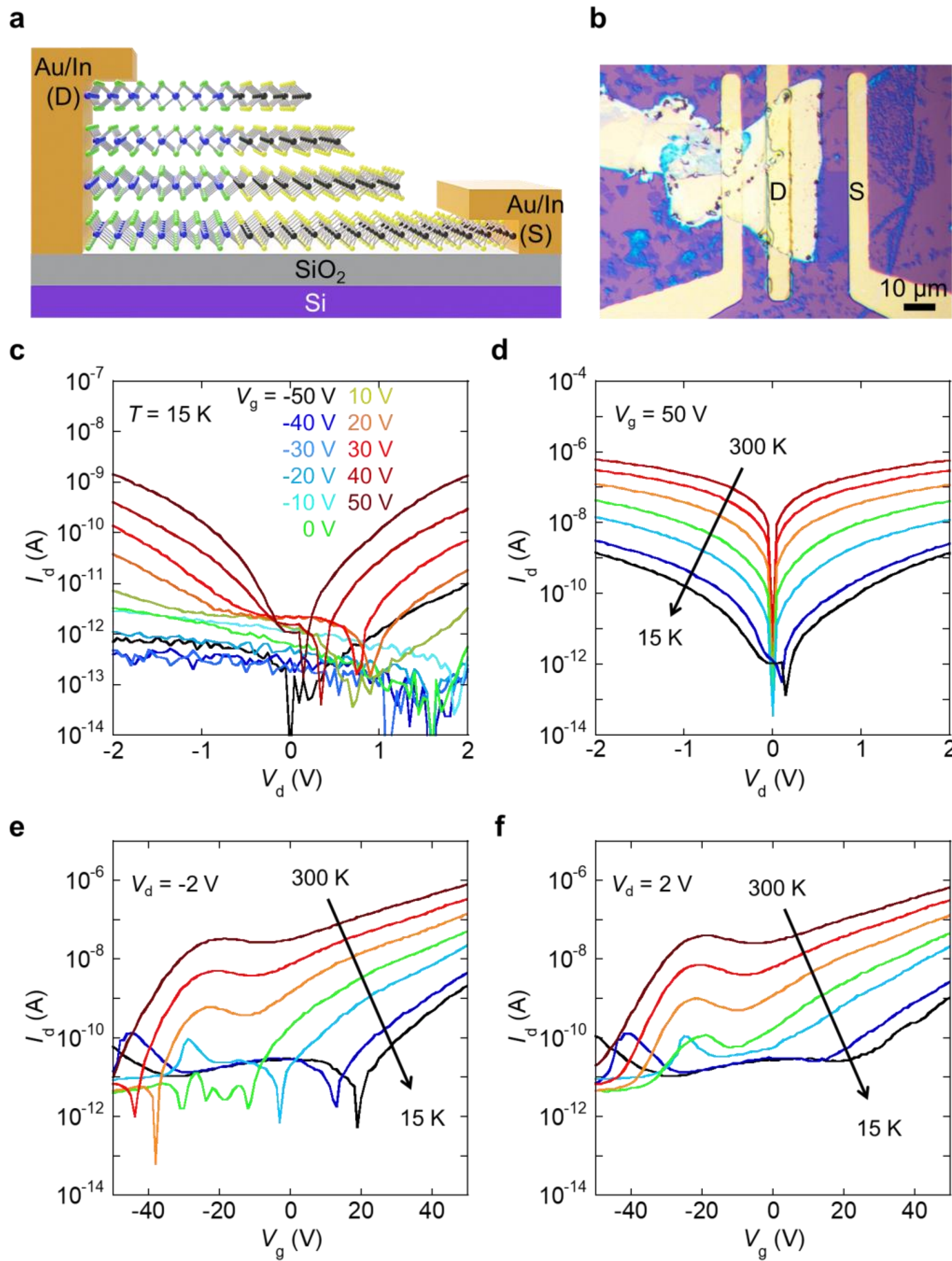

Figure 3.8 (a) Schematic and (b) optical micrograph images of the WSe_2/MoS_2 heterostructure device. (c) I_d-V_d curves of the WSe_2/MoS_2 heterostructure at different V_g and 15 K. (d) Temperature-dependent I_d-V_d curves of the WSe_2/MoS_2 heterostructure at $V_g = 50$ V. Temperature-dependent I_d-V_g curves of the WSe_2/MoS_2 heterostructure at (e) $V_d = -2$ V and (f) +2 V (15, 50, 100, 150, 200, 250 and 300 K).

3.3.2 Multilayer $Nb_xMo_{1-x}S_2/MoS_2$ Heterostructures.

Structure analysis

Figure 3.9a shows a schematic image of the present growth process of the multilayer $Nb_xMo_{1-x}S_2/MoS_2$ in-plane heterostructure. Similar to WSe_2/MoS_2, CVD growth of MoS_2 was conducted after exfoliation of multilayer $Nb_xMo_{1-x}S_2$ flakes (Figure 3.9b,c). The exfoliated $Nb_xMo_{1-x}S_2$ flake shows an abrupt change in height, whereas step-like height profiles can be obtained for $Nb_xMo_{1-x}S_2/MoS_2$ due to the CVD growth of multilayer MoS_2, as observed by AFM (Figure 3.9d,e). Figure 3.9f shows an optical micrograph image and Raman/PL intensity maps around the heterointerface. The A_{1g} Raman mode (410 cm^{-1}) of multilayer MoS_2 with moderate thickness presents high intensity around the edge of $Nb_xMo_{1-x}S_2$ flake in the intensity map. We note that the white flake shows the weak Raman intensity due to its sufficiently-thick multilayered structure. The E^1_{2g} and A_{1g} peaks of MoS_2 are observed at 383 cm^{-1} and 408−410 cm^{-1}, respectively, throughout the flakes (Figure 3.9g). In the purple area in Figure 3.9f, the difference in the peak frequencies of the E^1_{2g} and A_{1g} modes is approximately 19 cm^{-1}, and strong PL of the A-exciton is observed at 1.80 eV (Figure 3.9f,h). This also illustrates that the layer number of the CVD-grown MoS_2 decreases from multilayer to monolayer, as observed for WSe_2/MoS_2.

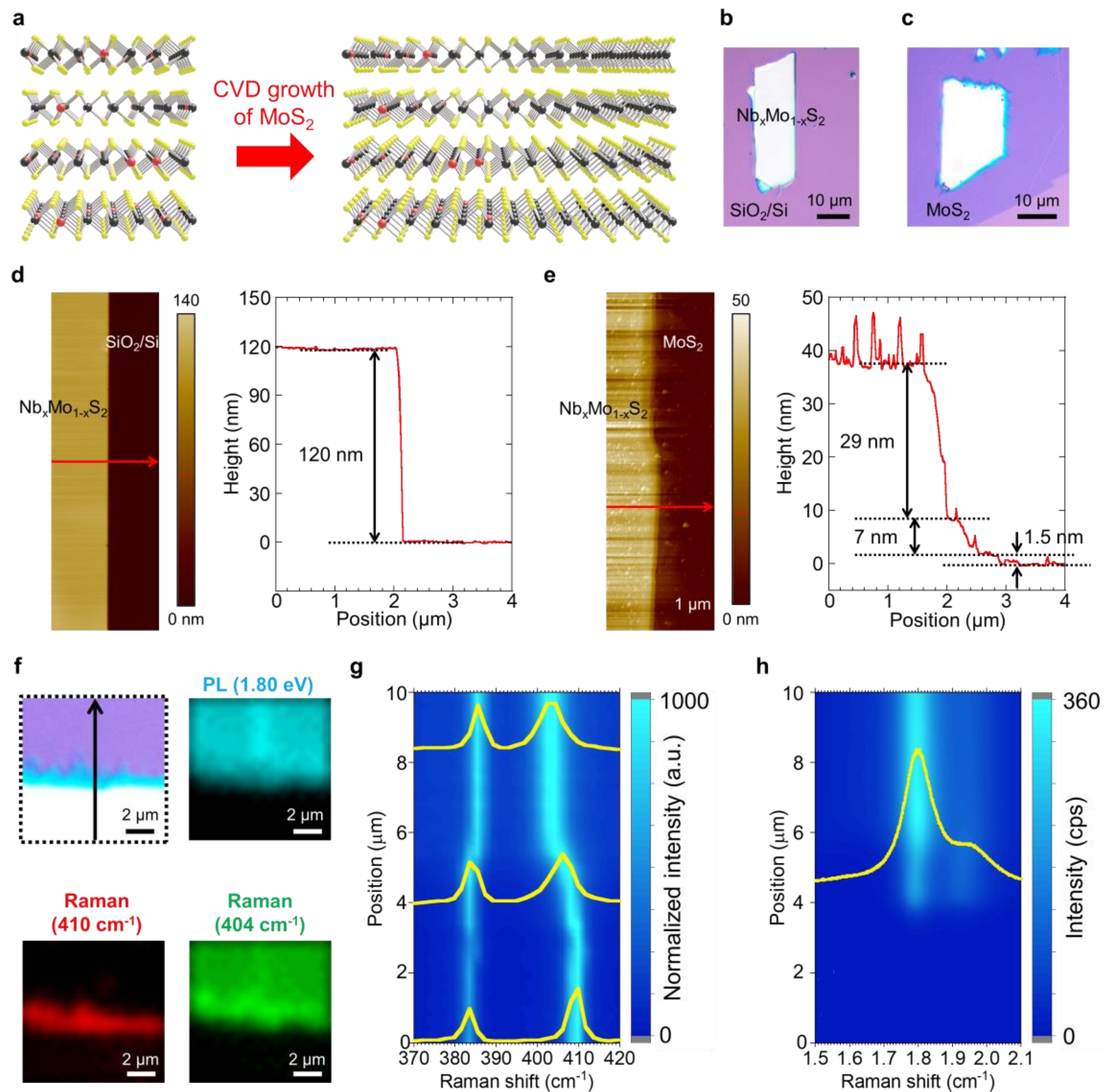

Figure 3.9 (a) Schematics of the fabrication of a multilayer $Nb_xMo_{1-x}S_2/MoS_2$ in-plane heterostructure, where multilayer MoS_2 was grown from the edge of multilayer $Nb_xMo_{1-x}S_2$. Black, red and yellow balls represent the Mo, Nb and S atoms, respectively. Optical micrograph images of (b) an exfoliated $Nb_xMo_{1-x}S_2$ flake and (c) the $Nb_xMo_{1-x}S_2/MoS_2$ heterostructure. AFM images and height profiles of the (d) exfoliated $Nb_xMo_{1-x}S_2$ flake and (e) $Nb_xMo_{1-x}S_2/MoS_2$ heterostructure. The height profiles were measured along the red arrow in AFM images. (f) Optical micrograph and Raman/PL intensity maps around the of $Nb_xMo_{1-x}S_2/MoS_2$ heterointerface. Line scans of (g) Raman and (h) PL spectra of the $Nb_xMo_{1-x}S_2/MoS_2$ flake measured at 0.2 mm intervals along the black arrow in (f). In (g), the Raman spectra were normalized at the intensity of A_{1g} mode.

We investigated the temperature dependence of the thickness uniformity of MoS_2 grown from the $Nb_xMo_{1-x}S_2$ flakes as well as the case of the multilayer WSe_2/MoS_2 heterostructures (Figure 3.3). Figure 3.10 shows the optical micrograph images of $Nb_xMo_{1-x}S_2/MoS_2$ heterostructures grown at different growth temperatures of MoS_2. At 700 °C, the width of multilayer MoS_2 (blue areas in Figure 3.10) from the $Nb_xMo_{1-x}S_2$ edges is less than 1 mm. The multilayer MoS_2 becomes larger above 750°C (blue areas in Figure 3.10b). At 780 °C and 850 °C, the thick multilayer MoS_2 (white areas in Figure 3.10c,d) along the $Nb_xMo_{1-x}S_2$ edge can be observed, suggesting the increase of the multilayer MoS_2 thickness at higher temperatures. These results indicate that the growth temperature is a major factor to improve the uniformity of MoS_2 thickness. The staircase-like structure of MoS_2 can be explained by the growth process governed by the surface diffusion of precursors. The bottom monolayer MoS_2 tends to be larger probably due to the efficient incorporation of surface-diffused atoms. In contrast, the incorporation rate of diffused atoms should be lower for the upper layers because they are farther away from the substrate. This scenario agrees with the increased thickness of MoS_2 at higher temperatures. At higher temperatures, the diffused atoms with high kinetic energy could easily climb the bottom MoS_2 edges and reach the upper MoS_2 layers.

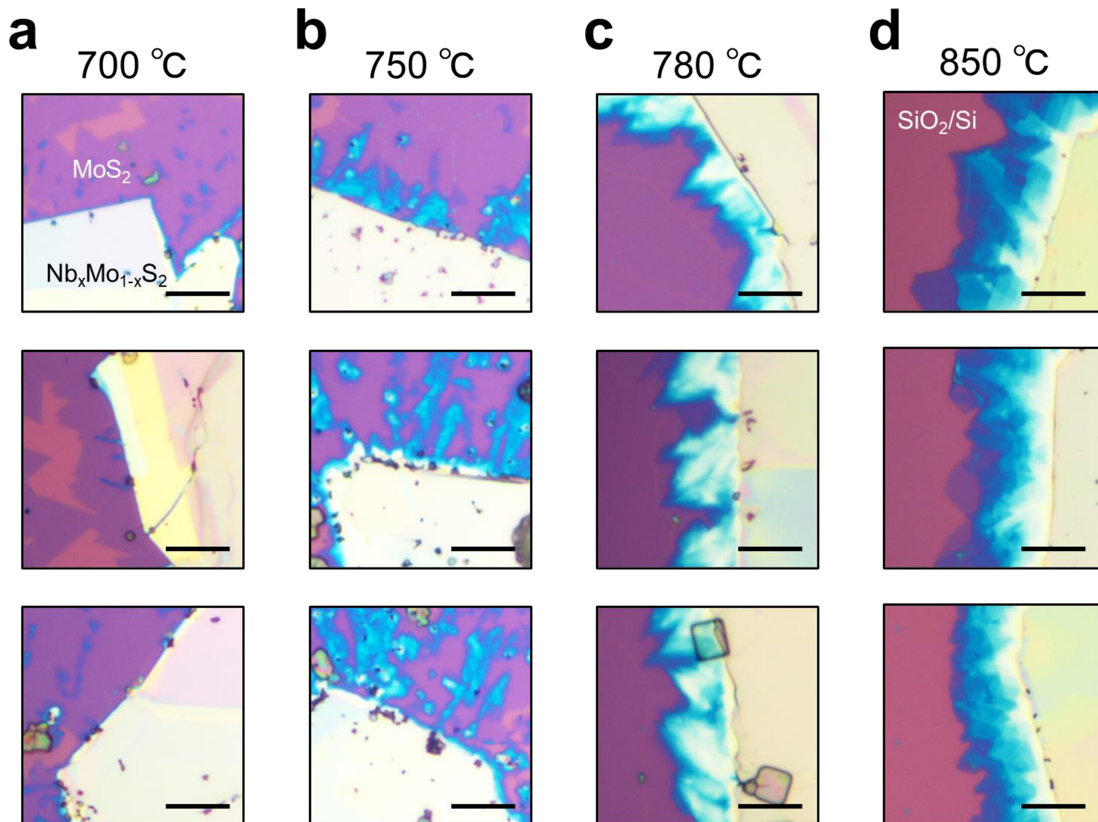

Figure 3.10 Optical micrograph images of $Nb_xMo_{1-x}S_2/MoS_2$ grown at (a) 700 °C, (b) 750 °C, (c) 780 °C, and (d) 850 °C. Scale bars are 10 µm.

We also performed cross-sectional TEM and HAADF-STEM observations of the $Nb_xMo_{1-x}S_2/MoS_2$ heterostructure (Figure 3.11a–d). The thickness of the flake decreases from 35 nm on the left to 0.7 nm on the right, supporting MoS_2 growth from the flake edge of $Nb_xMo_{1-x}S_2$, similar to the case of WSe_2 flakes. These images are consistent with the formation of multilayer $Nb_xMo_{1-x}S_2/MoS_2$ in-plane heterostructures supported by PL/Raman and AFM measurements (Figure 3.9). We note that observing the heterointerface in the STEM image (Figure 3.11b) and EDS mapping (Figure 3.11e–g) is difficult because of the close atomic numbers of Nb (Z = 41) and Mo (Z = 42).

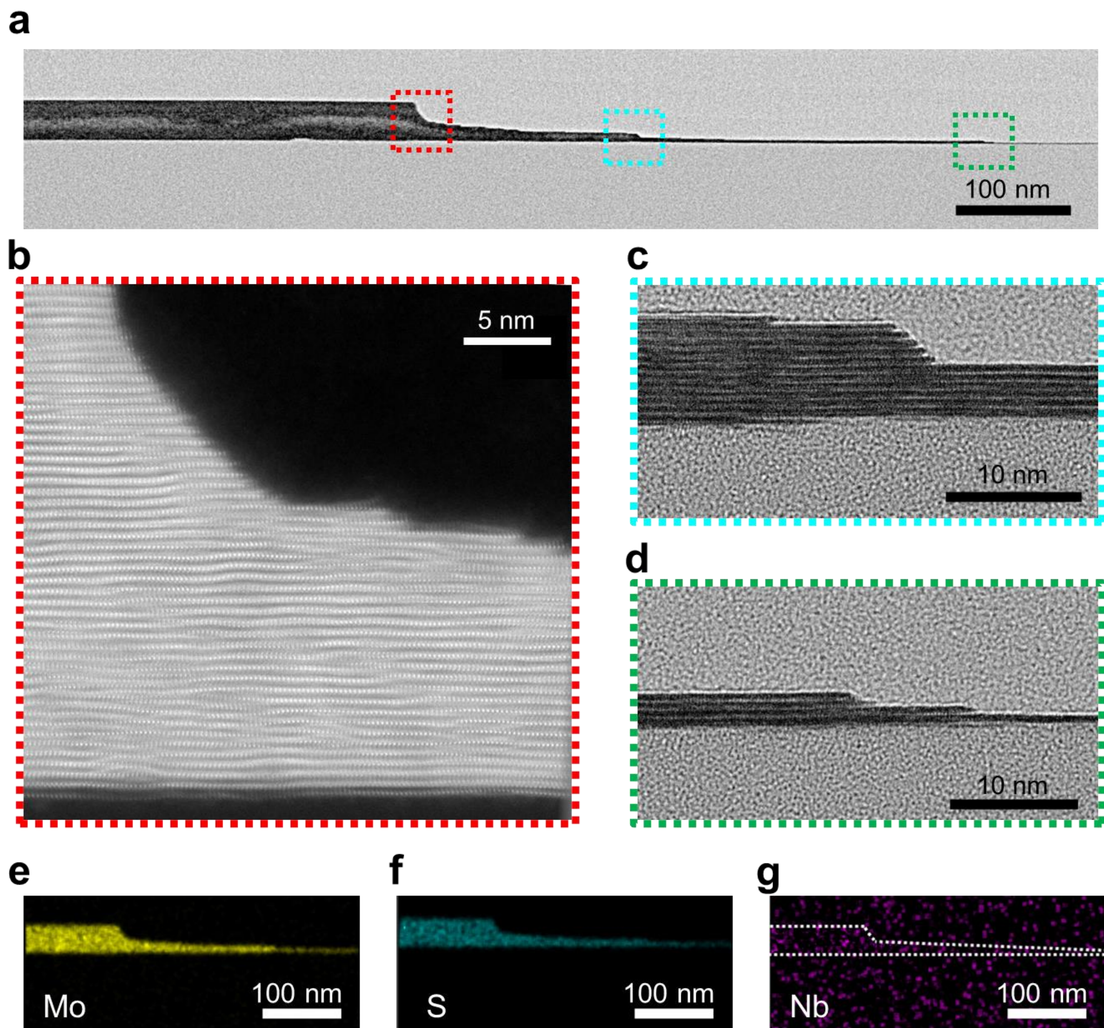

Figure 3.11 (a) Cross-sectional TEM image of the $Nb_xMo_{1-x}S_2/MoS_2$ heterostructure. (b) High-resolution cross-sectional HAADF-STEM image of the area indicated by the dotted red square in Figure 3.11a. (c, d) Cross-sectional TEM image of the area indicated by the (c) dotted light blue and (d) green squares in Figure 3.11a. EDS maps for (e) Mo, (f) S, and (g) Nb throughout the heterostructure.

To estimate the Nb concentration in the bulk $Nb_xMo_{1-x}S_2$ crystal, we performed XRF measurements of the bulk crystals of $Nb_xMo_{1-x}S_2$, MoS_2 (SPI Supplies), and NbS_2 (HQ Graphene), as shown in Figure 3.12. The XRF peaks can be assigned to Nb-Kα (16.6 keV), Mo-Kα (17.4 keV), Nb-Kβ (18.6 keV), and Mo-Kβ (19.6 keV) lines, respectively. The $Nb_xMo_{1-x}S_2$ crystal exhibits both Nb-Ka and Mo-Ka peaks, indicating that Nb and Mo coexist in the $Nb_xMo_{1-x}S_2$ crystal. The Nb/(Nb+Mo) molar ratio of the $Nb_xMo_{1-x}S_2$ crystal is estimated to be ~ 0.1 %.

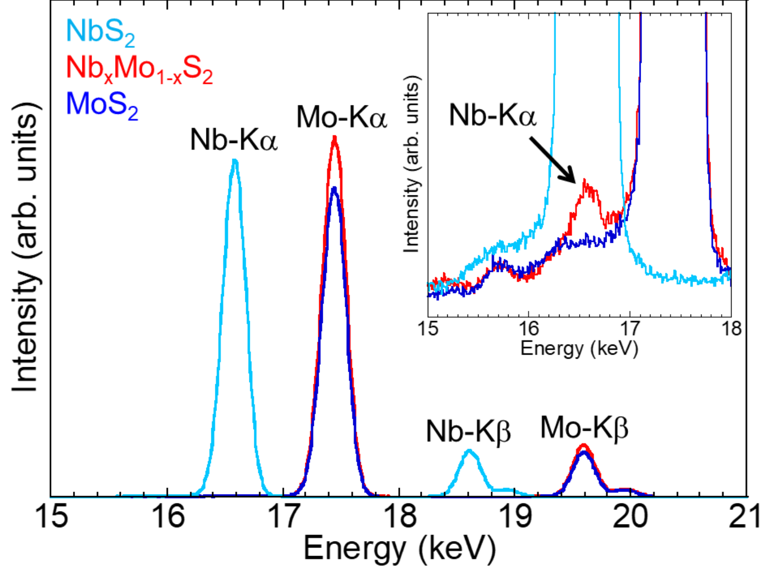

Figure 3.12 XRF spectra of the bulk $Nb_xMo_{1-x}S_2$, MoS_2, and NbS_2 crystals. The inset is an enlarged view of the Nb-Kα and Mo-Kα peaks.

The density of Nb atoms in the $Nb_xMo_{1-x}S_2$ crystals was estimated to be 1.9×10^{19} cm^{-3} from the Nb/(Nb+Mo) molar ratio of *ca*. 0.1% and the lattice constants of bulk MoS_2. For multilayer $Nb_xMo_{1-x}S_2$ crystals, almost all Nb acceptors are probably fully ionized due to the absence of a carrier freeze-out region.[24] For the position of Fermi level ($E_F - E_v$) of the $Nb_xMo_{1-x}S_2$ crystals, the hole density was calculated as follows:

$$p = \int_{-\infty}^{E_v} D_v(E)\{1 - f(E)\}dE \qquad (3.1)$$

where $D_v(E) = 4\pi \left(\frac{2m_p{}^*}{h^2}\right)^{\frac{3}{2}} (E_v - E)^{\frac{1}{2}}$ is density of states and $f(E) = \frac{1}{1+e^{\frac{E-E_F}{k_BT}}}$ is the Fermi-Dirac distribution. Here, $m_p{}^* = 0.68m_0$ is the effective hole mass of MoS_2.[24]
Therefore,

$$p = \int_{-\infty}^{E_v} D_v(E)\{1 - f(E)\}dE$$

$$= \int_{-\infty}^{E_v} 4\pi \left(\frac{2m_p{}^*}{h^2}\right)^{\frac{3}{2}} (E_v - E)^{\frac{1}{2}} \frac{e^{\frac{E-E_F}{k_BT}}}{1 + e^{\frac{E-E_F}{k_BT}}} dE \quad (3.2)$$

If $E_v - E = E'$, then

$$p = \int_{0}^{\infty} 4\pi \left(\frac{2m_p{}^*}{h^2}\right)^{\frac{3}{2}} (E')^{\frac{1}{2}} \frac{e^{\frac{E_v-E_F-E'}{k_BT}}}{1 + e^{\frac{E_v-E_F-E'}{k_BT}}} dE' = \int_{0}^{\infty} P(E')dE' \quad (3.3)$$

Figure 3.13a shows some examples of $P(E')$ assuming the value of $E_v - E_F$. The hole density of the $Nb_xMo_{1-x}S_2$ crystals can be calculated by integrating $P(E')$. Figure 3.13b shows the $E_F - E_v$ at 300 K and 15 K as a function of calculated hole density. The density of Nb atoms in the $Nb_xMo_{1-x}S_2$ crystals exceeds the calculated hole density at $E_F - E_v = 0$ eV, which suggests degenerate hole doping for these samples. Furthermore, the non-degenerate limit of hole density at $E_F = E_v + 3k_BT$ can be estimated by a parabolic valence-band model as follows:

$$p_{E_F=E_v+3k_BT} = 2\left(\frac{2\pi m_p{}^* k_BT}{h^2}\right)^{\frac{3}{2}} e^{-3} \quad (3.4)$$

Figure 3.13c shows the temperature dependence of the non-degenerate limit of the hole density. The density of Nb atoms exceeds the value of the non-degenerate limit. This calculation also supports degenerate hole doping for the present samples.

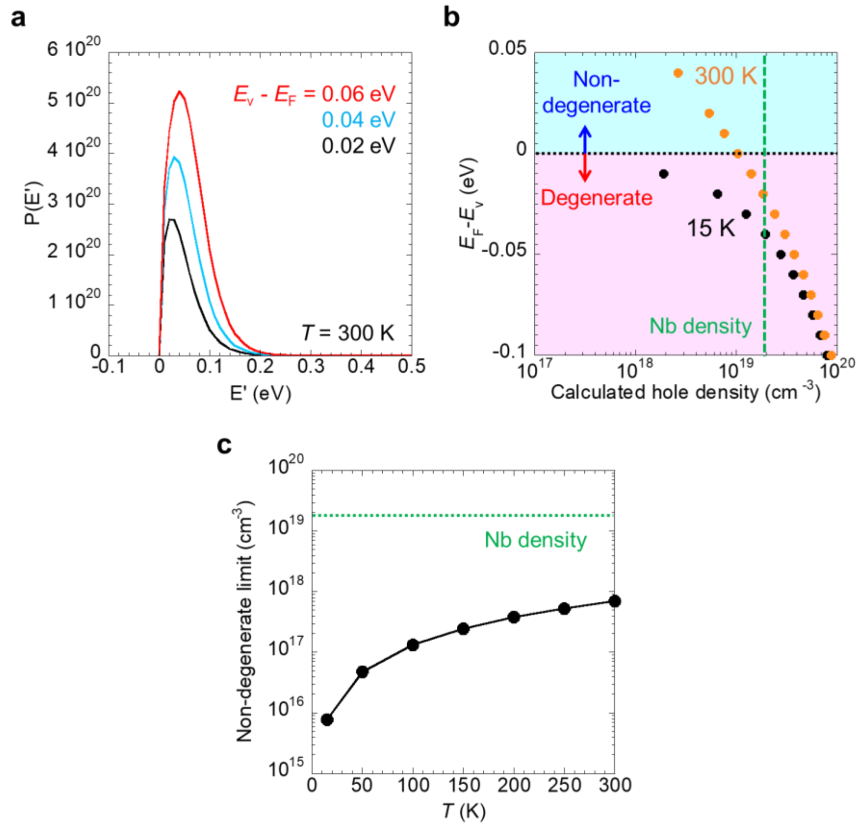

Figure 3.13 (a) Some examples of $P(E')$ assuming the values of $E_v - E_F$ (0.02, 0.04, and 0.06 eV). (b) Calculated hole densities at 300 K and 15 K as a function of $E_v - E_F$. (c) Temperature dependence of the non-degenerate limit of the hole density.

Electronic transport properties

In this section, we focus our attention on the transport properties of the $Nb_xMo_{1-x}S_2$, MoS_2 and $Nb_xMo_{1-x}S_2/MoS_2$ heterostructures. We fabricated the back-gate FETs as well as the case of the WSe_2/MoS_2 devices. As shown in Figure 3.14a, the drain current of multilayer $Nb_xMo_{1-x}S_2$ exhibits almost no gate voltage (V_g) dependence due to degenerate hole doping.[24] The drain current decreases with decreasing temperature (Figure 3.14). This is probably caused by impurity scattering.[24] In contrast, multilayer MoS_2 exhibits n-type characteristics as shown in Figure 3.7c.

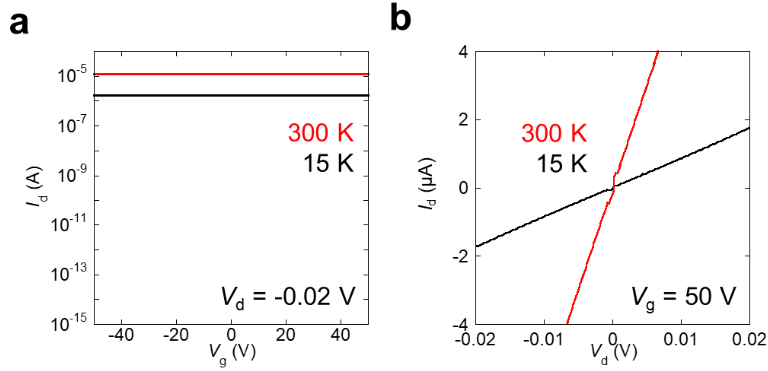

Figure 3.14 Temperature-dependent (a) I_d-V_g and (b) I_d-V_d curves of exfoliated multilayer $Nb_xMo_{1-x}S_2$.

Figure 3.15a,b shows schematic and optical micrograph images of the representative $Nb_xMo_{1-x}S_2/MoS_2$ device. Assuming similar n-type properties for multilayer MoS_2 grown from a $Nb_xMo_{1-x}S_2$ flake, we can expect a change in the band diagram for the present $Nb_xMo_{1-x}S_2/MoS_2$ heterostructures from a staggered gap to a broken gap induced by electron doping of MoS_2 (Figure 3.15c). In this case, a tunneling current flows at the heterointerface when applying a drain voltage (V_d), as shown in the band diagrams (Figure 3.15d). Briefly, when a negative drain voltage is applied, electrons tunnel from the valence band of $Nb_xMo_{1-x}S_2$ to the conduction band of MoS_2. At a small positive drain voltage, the drain current (I_d) is based on electron tunneling from the conduction band of MoS_2 to the valence band of $Nb_xMo_{1-x}S_2$. This tunneling current reaches its peak at the peak voltage (V_p) because of the maximized overlap between the occupied conduction band states of MoS_2 and unoccupied valence band states of $Nb_xMo_{1-x}S_2$. Further increases in the drain voltage lead to decreases in the tunneling current until the valley voltage (V_v) due to the decrease in the overlap. When a high voltage is applied, the drain current is based on the diffusion current, and the drain current monotonically increases with increasing drain voltage. This can be observed as the negative differential resistance (NDR) in the current-voltage curves for the tunnel diodes.[2, 47, 49, 113]

Figure 3.15e shows the I_d-V_d curves of the $Nb_xMo_{1-x}S_2/MoS_2$ device at different V_g and 15 K under vacuum. For $V_g = 0$ V, I_d is less than 10^{-13} A because of the high resistivity of MoS_2 without electron doping, as observed in the individual monolayer MoS_2 (Figure 3.7b). For $V_g > 10$ V, we can observe the reverse current due to electron tunneling from the valence band of $Nb_xMo_{1-x}S_2$ to the conduction band of MoS_2. For $V_g = 50$ V, an NDR trend (a iinflection in the I_d-V_d curves) is observed for forward bias, which may indicate a transition from the electron tunneling current to the diffusion current. In addition to the NDR trend, the onset voltage of the electron tunneling current at reverse bias is zero, which indicates that the band alignment for $Nb_xMo_{1-x}S_2/MoS_2$ is a

broken gap alignment. To further investigate the NDR trend, the temperature dependence of the I_d-V_d curves at V_g = 50 V is shown in Figure 3.15f. The NDR trend can be observed at T < 50 K. At T > 100 K, the NDR trend disappears because thermally excited carriers are generated at the heterointerface. In particular, the recombination current that competes with the tunneling process appears at high temperatures. A similar temperature dependence of NDR is also observed in previous studies of TMDC-based tunnel diodes.[29, 46, 48, 53] We note that the NDR trend also suggests that the n-type MoS_2 region is lightly doped.[3, 52]

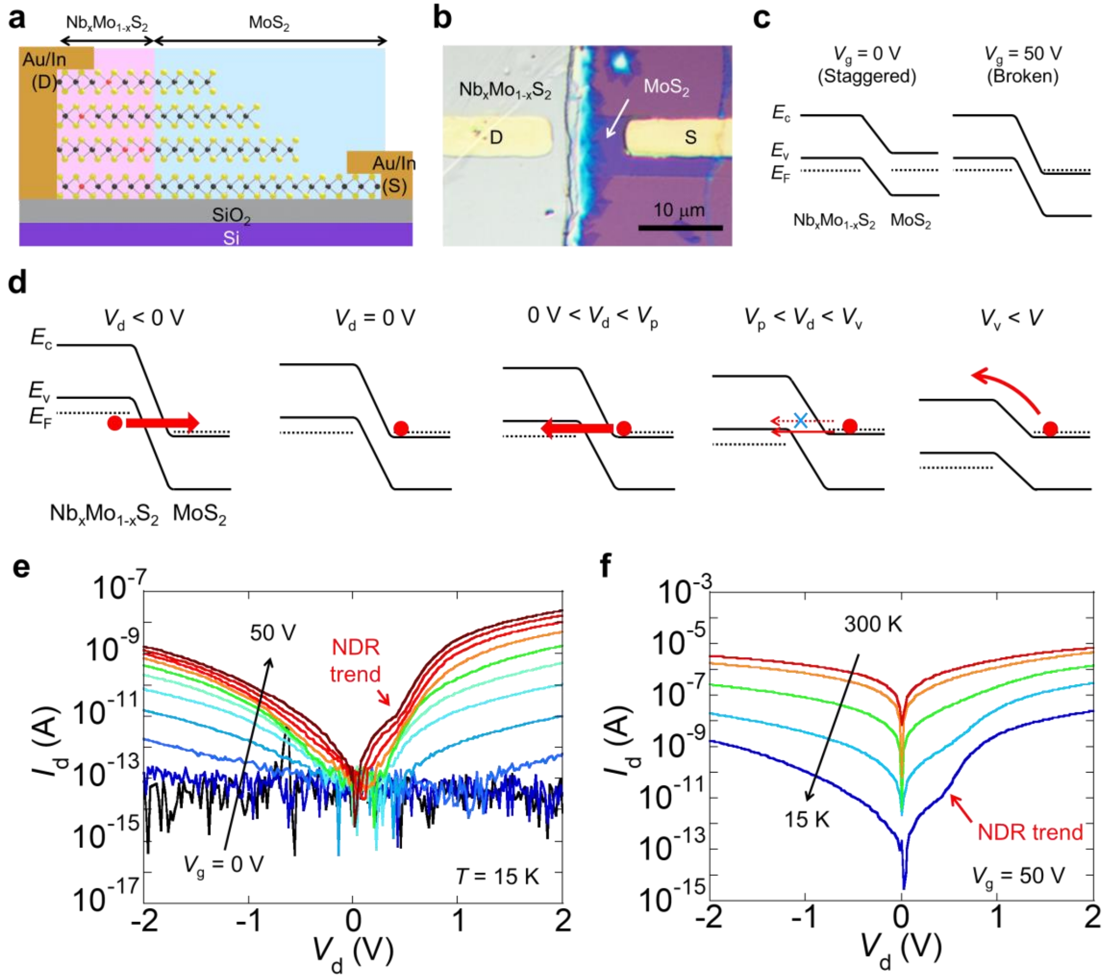

Figure 3.15 (a) Schematic and (b) optical micrograph images of the multilayer $Nb_xMo_{1-x}S_2/MoS_2$ in-plane heterostructure device. (c) Energy band alignment of the $Nb_xMo_{1-x}S_2/MoS_2$ heterostructure for a staggered gap (V_g = 0 V) and a broken gap (V_g = 50 V). (d) Energy band diagrams of the $Nb_xMo_{1-x}S_2/MoS_2$ heterostructure under various drain bias conditions. (e) I_d-V_d curves of the $Nb_xMo_{1-x}S_2/MoS_2$ heterostructure at different V_g and 15 K. The voltage step in V_g is 5 V. (f) Temperature-dependent I_d-V_d curves of the $Nb_xMo_{1-x}S_2/MoS_2$ heterostructure at V_g = 50 V (15, 50, 100, 200, and 300 K).

We also investigated the I_d-V_d curves at $V_g > 50$ V and low temperatures and the temperature-dependent transfer characteristics. Figure 3.16a shows the I_d-V_d curves of the $Nb_xMo_{1-x}S_2/MoS_2$ device at $V_g = 60$ and 80 V at 15 K. For $V_g = 60$ V, the NDR trend is observed for forward bias, which indicates the transition from the electron tunneling current to the diffusion current. For $V_g = 80$ V, however, the NDR trend disappears. Furthermore, for $V_g = 80$ V, the NDR trend is observed only at 50 K (Figure 3.16b). These results suggest that the holes in the bottom layer of $Nb_xMo_{1-x}S_2$ are dedoped by high positive gate voltages, and part of $Nb_xMo_{1-x}S_2$ becomes a nondegenerate semiconductor. Figure 3.16c shows the I_d-V_g curves of the same sample at reverse and forward bias and different temperatures. The device shows n-type behavior, which indicates that the transfer characteristics are dominated by MoS_2. The subthreshold swing (SS) averaged in the range of I_d from 10^{-11} to 10^{-10} A is estimated as a function of the temperature in Figure 3.16d. The large SS of approximately 3 V dec^{-1} derives from the low capacitance of thick SiO_2. For 200 K $< T <$ 300 K, SS exhibits a weak temperature dependence for reverse bias. In contrast, for forward bias, SS decreases with decreasing temperature. For $T <$ 200 K, at both forward and reverse bias, SS increases with decreasing temperature. The temperature dependences of SS for both reverse and forward bias are not consistent with those of ideal TFETs.[48, 53, 56, 114-117] This may be attributed to the interface states derived from the channel distortion on the SiO_2/Si substrate[34] and/or the high contact resistance at low temperature. To reduce these influences, the interface states and contact resistance must be reduced by using an atomically flat substrate and ohmic contact, respectively, which will be the focus of our future work.

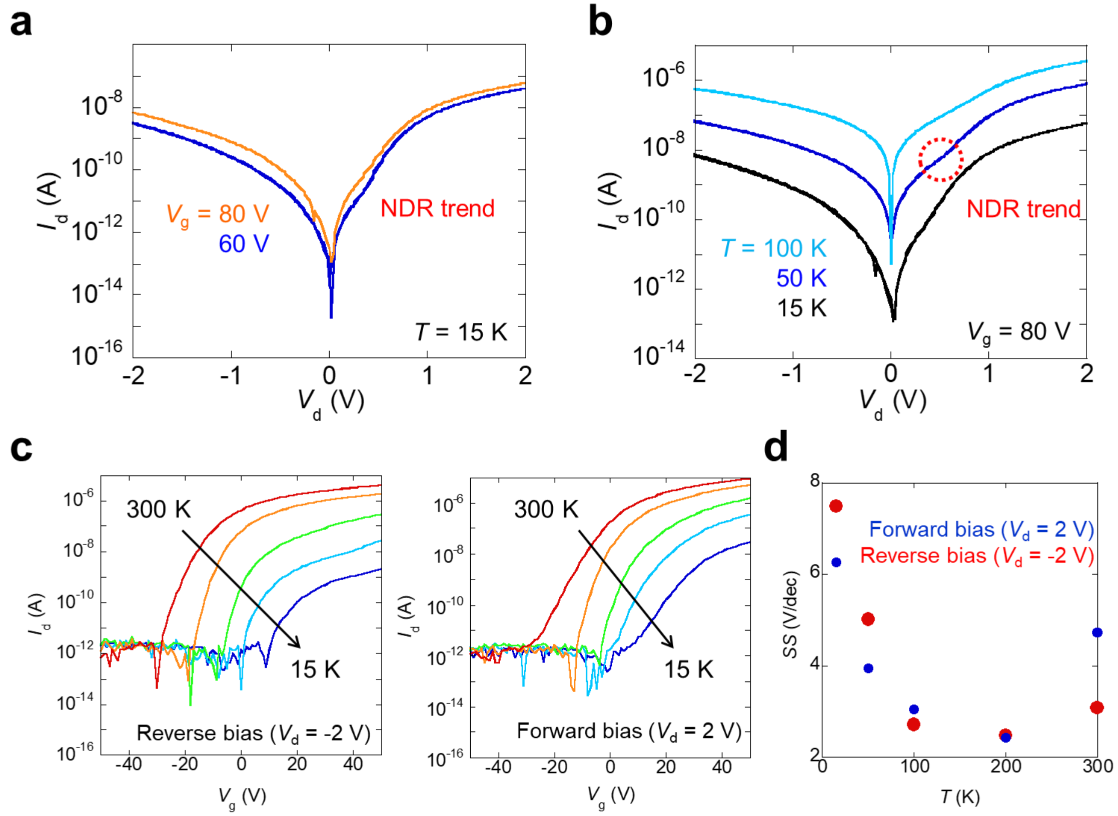

Figure 3.16. (a) I_d-V_d curves of the $Nb_xMo_{1-x}S_2/MoS_2$ heterostructure at V_g = 60 and 80 V at 15 K. (b) Temperature-dependent I_d-V_d curves of the $Nb_xMo_{1-x}S_2/MoS_2$ heterostructure at V_g = 80 V (15, 50, 100 K). (c) Temperature-dependent I_d-V_g curves of the $Nb_xMo_{1-x}S_2/MoS_2$ heterostructure for reverse (V_d = −2 V) and forward (V_d = 2 V) bias. (d) Temperature-dependent SS for reverse (V_d = −2 V) and forward (V_d = 2 V) bias, where SS is averaged in the range of I_d from 10^{-11} to 10^{-10} A.

We investigated the reproducibility of the NDR trend for another $Nb_xMo_{1-x}S_2/MoS_2$ sample with a Au (50 nm)/Ni (5 nm) electrode. Figure 3.17a shows the I_d-V_d curves of the $Nb_xMo_{1-x}S_2/MoS_2$ device at 100 K. The temperature-dependent I_d-V_d curves at V_g = 60 V are shown in Figure 3.17b. The NDR trend is also observed at high V_g and low temperature, as in Figure 3.15e,f. Figure 3.17c,d shows the temperature-dependent I_d-V_g curves and SS at different temperatures, where SS is averaged in the range of I_d from 10^{-11} to 10^{-10} A. The device shows a similar temperature dependence as that discussed in Figure 3.16c,d.

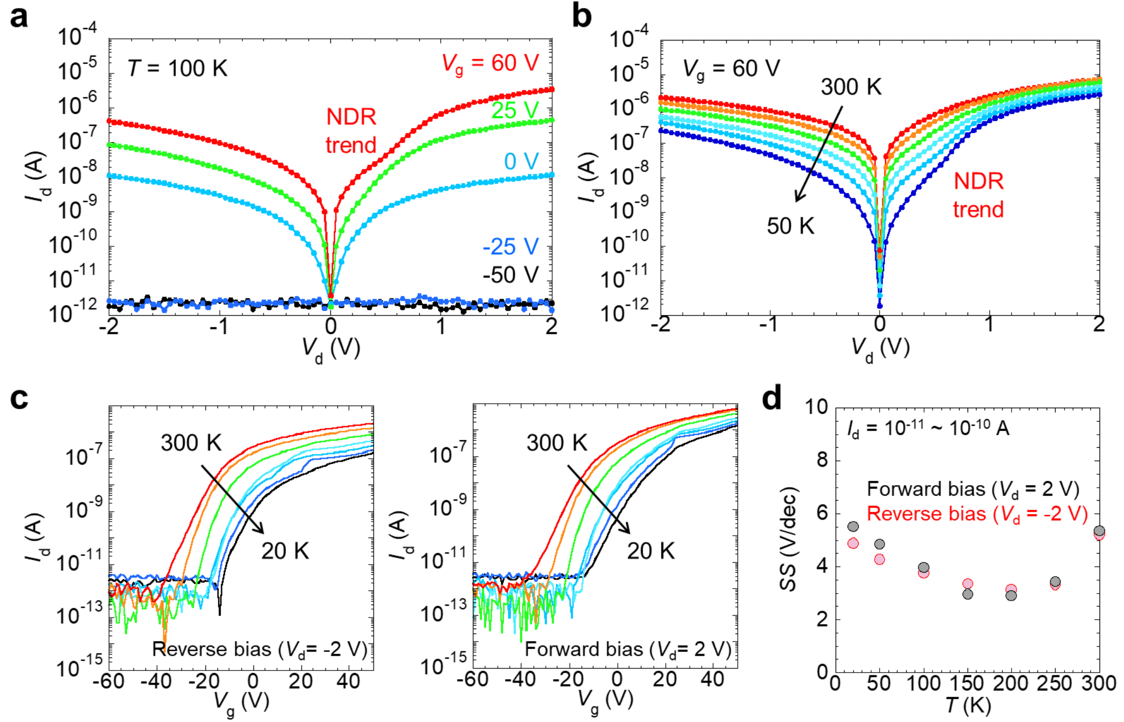

Figure 3.17. Temperature-dependent transport properties of another $Nb_xMo_{1-x}S_2/MoS_2$ sample with an Au (50 nm)/Ni (5 nm) electrode. (a) I_d-V_d curves at different V_g and 100 K. (b) Temperature-dependent I_d-V_d curves at V_g = 60 V (50, 100, 150, 200, 250, and 300 K). (c) Temperature-dependent I_d-V_g curves for reverse (V_d = −2 V) and forward (V_d = 2 V) bias (20, 50, 100, 150, 200, 250, and 300 K). (d) Temperature-dependent SS for reverse (V_d = −2 V) and forward (V_d = 2 V) bias, where SS is averaged in the range of I_d from 10^{-11} to 10^{-10} A.

Furthermore, we confirmed that NDR trend is not observed for the CVD-grown multilayer/monolayer MoS_2 junction. Figure 3.18a shows the optical micrograph image of the device of , which consists of multilayer and monolayer MoS_2 similar to the $Nb_xMo_{1-x}S_2/MoS_2$ device in Figure 3.15. Figure 3.18b shows the I_d-V_d curves of the multilayer/monolayer MoS_2 device at 15 K. Figure 3.18c shows the temperature-dependent I_d-V_d curves at V_g = 50 V. NDR trend is not observed even at 15 K and V_g = 50 V. These results support that the NDR trend in Figure 3.15e,f is derived from the electron tunneling at the $Nb_xMo_{1-x}S_2/MoS_2$ interface.

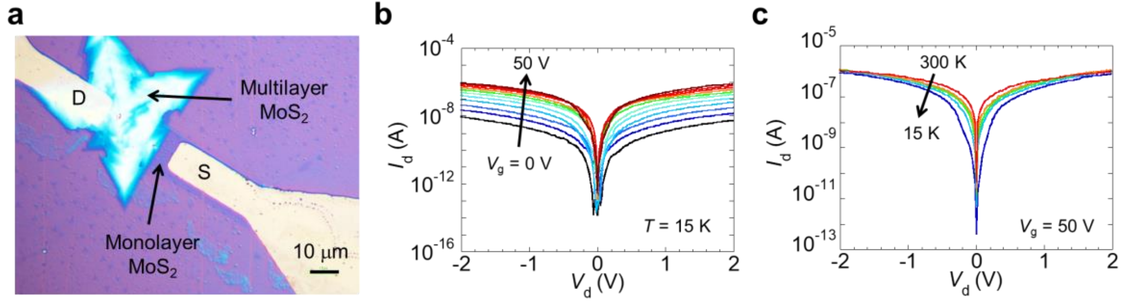

Figure 3.18. (a) Optical micrograph image of the multilayer/monolayer MoS_2 junction device. (b) I_d-V_d curves at different V_g (15 K). (b) Temperature-dependent I_d-V_d curves at V_g = 50 V (15, 50, 100, 200, and 300 K).

To understand the origin of the NDR trend, the experimental results were theoretically fitted using the following equation (Figure 3.19a):

$$\log_{10}(I_d) = \log_{10}\left\{I_p\left(\frac{V_d}{V_p}\right)exp\left(1-\frac{V_d}{V_p}\right)+I_0 exp\left(\frac{qV_d}{\eta k_B T}\right)\right\} \tag{3.5}$$

where I_p and V_p are the peak current and peak voltage of NDR, respectively (see section 1.2). I_0 and η are the saturation current and ideal factor, respectively (see section 1.1). The fitting parameters were $I_p = 3.97 \times 10^{-12}$ A, $V_p = 0.4$ V, $I_0 = 2.13 \times 10^{-14}$ A, and $\eta = 53.7$. Note that we used a least-squares method in the range of V_d = 0.3–0.7 V. The experimental results of the NDR trend can be reproduced by adding together the tunneling current and recombination current equations. This theoretical fitting also suggests that the tunneling current (Figure 3.19b) competes with the recombination current (Figure 3.19c) for the $Nb_xMo_{1-x}S_2/MoS_2$ sample. In addition, the ideal factor of $\eta = 53.7$ is much larger than the theoretical values in the Shockley-Read-Hall model for the recombination current ($\eta = 1$ to 2). The large ideal factor supports that the recombination probability is enhanced by trap-assisted tunneling into the shallow donor-like state coupled to the midgap level (Figure 3.19d).[118, 119] Moreover, the theoretical fitting cannot reproduce the experimental results at low voltages (V_d < 0.3 V) and high voltages (V_d > 0.7 V). This is probably because the influence of the contact resistance is dominant at low voltages. At high voltages, the resistances of $Nb_xMo_{1-x}S_2$ and MoS_2 themselves cannot be negligible.

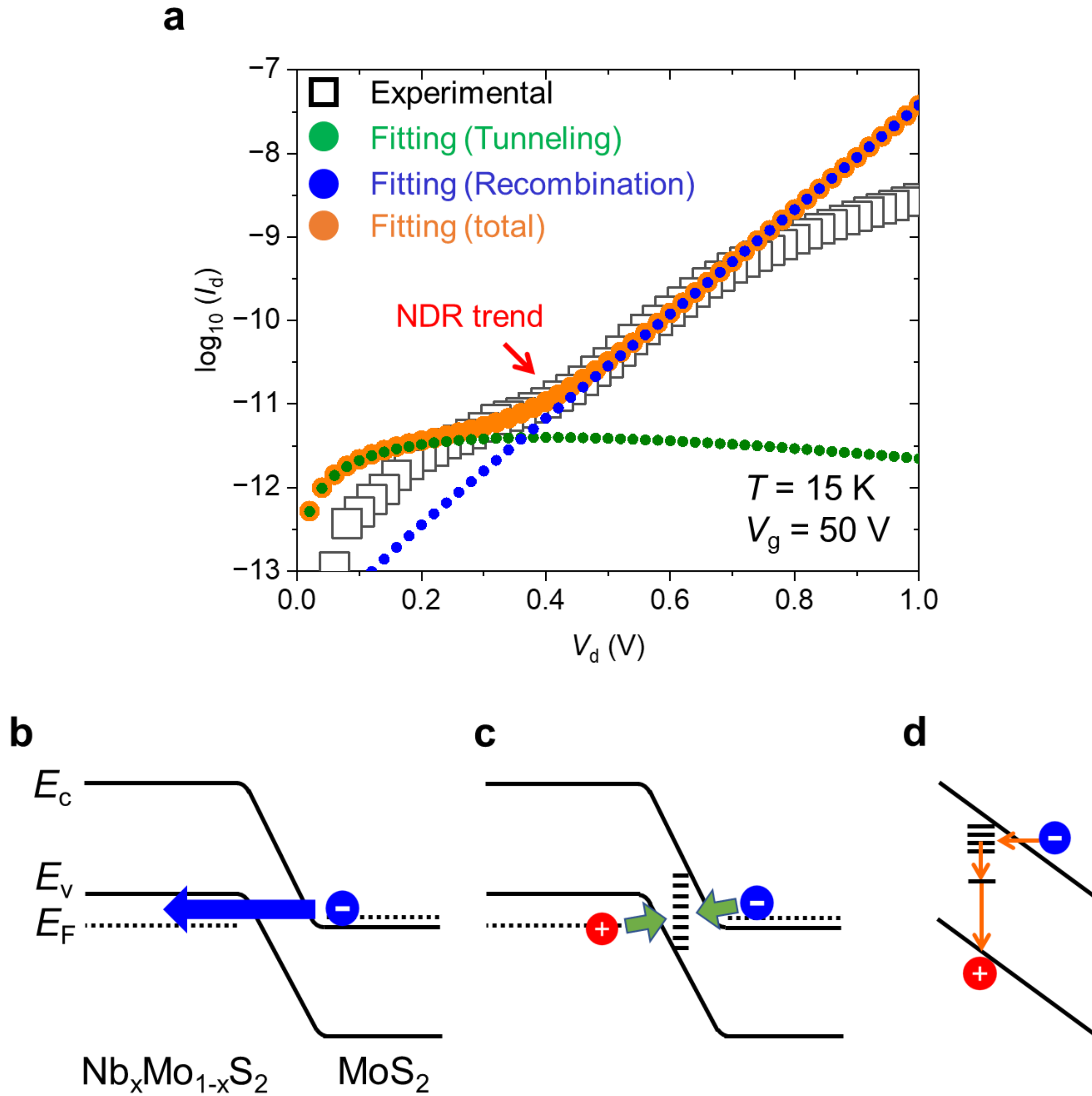

Figure 3.19. (a) Comparison of the experimental results and theoretical fitting of the NDR trend. The green, blue, and orange spheres are theoretical values of the tunneling current, recombination current, and their sum, respectively. Schematic illustrations of (b) electron tunneling and (c) the recombination process. (d) Trap-assisted tunneling into the shallow donor-like state coupled to the midgap level state at the heterointerface.

To understand the electronic states of $Nb_xMo_{1-x}S_2/MoS_2$, we carried out first-principles calculations. Figure 3.20a,b shows the calculation models and electronic band structures of MoS_2 and $Nb_xMo_{1-x}S_2$ ($x = 0.11$) monolayers. The calculation models are 6×6 supercells of monolayers because the computational costs of the multilayer structures are too huge. To clearly observe the doping effect by Nb substitution, we calculated the monolayers with higher Nb concentration than

that of the bulk crystal (~0.1%). We note that the DFT underestimate the band gap of insulating and semiconducting matters. Therefore, the conduction band edges obtained by DFT can provide a qualitative discussion on the band edge alignment of the heterostructures. Furthermore, the $Nb_xMo_{1-x}S_2$ is slightly strained because we conducted the full structural optimization. The lattice parameter of the $Nb_xMo_{1-x}S_2$ is 0.52 % larger than that of pristine MoS_2. However, the band structure modulation ascribed to the strain is not so large compared with that ascribed to the Nb-doping. As shown in Figure 3.20a,b, the valence band of MoS_2 is occupied by electrons, and the Fermi level is located at the valence band edge. In contrast, the Fermi level of $Nb_xMo_{1-x}S_2$ is located inside the valence band, which is consistent with the degenerate p-type behavior of the multilayer $Nb_xMo_{1-x}S_2$ used in the present study. These results are consistent with previous first-principles calculations for monolayer MoS_2 and $Nb_xMo_{1-x}S_2$.[120] From these results of monolayers, we can expect the formation of a staggered band alignment in MoS_2 and $Nb_xMo_{1-x}S_2$ heterostructures. To further confirm this tendency, we also calculated the in-plane $Nb_xMo_{1-x}S_2/MoS_2$ superlattice. Figure 3.20c shows the calculation model and the local electronic density of states (LDOS) of the monolayer in-plane $Nb_xMo_{1-x}S_2/MoS_2$ superlattice, where Nb is substitutionally doped in a 6 × 3 region of the 18 × 3 supercell. Here, the $Nb_xMo_{1-x}S_2$ region is slightly strained compared to the optimized structure, and the small lattice mismatch and the in-plane and out-of-plane dislocations have not been taken into consideration owing to huge computational costs. Both the valence and conduction bands of the $Nb_xMo_{1-x}S_2$ region shift to higher energy than those of the MoS_2 region, indicating the formation of a staggered gap band alignment. Note that the Fermi level of the MoS_2 region is located within the valence band, probably due to hole doping from adjacent Nb atoms.

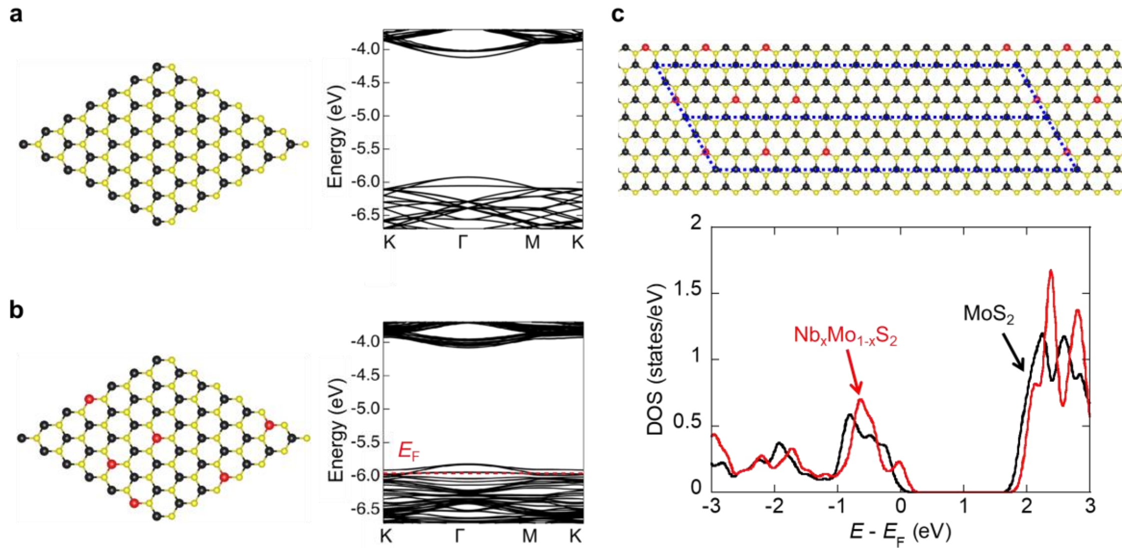

Figure 3.20 Structure models of the unit cell and calculated band structures of (a) undoped MoS_2 and (b) $Nb_xMo_{1-x}S_2$ (x = 0.11) monolayers. The black, yellow, and red circles correspond to Mo, S, and Nb atoms, respectively. (c) Structure model of the unit cell and LDOS of the $Nb_xMo_{1-x}S_2$ and MoS_2 regions in the $Nb_xMo_{1-x}S_2$ (x = 0.11)/MoS_2 in-plane superlattice. The area indicated by the blue dotted lines is the unit cell.

A similar tendency is observed for the LDOS of the $Nb_xMo_{1-x}S_2$/MoS_2 vertical heterostructure. It is noted that, despite the lattice strain in the Nb-substituted region, the LDOS of in-plane and vertical heterostructures (Figure 3.20c and 3.21) possess a qualitatively similar staggered band alignment as expected from the band structures of the undoped MoS_2 and $Nb_xMo_{1-x}S_2$ monolayers shown in Figure 3.20a,b. This indicates that the lattice strain by Nb doping does not have a substantial influence on the band alignment due to the small difference in lattice constants between $Nb_xMo_{1-x}S_2$ and MoS_2 monolayers after full structural optimization. The staggered band alignment in the monolayer in-plane superlattice is in agreement with the experimental findings as illustrated in Figure 3.15e, where the NDR trend can be observed in the multilayer $Nb_xMo_{1-x}S_2$/MoS_2 in-plane heterostructure by applying positive gate voltages. In other words, this indicates that the multilayer $Nb_xMo_{1-x}S_2$/MoS_2 in-plane heterostructure has a staggered band alignment before the gate voltage is applied. We note that the substantial number of atoms in the heterostructures makes quantitative discussions difficult in terms of accuracy, which require future efforts including large-scale calculations. Figure 3.21 shows the structure model and calculated LDOS of the vertical heterostructure of $Nb_xMo_{1-x}S_2$ (x = 0.11) and MoS_2 monolayers. Similar to the case of the in-plane heterostructure, the valence and conduction bands of $Nb_xMo_{1-x}S_2$ (x = 0.11) shift to higher energies than those of MoS_2. This suggests that the band alignment of the vertical heterostructure is also a staggered gap alignment. We note that the MoS_2 region in the vertical heterostructure has a finite LDOS around the Fermi level, and its Fermi level is closer to the valence band than that of monolayer MoS_2, where the Fermi level is located at the valence band edge (Figure 3.20a). This is probably because the MoS_2 region is also slightly hole-doped by the adjacent $Nb_xMo_{1-x}S_2$ (x = 0.11) as in the in-plane heterostructure (Figure 3.20c).

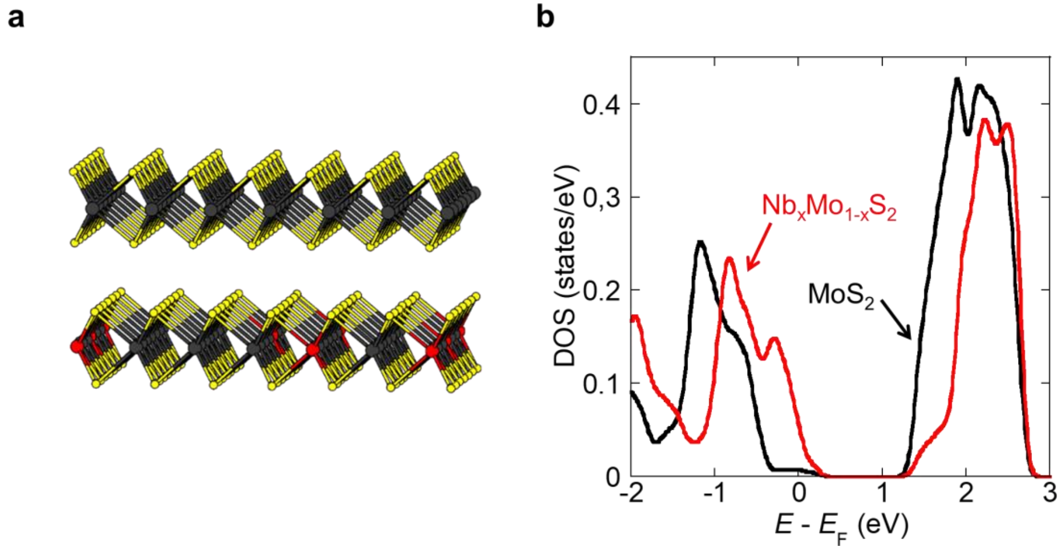

Figure 3.21. (a) Structure model and (b) LDOS of the vertical heterostructure of $Nb_xMo_{1-x}S_2$ (x = 0.11) and MoS_2 monolayers. The black, yellow, and red circles correspond to Mo, S, and Nb atoms, respectively.

3.4 Conclusions

We fabricated multilayer in-plane heterostructures of WSe_2/MoS_2 and $Nb_xMo_{1-x}S_2/MoS_2$ by using CVD. CVD growth of multilayer MoS_2 from the edges of WSe_2 and $Nb_xMo_{1-x}S_2$ was confirmed by Raman, PL, AFM, TEM, and HAADF-STEM observations. In addition to the in-plane heterostructures, the vertical growth of MoS_2 on the surface of WSe_2 was also confirmed. The $Nb_xMo_{1-x}S_2/MoS_2$ device exhibited an NDR trend at high positive gate voltages below 50 K, indicating that the band alignment changed from a staggered gap to a broken gap due to electron doping of MoS_2. First-principles calculations also supported that $Nb_xMo_{1-x}S_2/MoS_2$ without a gate voltage exhibited a staggered gap band alignment. We believe that this approach paves a way for the scalable growth of multilayer in-plane heterostructures. Actually, several works have already demonstrated the scalable growth of large-scale arrays based on in-plane monolayer heterostructures and multilayer heterophases by using the etching of wafer-scale films and re-growth process.[28, 85] Our findings constitute a significant achievement in constructing such novel in-plane heterostructures based on layered materials. The present results also show that CVD-grown multilayer in-plane heterostructures provide important access to TMDC-based energy-efficient devices such as tunnel diodes and TFETs.

Chapter 4:

Air-Stable and Efficient Electron Doping of Monolayer MoS_2 by Salt–Crown Ether Treatment

4.1 Introduction

Two-dimensional (2D) TMDCs have attracted much attention because of their excellent physical properties and potential applications in electronics and optoelectronics.[7-15] In particular, much effort has recently been devoted to investigate group-6 TMDC monolayers such as MoS_2 and WSe_2 and to elucidate their semiconducting properties, such as high on/off current ratio, high mobility and direct-bandgap nature.[20, 21, 121-124] To exploit the potential of TMDCs in devices such as light-emitting diodes and tunnelling field-effect transistors (FETs), developing a sophisticated technique for stable and highly efficient carrier doping is critical. Carrier doping in TMDCs has been carried out via several approaches, including elemental substitution, defect engineering, and chemical doping. Elemental substitution of group-6 TMDCs has been demonstrated by replacing group-6 transition metal elements (Mo and W) with group-5 and group-7 elements such as Nb and Re, respectively. [14, 24-28] Defect engineering has been carried out by the formation of chalcogen vacancies by hydrazine or plasma treatment,[125, 126] and the replacement of sulfur vacancies by chloride molecules.[127] Even though these techniques enable high tunability of the electrical conductivity of TMDCs, achieving both high-density doping and high mobility remains a major challenge because of impurity scattering by the substituted atoms or defects. In contrast, chemical doping is mainly based on surface charge transfer from a dopant to a semiconductor and has the advantage of not usually introducing defects into the crystal lattice. Chemical doping can thus increase the carrier density without seriously degrading the carrier mobility of TMDCs. The literature contains numerous reports of TMDC doping.[35-44] For example, Fang et al. reported degenerate n-type doping of few-layer MoS_2 and WSe_2 via vapor-phase doping of K, resulting in high electron densities of $\sim 1.0 \times 10^{13}$ cm^{-2} and $\sim 2.5 \times 10^{12}$ cm^{-2} for MoS_2 and WSe_2, respectively.[36] Air-stable n-type doping of few-layer MoS_2 with a high carrier density of $\sim 1.2 \times 10^{13}$ cm^{-2} was also achieved via solution-based doping of benzyl viologen (BV); the BV-doped MoS_2 exhibited stable transport properties in air for ~9 days.[37] Ji et al. achieved p- and n-type doping of monolayer WSe_2 using 4-nitrobenzenediazonium tetrafluoroborate and diethylenetriamine, respectively, and reported high carrier mobilities of 82 and 25 cm^2 V^{-1} s^{-1} for holes and electrons, respectively.[38] Despite such progress, further improvements that result in

highly stable and efficient doping methods are strongly desired for realizing future high-performance TMDC-based devices.

In the present work, we demonstrate the feasibility of using salt–crown ethers to achieve degenerate n-type, stable monolayer MoS_2. Crown ethers, which are cyclic oligomers consisting of several ethylene oxides, possess central cavities that form stable complexes with various metal ions and molecules.[128, 129] One type of crown ether, benzo-18-crown-6 in KOH/butanol solution, forms stable complexes with K^+ cations to produce OH^- anions, which can serve as an efficient n-type dopant for carbon nanotubes (CNTs).[128] We found that this approach is also effective at preparing highly doped monolayer MoS_2 with an electron density of 3.4×10^{13} cm^{-2}, which is similar to the previously reported electron density values for MoS_2 doped with other n-type dopants such as K and BV.[36, 37] Importantly, the electron-doped surfaces of MoS_2 are stable under ambient conditions for approximately 1 month. The electron doping by the crown ether complex is also supported by the first principles calculations. Furthermore, patterned doping is demonstrated to improve the contact resistance in MoS_2-based FETs.

4.2 Experimental Methods

Sample preparation

MoS_2 monolayers were grown on SiO_2 (285 nm)/Si substrates via salt-assisted CVD.[94, 95, 130] The SiO_2/Si substrate was placed at the center of a quartz tube, and MoO_2 powder (20–100 mg), KBr powder (5–11 mg) and sulfur flakes (2–3 g) were placed 1, 2–3 and 30 cm upstream from the tube center, respectively. The quartz tube was then filled with N_2 gas at flow rates of 150–275 sccm. The temperatures of the substrate and powders were gradually increased to 740–800 °C using an electric furnace. After the set-point temperature was reached, the sulfur flakes were heated at about 180–200 °C for 15 min using a second electric furnace to supply sulfur vapor to the substrate. After the growth, the quartz tube was immediately cooled using an electric fan. The same reaction conditions were used to grow WS_2, except that WO_3 powder (10 mg) was used instead of MoO_2, the amount of KBr was decreased to 5 mg, and the N_2 gas flow rate was increased to 300 sccm.

Device fabrication

FET devices were fabricated by photolithography. MoS_2 films on SiO_2/Si substrates were spin-coated with an AZ P1350 photoresist (Merck Performance Materials), followed by an exposure/development process, resistive thermal evaporation of Au (20 nm)/In (5 nm) electrodes (ULVAC, EX-200) and a liftoff process in acetone. The devices were then annealed at 200 °C under vacuum (~10^{-4} Pa) for 30 min before the transport measurements. To prepare the four-terminal devices for Hall effect measurements, the devices were plasma-etched for 1 min using a

Tergeo plasma cleaner (Pie Scientific) at 49 W under air. For the $n^+/i/n^+$ patterned doping, an SU-8 3005 photoresist (Kayaku Advanced Materials) was coated only in the middle of the channel using a lithography process. A similar $n^+/i/n^+$ patterned doping was achieved by combining an AZ P1350 photoresist coating applied only close to the S/D electrodes and water immersion after KOH/benzo-18-crown-6 doping.

Doping process and transport measurements

The carrier transport properties were measured using a probe station with voltage sources (KEITHLEY, 2614B) connected in the configuration. The doping process was performed by spin-coating butanol solution consisting of KOH/benzo-18-crown-6 (0.1–100 mM) onto the substrates. These chemicals were purchased from Wako Pure Chemical Industries (Japan) and Sigma-Aldrich (Japan) and were used as received without further purification. The Hall effect and the temperature dependence of the electrical resistance were measured with a physical property measurement system (PPMS, Quantum Design).

Raman and PL spectroscopy

The Raman and PL spectra of the samples were acquired at 532 nm excitation in a backscattering configuration using a microspectrometer (Renishaw, inVia).

Theoretical calculations

First-principles calculations of the undoped and doped monolayer MoS_2 were carried out using density functional theory (DFT), as implemented in the OpenMx package.[131] The generalized gradient approximation[100] with van der Waals correction[132, 133] was used for the exchange–correlation function. The electron–ion interaction was described by norm-conserving pseudopotentials.[134, 135] Pseudo-atomic orbitals (PAOs) centred on atomic sites were used as the basis function set.[136] The PAO basis functions were specified by C7.0-s2p2d1, H7.0- s2p1, O7.0-s2p2d1, K14.0-s4p3d2, M7.0-s3p2d2f1 and S7.0- s3p2d2f1. For example, C7.0-s2p2d1 indicates the PAOs of the carbon atom with a cutoff radius of 7.0 Bohr and with two s, two p, and one d components. The lattice constant of the monolayer MoS_2 was set to 3.16 Å.

4.3 Results and Discussions

Electrical and Optical Characteristics of Doped MoS_2

To investigate the carrier doping by crown ether in MoS_2, back-gated FETs with a MoS_2 channel were fabricated. Figure. 4.1a shows the schematic and optical micrographs of a representative MoS_2 FET. Triangular -shaped monolayer MoS_2 single crystals were grown on SiO_2/Si substrates via chemical vapor deposition (CVD). For n-type doping, the samples were spin-coated with a butanol solution of KOH/benzo-18-crown-6. In the solution, K^+ ions were captured by the cavities of the crown ether to form stable K+-ion complexes [K-crown]+OH− in butanol.[128]

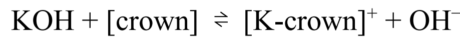

$$\mathrm{KOH} + [\mathrm{crown}] \rightleftharpoons [\mathrm{K\text{-}crown}]^+ + \mathrm{OH}^-$$

Similar to the case of CNTs, we reasonably expected electrons to transfer from OH− ions to MoS2; we also expected the transferred electrons to be stabilized by $[\text{K-crown}]^+$ cations adsorbed onto the MoS_2 surface, as illustrated in Figure 4.1b. The positive charges in the metal ion–benzocrown complexes would be delocalized over the benzene ring, thereby supporting further stabilization of negatively charged MoS_2.[128] Figure 4.1c,d presents the transfer and output curves for FETs with undoped MoS_2 and FETs with MoS_2 doped with KOH/benzo-18-crown-6 at concentrations from 0.1 to 100 mM, respectively. The undoped MoS_2 exhibits typical n-type semiconducting behavior; the corresponding FET exhibits an on/off current ratio of $\sim 10^5$ and a carrier mobility of $\sim 6.5\ \mathrm{cm^2\ V^{-1}\ s^{-1}}$ for applied gate voltages, V_{gs}, ranging from −50 to 50 V. Here, the carrier mobility was estimated using a parallel-plate model,[1] $\mu = [(\mathrm{d}I_d)/(\mathrm{d}V_{gs})][(L/V_{ds}C_{OX}W)]$, where L is the channel length, W is the channel width, I_d is the drain current, V_{ds} is the drain voltage, and $C_{OX} = 12.1\ \mathrm{nF\ cm^{-2}}$ is the gate capacitance of SiO_2 with a thickness of 285 nm and $V_{ds} = 1$ V. These characteristics are comparable to those reported in previous studies of CVD-grown monolayer MoS_2.[137] For the samples coated with 0.1 and 1 mM dopants, higher-concentration doping led to a shift of the threshold voltage (V_{th}) to the negative voltage side and to an increase of the drain current. Treatments with higher-concentration dopants resulted in a substantial increase in the off-current and in metallic gate dependence. Eventually, the on-current reached ~100 μA for the sample treated with the 100 mM dopant solution, which represents an increase of approximately two orders of magnitude compared with the on-current of the untreated sample. An increase in the on-current was also observed for monolayer WS_2 (Figure 4.2). Notably, the doped MoS_2 FETs were highly stable in ambient air. The transfer curves remained nearly unchanged even after 24 days of air exposure (Figure 4.1e). The drain current decreased by one order of magnitude between 24 and 41 days, but showed little change for the next 142 days.

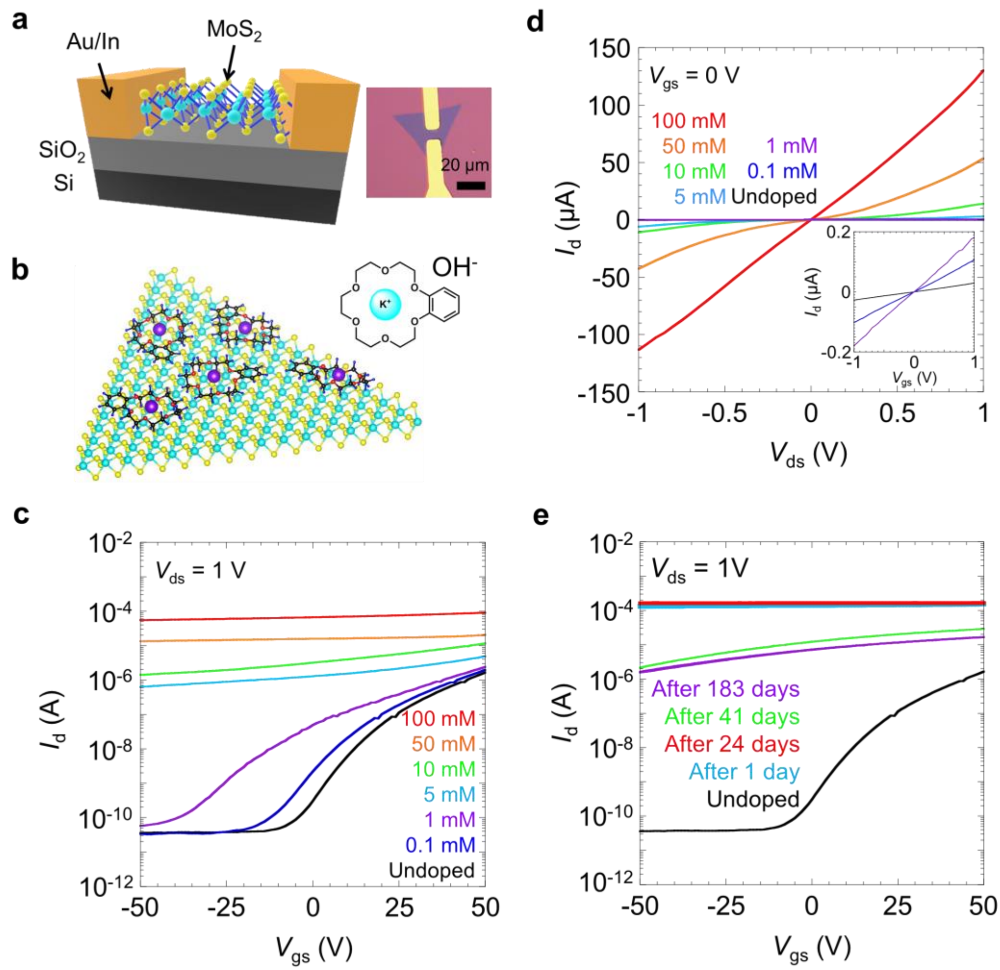

Figure 4.1 (a) Schematic and optical micrographs of the back-gated FET device. (b) Schematic model of the chemical doping using KOH/benzo-18- crown-6 for n-type doping. (c and d) The transfer (c) and output curves (d) of undoped and doped monolayer MoS_2 with different dopant concentrations from 0.1 to 100 mM. (e) Transfer characteristic curves of the device before and after doping. The doped device had been kept in air for 183 days.

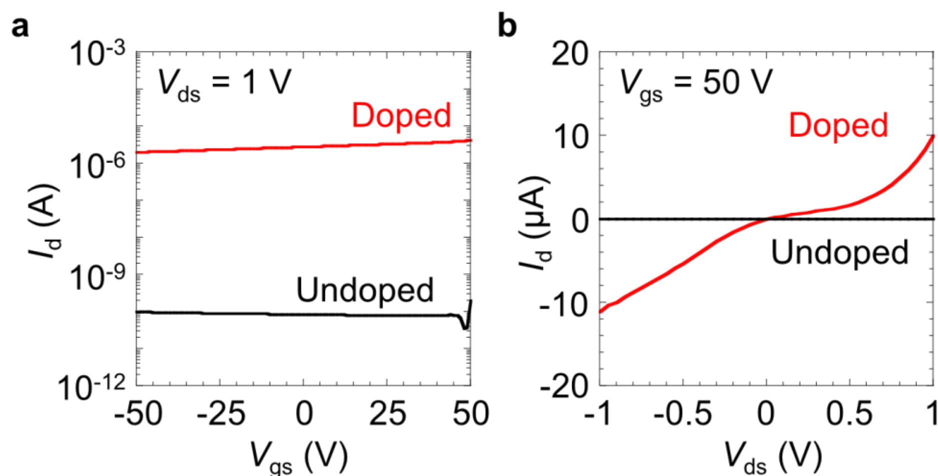

Figure 4.2 The transfer (a) and output (b) curves for undoped and doped monolayer WS_2 using 100 mM dopant solution.

The doped MoS_2 was further characterized by Raman and photoluminescence (PL) spectroscopy. Figure 4.3a shows the Raman spectra of monolayer MoS_2, recorded before and after the doping treatments with different concentrations of the dopants (0.1–100 mM). The two characteristic Raman peaks denoted by E' and A_1' are attributed to the in-plane and out-of-plane vibration modes of monolayer MoS_2, respectively.[105] As shown in Figure 4.3a, the E' mode (383 cm^{-1}) changes very little after the doping process, whereas the A_1' mode is downshifted by 6 cm^{-1}. This tendency is consistent with the results of an earlier report of electron doping of MoS_2 with BV[37] and suggests that the electron–phonon interaction is enhanced by an increase in the electron concentration.[138] The PL spectra show the emission peak from A exciton at 1.80 eV for the undoped MoS_2 (Figure 4.3b).[20] The A-exciton peak was substantially suppressed by the doping treatments and was completely quenched at above 1 mM with a downshift of the peak to 1.72 eV. Similar quenching of the A-exciton peak is also observed for the doping by electric field.[139] These PL changes can be explained by an increase of the emission from negatively charged trions as a result of the electron doping and the suppression of neutral exciton formation.[139, 140] These optical responses are consistent with the transport measurement results for electron-doped monolayer MoS_2. A good homogeneity of doping was confirmed by the Raman and PL spectra obtained at different locations (Figure 4.4). A small variation in the PL spectra is also observed for both the pristine and doped samples and can be explained by the local lattice strain induced due to the interaction with the growth substrate.[83]

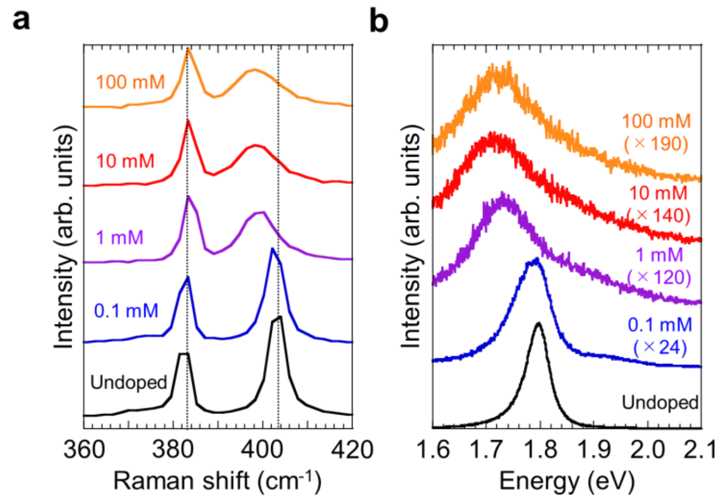

Figure 4.3 (a) Raman and (b) PL spectra of undoped and doped monolayer MoS_2 with different dopant concentrations from 0.1 to 100 mM.

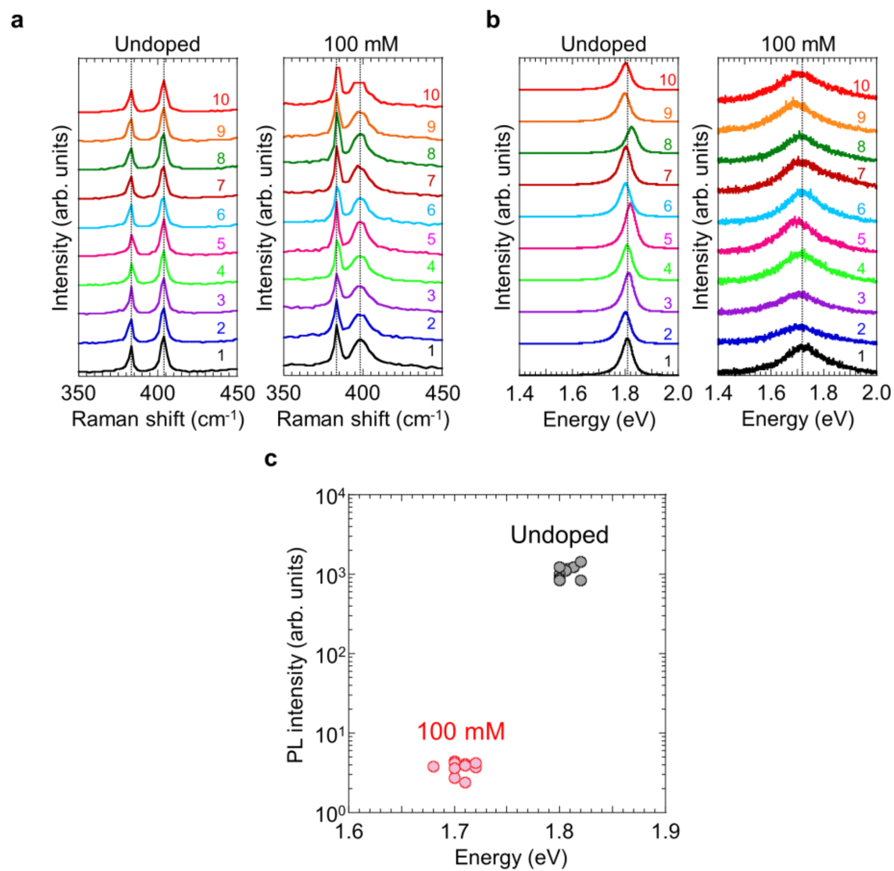

Figure 4.4 (a) Raman and (b) PL spectra of undoped and doped MoS_2 crystals taken at different 10 points. (c) Distributions of PL peak energy and intensity of undoped and 100 mM doped MoS_2 taken at different 10 points.

We also measured the Hall effect and the temperature dependence of the electrical resistance of the sample doped using the 100 mM dopant solution. The linear magnetic field dependence is consistent with the ordinary Hall voltage behaviour (Figure 4.5a). The 2D sheet carrier density, n_{2D}, is given by $n_{2D} = |(I_d B)/(e\Delta V_H)|$, where I_d is the drain current, e is the electric charge, B is the magnetic field strength and ΔV_H is the Hall voltage obtained after subtracting the offset Hall voltage at B = 0 T. The carrier mobility is given by $\mu = \sigma_{2D}/en_{2D}$, where $\sigma_{2D} = 5.6 \times 10^{-5}\ \Omega^{-1}$ is the sheet conductance of the present device. The values of n_{2D} and μ were estimated to be 3.4×10^{13} cm^{-2} and 10 cm^2 V^{-1} s^{-1}, respectively. The present n_{2D} value is as high as the value of ~10^{13} cm^{-2} previously reported for MoS_2 doped with potassium or BV.[36, 37] The high electron density also suggests that the Fermi level is located in the conduction band and that degenerate n-type doping is achieved by the crown ether complexes. Indeed, the temperature-dependent resistance of the doped MoS_2 indicates typical metallic behavior, where the resistance decreases with decreasing temperature (Figure 4.5b). These transport measurement results clearly indicate that effective electron doping was achieved by the crown ether complex-based coating process.

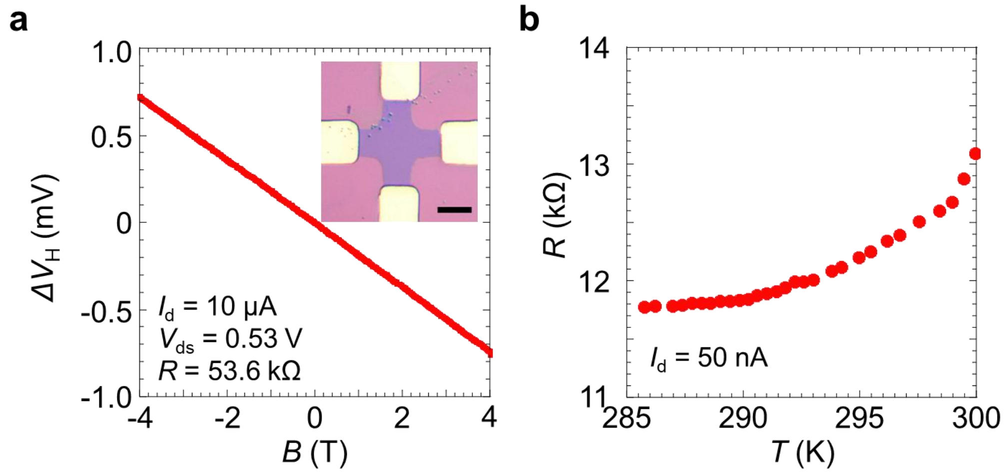

Figure 4.5 (a) Magnetic field dependence of the Hall voltage for the doped monolayer MoS_2 using 100 mM dopant solution at room temperature. The inset is an optical image of the sample. The scale bar is 10 μm. (b) Temperature dependence of the electrical resistance for the doped monolayer MoS_2 using 100 mM dopant solution.

First Principles Calculations of Electric States of Doped MoS_2

To understand the electronic states of monolayer MoS_2 with the K/benzo-18-crown-6 complex, we carried out first principles calculations. Figure 4.6a shows the changes in the electron distribution as a result of the adsorption of the dopant. The region of increased electron density (indicated in blue) is distributed over the MoS_2 layer and the region of decreased electron density (indicated in orange) is distributed in the crown ether complex (Figure 4.6b). Figure 4.6c shows

the electronic band structures. Monolayer MoS_2 has a direct bandgap of ~1.8 eV and its Fermi level is located in the middle of the bandgap. In contrast, the Fermi level of monolayer MoS_2 with the crown ether complex shifts to the conduction band. According to the density of states (Figure 4.6d), the energy level of the highest occupied molecular orbital (HOMO) for the K/benzo-18-crown-6 complex (having K atom components) becomes higher than the conduction- band minimum of monolayer MoS_2. This arrangement of energy levels means that one electron is transferred from the complex to MoS_2 per unit cell. Assuming that the density of K/benzo-18-crown-6 complex on the MoS_2 layer is the same as that used in the model for calculations, the electron density of monolayer MoS_2 is estimated to increase to $\sim 3 \times 10^{13}$ cm^{-2}. This estimation is consistent with the carrier density obtained from the Hall effect measurement (Figure 4.5a). These results also suggest that the doped electrons in MoS_2 are stabilized by the K/benzo-18-crown-6 complex after charge transfer from the OH^- ions to MoS_2.

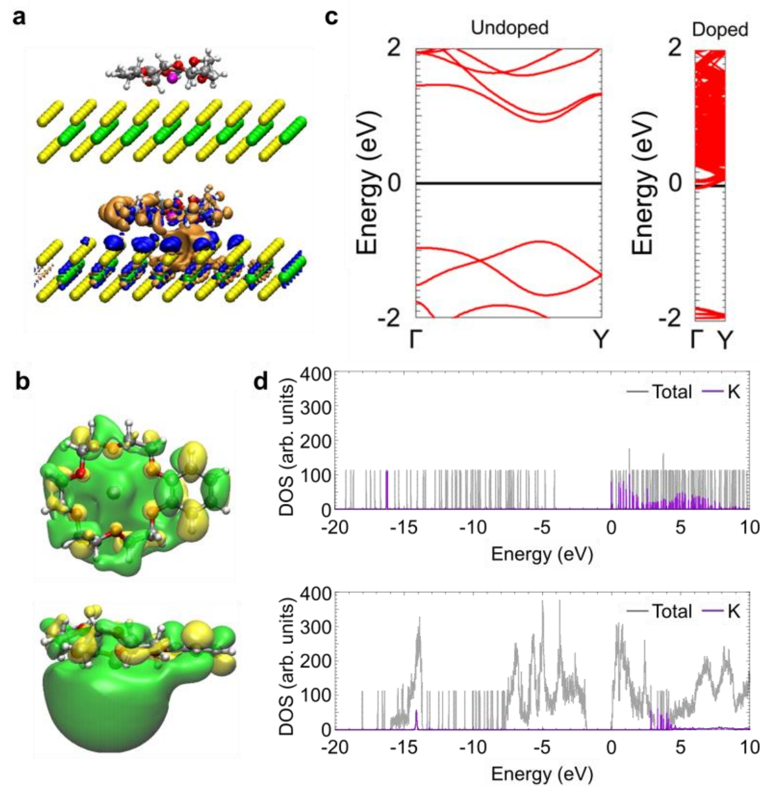

Figure 4.6 (a) Optimized atomic structure of monolayer MoS_2 with the K/benzo-18-crown-6 complex and changes in the electron distribution induced by the adsorption of the dopant. Gray, red, white, purple, yellow and green spheres represent C, O, H, K, S and Mo atoms, respectively. The blue (orange) color represents an increase (decrease) in the electron density. (b) Top and side views of the wave function of the HOMO for K/benzo-18-crown-6. The green and yellow colors indicate plus and minus contours, respectively. (c) Electronic band structures of undoped and doped monolayer MoS_2. (d) Total (gray) and K atom partial (purple) density of states (DOS) of

(top) K/benzo-18-crown-6 and (bottom) monolayer MoS_2 with K/benzo-18-crown-6.

Spatially-controlled doping of MoS_2 FETs

We demonstrated the spatially controlled n-type doping of partially masked MoS_2 FETs. After the electrodes were deposited, an epoxy-based photoresist was coated, using a lithography process, only in the middle of the channel. The MoS_2 between the source/drain (S/D) contacts and the photoresist were then doped, whereas the channel masked by the photoresist remained undoped (Figure 4.7a). Figure 4.7b–e shows the transfer and output curves of the device with the photoresist coating before and after the doping, respectively. The doped device clearly exhibits a higher on-current and a rapid increase in the current. Given the change in the channel area, the electron mobility increased from ~52 $cm^2\ V^{-1}\ s^{-1}$ to ~117 $cm^2\ V^{-1}\ s^{-1}$ as a result of the patterned doping. The patterned n-type doping was also carried out by partial removal of KOH/benzo-18-crown-6. The dopant was removed by immersing the samples in a solvent such as water or butanol. After the devices were immersed in these solvents, the gate dependence of the washed MoS_2 exhibited n-type behavior, with a high on/off current ratio, similar to the gate dependence of the undoped MoS_2 (Figure 4.8a,b). The patterned n-doping of the MoS_2 FETs was achieved via the reversible characteristics and the lithography process. After the doping, the photoresist was lithographically coated only close to the S/D electrodes. The dopant in the uncoated region was then removed by immersing the device in water for 1 min; the coated region remained in the doped state because of the protection afforded by the photoresist (Figure 4.8c). Figure 4.8d shows the transfer curves before and after the patterning. The on-current increased from ~6.6×10^{-7} to ~3.3×10^{-6} A. These results for both the partially doped devices, which are similar to the results for previously reported devices,[35-37] can be explained by a reduction in the contact resistance.

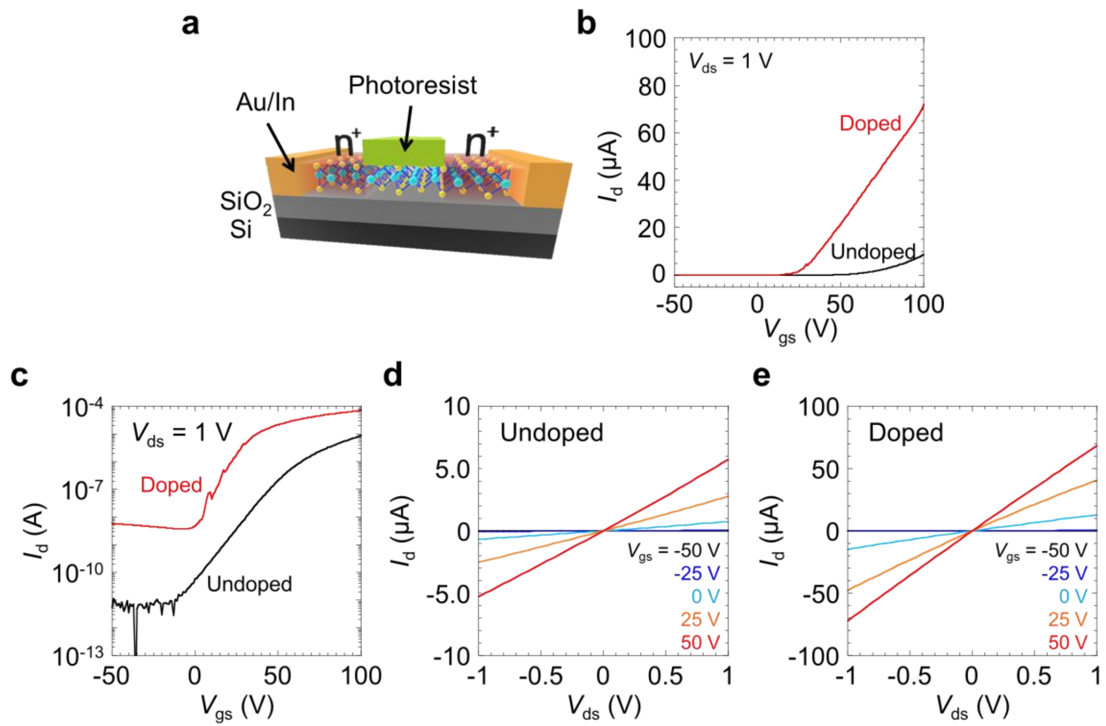

Figure 4.7 (a) Schematic diagram of an $n^+/i/n^+$ patterned device with a photoresist coating. (b) Transfer curves of the device with the photoresist coating before and after the doping using 100 mM dopant solution drawn on (b) linear and (c) logarithmic scale. Output curves of the device with a photoresist coating only in the middle of the channel: (d) before and (e) after the doping process using 100 mM dopant solution.

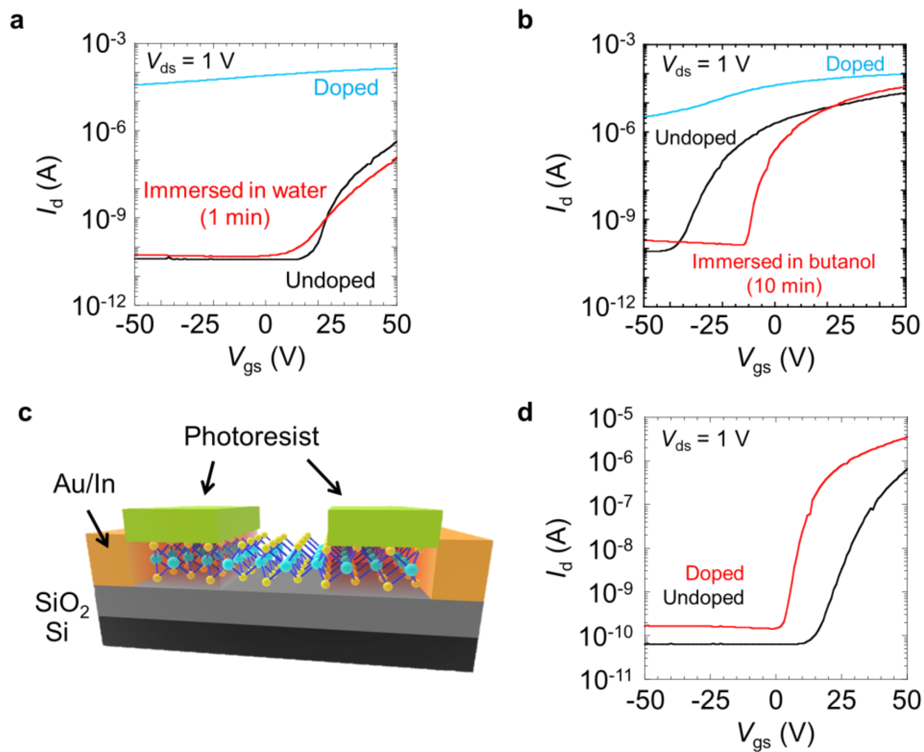

Figure 4.8. Reversible transfer characteristics of a KOH/benzo-18-crown-6-doped device using 100 mM (a) or 10mM (b) dopant solution. The transfer curves returned to those of undoped sample after immersion in water (a) or butanol (b). (c) Schematic (d) and transfer characteristics of the $n^+/i/n^+$ patterned device using 100 mM dopant solution with photoresist coating only close to the source and drain electrodes.

Comparison of Chemically Doping Methods of MoS_2

For discussion of the advantages of our doping method, the performance of TMDC-FET devices reported in the present work and in previous works are compared in Table 4.1.[36, 37, 41-44] The present doping method achieved relatively high electron density (~3.4×10^{13} cm^{-2}) and air stability (~24 days) compared with the methods used to prepare devices in the previous studies. Rosa et al. have reported that poly(vinyl-alcohol) doping with Al_2O_3 encapsulation results in a device with high stability in air for 30 days.[44] Such oxide films may provide an approach to improve the stability of the present n-type doped TMDCs through passivation.

	Dopants	Materials	Carrier density (cm^{-2})	Air stability
This work	KOH/benzo-18-crown-6	ML MoS_2	~3.4×10^{13}	~24 days
36	Potassium	FL MoS_2	~1.0×10^{13}	
37	Benzyl viologen	FL MoS_2	~1.2×10^{13}	~9 days
42	*p*-Toulene sufonic acid	FL MoS_2	~2.5×10^{12}	~10 days
41	Amorphous titanium suboxide	ML MoS_2	~7.4×10^{12}	~30 days
44	Poly(vinyl-alcohol)	FL MoS_2	~4.0×10^{12} (~8.0×10^{12} after annealing)	~16 hours (> 30 days with Al_2O_3 encapsulation)
43	Pentamethylrhodocene dimer	ML MoS_2	~2.4×10^{12}	

Table 4.1 Comparison of the carrier density and air stability of chemically doped monolayer (ML) and few-layer (FL) MoS_2 using different n-type dopants. The carrier densities were estimated by Hall effect for this work, by the electric-field effect with the parallel plate model for Ref. 36, 37, 44, and the shift of threshold voltage for Ref. 41, 42, 43.

4.4 Conclusions

We have demonstrated the efficient electron doping of CVD-grown monolayer MoS_2 with high stability under ambient conditions using KOH/benzo-18-crown-6 as a dopant. The electron doping achieved a high electron density of 3.4×10^{13} cm^{-2}, and the doped MoS_2 exhibited excellent stability in air for ~1 month. First-principles calculations indicated that electrons were

transferred from the K/benzo-18-crown-6 complex to the monolayer MoS_2. Patterned doping was also used to improve the contact resistance in MoS_2-based FETs. The present chemical doping strategy provides an effective method to control the electrical properties of TMDC materials for use in future device applications.

Chapter 5:

Conclusions

In this work, we presented multilayer in-plane heterostructures based on TMDCs fabricated by MoS_2 growth from the edges of exfoliated multilayer WSe_2 and $Nb_xMo_{1-x}S_2$. For the WSe_2/MoS_2 heterostructures, the epitaxial growth of MoS_2 and an abrupt composition change within *ca*. 2 nm around the heterointerface were confirmed. For, the $Nb_xMo_{1-x}S_2/MoS_2$ heterostructures, the NDR trend was observed at 15 K and $V_g = 50$ V, which indicates the electron tunneling current is at the heterointerface. Furthermore, we suggested that the electron tunneling current competes with the recombination current derived from interface trap states. These results provide important insights into advanced electronics based on TMDC in-plane heterostructures.

A chemical doping method was also developed for monolayer MoS_2. The monolayer MoS_2 doped by KOH/benzo-18-crown-6 exhibited a very high electron density of 3.4×10^{13} cm^{-2}, which suggested degenerate electron doping. In addition, this electron doping can achieve excellent stability in air for *ca*. 1 month. This doping method represents a significant step toward the future of low-consumption device applications such as TFETs.

Acknowledgements

During the three years after I entered the doctoral program at Tokyo Metropolitan University (TMU), I was able to conduct this research with guidance and cooperation from various people.

Assoc. Prof. Yasumitsu Miyata, thank you very much for taking me into your group. You were the big motivator that I decided to enter the doctoral program. The discussions with you were so exciting and fun for me. I appreciate that you always give me the best advice in various aspects such as the experimental methods, writing papers, making presentation slides, and my career path as a researcher. The way of thinking that you taught me is a tremendous asset for me. You also gave me opportunities to participate in various academic conferences, which were very good experiences for me to grow. Those three years were precious in my life. I would like express my sincere gratitude to you for your honesty during these years.

Asst. Prof. Yusuke Nakanishi, thank you very much for your guidance in a wide range of areas. You also gave me useful advice on writing papers and preparing presentations.

Mr. Takahiko Endo, I would like to express my sincere appreciation for the synthesis of the TMDC samples. You always gave me very high-quality TMDC samples grown by CVD. Your CVD techniques were a significant assist for my research.

Dr. Hong En Lim (currently at Saitama University) and Dr. Wenjin Zhang, I am thankful for your kind and thoughtful discussion of my works. The discussions with you were also very beneficial for practicing my English speaking.

Mr. Seiya Kawasaki (currently at The University of Tokyo), I would like to express my sincere thanks for performing the electronic transport measurements of multilayer in-plane heterostructures with me. Without your help, we would not have been able to demonstrate tunneling currents in the multilayer in-plane heterostructures.

Mr. Masahiko Kaneda, thank you for performing the electronic transport measurements of chemically-doped TMDC monolayers with me. Your support has been helpful in refining my work.

These works were able to be completed with the cooperation of many researchers. Dr. Zheng Liu from the National Institute of Advanced Industrial Science and Technology (AIST), thank you very much for conducting the atomic resolution HAADF-STEM observations. Prof. Susumu Okada, Asst. Prof. Mina Maruyama, and Asst. Prof. Yanlin Gao (University of Tsukuba), I would like to thank you for your excellent theoretical calculation of the electronic states of the in-plane heterostructures. Prof. Keiji Ueno (Saitama University), thank you for preparing the bulk TMDC crystals. Prof. Kazuhiro Yanagi (TMU), I appreciate your technical assistance with the plasma etching. Dr. Toshifumi Irisawa (AIST), thank you for your kind advice and technical

assistance with the device measurements. Prof. Kosuke Nagashio (The University of Tokyo), I would like to express my sincere gratitude for discussions with you on tunnel diodes and transistors. Dr. Yoshiyuki Nonoguchi (Kyoto Institute of Technology), I am thankful for preparation of the KOH/benzo-18-grown-6 solution. Asst. Prof. Jiang Pu and Prof. Taishi Takenobu (Nagoya University), I would like to thank you for the Hall-effect measurements of doped MoS_2 with KOH/benzo-18-crown-6. Dr. Mari Ohfuchi (Fujitsu Laboratories Ltd.), I appreciate the first-principles calculations of chemically doped MoS_2.

I am grateful to all the kind and helpful members of the NanoScience Research Lab. A special mention to our devoted secretaries, Ms. Tomomi Nonaka, Ms. Mayu Yamada and the staff in the department (especially, Ms. Mayumi Iwamoto), who have helped me in many aspects.

Finally, I would like to express my gratitude to my father and mother, who supported me for my university life and encouragement every day. I will make you be proud of me to give back your kindness and love.

Hiroto Ogura
December 2022

References

1. Sze, S. M., Semiconductor Devices: Physics and Technology. *John Wiley & Sons, New York,* **2002,** *2nd edn.*

2. Esaki, L., New Phenomenon in Narrow Germanium pn Junctions. *Phys. Rev.* **1958,** *109* (2), 603-604.

3. Sarkar, D.; Xie, X.; Liu, W.; Cao, W.; Kang, J.; Gong, Y.; Kraemer, S.; Ajayan, P. M.; Banerjee, K., A subthermionic tunnel field-effect transistor with an atomically thin channel. *Nature* **2015,** *526*, 91-95.

4. Ionescu, A. M.; Riel, H., Tunnel field-effect transistors as energy-efficient electronic switches. *Nature* **2011,** *479*, 329-337.

5. Knoch, J.; Appenzeller, J. In *A novel concept for field-effect transistors - the tunneling carbon nanotube FET*, 63rd Device Research Conference Digest, 2005. DRC '05., 20-22 June 2005; 2005; pp 153-156.

6. Knoch, J.; Mantl, S.; Appenzeller, J., Impact of the dimensionality on the performance of tunneling FETs: Bulk versus one-dimensional devices. *Solid-State Electron.* **2007,** *51*, 572-578.

7. Jariwala, D.; Sangwan, V. K.; Lauhon, L. J.; Marks, T. J.; Hersam, M. C., Emerging Device Applications for Semiconducting Two-Dimensional Transition Metal Dichalcogenides. *ACS Nano* **2014,** *8*, 1102-1120.

8. Tian, H.; Chin, M. L.; Najmaei, S.; Guo, Q.; Xia, F.; Wang, H.; Dubey, M., Optoelectronic devices based on two-dimensional transition metal dichalcogenides. *Nano Res.* **2016,** *9*, 1543-1560.

9. Ahmed, S.; Yi, J., Two-Dimensional Transition Metal Dichalcogenides and Their Charge Carrier Mobilities in Field-Effect Transistors. *Nano-Micro Lett.* **2017,** *9*, 50.

10. Wang, J.; Verzhbitskiy, I.; Eda, G., Electroluminescent Devices Based on 2D Semiconducting Transition Metal Dichalcogenides. *Adv. Mater.* **2018,** *30*, 1802687.

11. Hu, Z.; Wu, Z.; Han, C.; He, J.; Ni, Z.; Chen, W., Two-dimensional transition metal dichalcogenides: interface and defect engineering. *Chem. Soc. Rev.* **2018,** *47*, 3100-3128.

12. Wang, L.; Huang, L.; Tan, W. C.; Feng, X.; Chen, L.; Huang, X.; Ang, K.-W., 2D Photovoltaic Devices: Progress and Prospects. *Small Methods* **2018,** *2*, 1700294.

13. Liao, W.; Zhao, S.; Li, F.; Wang, C.; Ge, Y.; Wang, H.; Wang, S.; Zhang, H., Interface engineering of two-dimensional transition metal dichalcogenides towards next-generation electronic devices: recent advances and challenges. *Nanoscale Horiz.* **2020,** *5* (5), 787-807.

14. Loh, L.; Zhang, Z.; Bosman, M.; Eda, G., Substitutional doping in 2D transition

metal dichalcogenides. *Nano Res.* **2021,** *14* (6), 1668-1681.

15. Hoang, A. T.; Qu, K.; Chen, X.; Ahn, J.-H., Large-area synthesis of transition metal dichalcogenides via CVD and solution-based approaches and their device applications. *Nanoscale* **2021,** *13*, 615-633.

16. Guo, Y.; Robertson, J., Band engineering in transition metal dichalcogenides: Stacked versus lateral heterostructures. *Appl. Phys. Lett.* **2016,** *108*, 233104.

17. Johnson, V. R.; Vaughn, G. W., Investigation of the Mechanism of MoS_2 Lubrication in Vacuum. *J. Appl. Phys.* **1956,** *27*, 1173-1179.

18. Somoano, R. B.; Hadek, V.; Rembaum, A.; Samson, S.; Woollam, J. A., The alkaline earth intercalates of molybdenum disulfide. *J. Chem. Phys.* **1975,** *62*, 1068-1073.

19. Novoselov, K. S.; Jiang, D.; Schedin, F.; Booth, T. J.; Khotkevich, V. V.; Morozov, S. V.; Geim, A. K., Two-dimensional atomic crystals. *Proc. Natl. Acad. Sci.* **2005,** *102* (30), 10451-10453.

20. Mak, K. F.; Lee, C.; Hone, J.; Shan, J.; Heinz, T. F., Atomically Thin MoS_2: A New Direct-Gap Semiconductor. *Phys. Rev. Lett.* **2010,** *105*, 136805.

21. Radisavljevic, B.; Radenovic, A.; Brivio, J.; Giacometti, V.; Kis, A., Single-layer MoS_2 transistors. *Nat. Nanotechnol.* **2011,** *6*, 147-150.

22. Geim, A. K.; Grigorieva, I. V., Van der Waals heterostructures. *Nature* **2013,** *499*, 419-425.

23. Gong, Y.; Lin, J.; Wang, X.; Shi, G.; Lei, S.; Lin, Z.; Zou, X.; Ye, G.; Vajtai, R.; Yakobson, B. I.; Terrones, H.; Terrones, M.; Tay, Beng K.; Lou, J.; Pantelides, S. T.; Liu, Z.; Zhou, W.; Ajayan, P. M., Vertical and in-plane heterostructures from WS_2/MoS_2 monolayers. *Nat. Mater.* **2014,** *13*, 1135-1142.

24. Suh, J.; Park, T.-E.; Lin, D.-Y.; Fu, D.; Park, J.; Jung, H. J.; Chen, Y.; Ko, C.; Jang, C.; Sun, Y.; Sinclair, R.; Chang, J.; Tongay, S.; Wu, J., Doping against the Native Propensity of MoS_2: Degenerate Hole Doping by Cation Substitution. *Nano Lett.* **2014,** *14*, 6976-6982.

25. Jin, Y.; Zeng, Z.; Xu, Z.; Lin, Y.-C.; Bi, K.; Shao, G.; Hu, T. S.; Wang, S.; Li, S.; Suenaga, K.; Duan, H.; Feng, Y.; Liu, S., Synthesis and Transport Properties of Degenerate P-Type Nb-Doped WS_2 Monolayers. *Chem. Mater.* **2019,** *31*, 3534-3541.

26. Sasaki, S.; Kobayashi, Y.; Liu, Z.; Suenaga, K.; Maniwa, Y.; Miyauchi, Y.; Miyata, Y., Growth and optical properties of Nb-doped WS_2monolayers. *Appl. Phys. Express* **2016,** *9*, 071201.

27. Qin, Z.; Loh, L.; Wang, J.; Xu, X.; Zhang, Q.; Haas, B.; Alvarez, C.; Okuno, H.; Yong, J. Z.; Schultz, T.; Koch, N.; Dan, J.; Pennycook, S. J.; Zeng, D.; Bosman, M.; Eda, G., Growth of Nb-Doped Monolayer WS_2 by Liquid-Phase Precursor Mixing.

ACS Nano **2019,** *13*, 10768-10775.
28. Gao, H.; Suh, J.; Cao, M. C.; Joe, A. Y.; Mujid, F.; Lee, K.-H.; Xie, S.; Poddar, P.; Lee, J.-U.; Kang, K.; Kim, P.; Muller, D. A.; Park, J., Tuning Electrical Conductance of MoS_2 Monolayers through Substitutional Doping. *Nano Lett.* **2020,** *20*, 4095-4101.
29. Nakamura, K.; Nagamura, N.; Ueno, K.; Taniguchi, T.; Watanabe, K.; Nagashio, K., All 2D Heterostructure Tunnel Field-Effect Transistors: Impact of Band Alignment and Heterointerface Quality. *ACS Appl, Mater. Interfaces* **2020,** *12*, 51598-51606.
30. Chernikov, A.; Berkelbach, T. C.; Hill, H. M.; Rigosi, A.; Li, Y.; Aslan, B.; Reichman, D. R.; Hybertsen, M. S.; Heinz, T. F., Exciton Binding Energy and Nonhydrogenic Rydberg Series in Monolayer WS_2. *Phys. Rev. Lett.* **2014,** *113*, 076802.
31. Zhu, G.-J.; Xu, Y.-G.; Gong, X.-G.; Yang, J.-H.; Yakobson, B. I., Dimensionality-Inhibited Chemical Doping in Two-Dimensional Semiconductors: The Phosphorene and MoS_2 from Charge-Correction Method. *Nano Lett.* **2021,** *21* (15), 6711-6717.
32. Noh, J.-Y.; Kim, H.; Park, M.; Kim, Y.-S., Deep-to-shallow level transition of Re and Nb dopants in monolayer MoS_2 with dielectric environments. *Phys. Rev. B* **2015,** *92*, 115431.
33. Hong, J.; Hu, Z.; Probert, M.; Li, K.; Lv, D.; Yang, X.; Gu, L.; Mao, N.; Feng, Q.; Xie, L.; Zhang, J.; Wu, D.; Zhang, Z.; Jin, C.; Ji, W.; Zhang, X.; Yuan, J.; Zhang, Z., Exploring atomic defects in molybdenum disulphide monolayers. *Nat. Commun.* **2015,** *6*, 6293.
34. Fang, N.; Toyoda, S.; Taniguchi, T.; Watanabe, K.; Nagashio, K., Full Energy Spectra of Interface State Densities for n- and p-type MoS_2 Field-Effect Transistors. *Adv. Funct. Mater.* **2019,** *29*, 1904465.
35. Fang, H.; Chuang, S.; Chang, T. C.; Takei, K.; Takahashi, T.; Javey, A., High-Performance Single Layered WSe_2 p-FETs with Chemically Doped Contacts. *Nano Lett.* **2012,** *12*, 3788-3792.
36. Fang, H.; Tosun, M.; Seol, G.; Chang, T. C.; Takei, K.; Guo, J.; Javey, A., Degenerate n-Doping of Few-Layer Transition Metal Dichalcogenides by Potassium. *Nano Lett.* **2013,** *13*, 1991-1995.
37. Kiriya, D.; Tosun, M.; Zhao, P.; Kang, J. S.; Javey, A., Air-Stable Surface Charge Transfer Doping of MoS_2 by Benzyl Viologen. *J. Am. Chem. Soc.* **2014,** *136*, 7853-7856.
38. Ji, H. G.; Solís-Fernández, P.; Yoshimura, D.; Maruyama, M.; Endo, T.; Miyata, Y.; Okada, S.; Ago, H., Chemically Tuned p- and n-Type WSe_2 Monolayers with High Carrier Mobility for Advanced Electronics. *Adv. Mater.* **2019,** *31*, 1903613.
39. Iqbal, M. W.; Elahi, E.; Amin, A.; Aftab, S.; Aslam, I.; Hussain, G.; Shehzad,

M. A., A facile route to enhance the mobility of $MoTe_2$ field effect transistor via chemical doping. *Superlattices Microstruct.* **2020,** *147*, 106698.
40. Liu, X.; Qu, D.; Ryu, J.; Ahmed, F.; Yang, Z.; Lee, D.; Yoo, W. J., P-Type Polar Transition of Chemically Doped Multilayer MoS_2 Transistor. *Adv. Mater.* **2016,** *28*, 2345-2351.
41. Rai, A.; Valsaraj, A.; Movva, H. C. P.; Roy, A.; Ghosh, R.; Sonde, S.; Kang, S.; Chang, J.; Trivedi, T.; Dey, R.; Guchhait, S.; Larentis, S.; Register, L. F.; Tutuc, E.; Banerjee, S. K., Air Stable Doping and Intrinsic Mobility Enhancement in Monolayer Molybdenum Disulfide by Amorphous Titanium Suboxide Encapsulation. *Nano Lett.* **2015,** *15*, 4329-4336.
42. Andleeb, S.; Kumar Singh, A.; Eom, J., Chemical doping of MoS_2multilayer by p-toluene sulfonic acid. *Sci. Technol. Adv. Mater.* **2015,** *16*, 035009.
43. Zhang, S.; Hill, H. M.; Moudgil, K.; Richter, C. A.; Hight Walker, A. R.; Barlow, S.; Marder, S. R.; Hacker, C. A.; Pookpanratana, S. J., Controllable, Wide-Ranging n-Doping and p-Doping of Monolayer Group 6 Transition-Metal Disulfides and Diselenides. *Adv. Mater.* **2018,** *30*, 1802991.
44. Lockhart de la Rosa, C. J.; Nourbakhsh, A.; Heyne, M.; Asselberghs, I.; Huyghebaert, C.; Radu, I.; Heyns, M.; De Gendt, S., Highly efficient and stable MoS_2 FETs with reversible n-doping using a dehydrated poly(vinyl-alcohol) coating. *Nanoscale* **2017,** *9*, 258-265.
45. Lee, C.-H.; Lee, G.-H.; van der Zande, A. M.; Chen, W.; Li, Y.; Han, M.; Cui, X.; Arefe, G.; Nuckolls, C.; Heinz, T. F.; Guo, J.; Hone, J.; Kim, P., Atomically thin p–n junctions with van der Waals heterointerfaces. *Nat. Nanotechnol.* **2014,** *9*, 676-681.
46. Roy, T.; Tosun, M.; Cao, X.; Fang, H.; Lien, D.-H.; Zhao, P.; Chen, Y.-Z.; Chueh, Y.-L.; Guo, J.; Javey, A., Dual-Gated MoS_2/WSe_2 van der Waals Tunnel Diodes and Transistors. *ACS Nano* **2015,** *9*, 2071-2079.
47. Yan, R.; Fathipour, S.; Han, Y.; Song, B.; Xiao, S.; Li, M.; Ma, N.; Protasenko, V.; Muller, D. A.; Jena, D.; Xing, H. G., Esaki Diodes in van der Waals Heterojunctions with Broken-Gap Energy Band Alignment. *Nano Lett.* **2015,** *15*, 5791-5798.
48. Roy, T.; Tosun, M.; Hettick, M.; Ahn, G. H.; Hu, C.; Javey, A., 2D-2D tunneling field-effect transistors using WSe_2/$SnSe_2$ heterostructures. *Appl. Phys. Lett.* **2016,** *108*, 083111.
49. Shim, J.; Oh, S.; Kang, D.-H.; Jo, S.-H.; Ali, M. H.; Choi, W.-Y.; Heo, K.; Jeon, J.; Lee, S.; Kim, M.; Song, Y. J.; Park, J.-H., Phosphorene/rhenium disulfide heterojunction-based negative differential resistance device for multi-valued logic. *Nat. Commun.* **2016,** *7* (1), 13413.
50. Nourbakhsh, A.; Zubair, A.; Dresselhaus, M. S.; Palacios, T., Transport

Properties of a MoS_2/WSe_2 Heterojunction Transistor and Its Potential for Application. *Nano Lett.* **2016,** *16*, 1359-1366.

51. Yan, X.; Liu, C.; Li, C.; Bao, W.; Ding, S.; Zhang, D. W.; Zhou, P., Tunable $SnSe_2/WSe_2$ Heterostructure Tunneling Field Effect Transistor. *Small* **2017,** *13*, 1701478.

52. Liu, X.; Qu, D.; Li, H.-M.; Moon, I.; Ahmed, F.; Kim, C.; Lee, M.; Choi, Y.; Cho, J. H.; Hone, J. C.; Yoo, W. J., Modulation of Quantum Tunneling via a Vertical Two-Dimensional Black Phosphorus and Molybdenum Disulfide p–n Junction. *ACS Nano* **2017,** *11*, 9143-9150.

53. He, J.; Fang, N.; Nakamura, K.; Ueno, K.; Taniguchi, T.; Watanabe, K.; Nagashio, K., 2D Tunnel Field Effect Transistors (FETs) with a Stable Charge-Transfer-Type p^+-WSe_2 Source. *Adv. Electron. Mater.* **2018,** *4*, 1800207.

54. Fan, S.; Vu, Q. A.; Lee, S.; Phan, T. L.; Han, G.; Kim, Y.-M.; Yu, W. J.; Lee, Y. H., Tunable Negative Differential Resistance in van der Waals Heterostructures at Room Temperature by Tailoring the Interface. *ACS Nano* **2019,** *13*, 8193-8201.

55. Srivastava, P. K.; Hassan, Y.; Gebredingle, Y.; Jung, J.; Kang, B.; Yoo, W. J.; Singh, B.; Lee, C., Multifunctional van der Waals Broken-Gap Heterojunction. *Small* **2019,** *15*, 1804885.

56. Jeon, H. B.; Shin, G. H.; Lee, K. J.; Choi, S.-Y., Vertical-Tunneling Field-Effect Transistor Based on WSe_2-MoS_2 Heterostructure with Ion Gel Dielectric. *Adv. Electron. Mater.* **2020,** *6*, 2000091.

57. Huang, C.; Wu, S.; Sanchez, A. M.; Peters, J. J. P.; Beanland, R.; Ross, J. S.; Rivera, P.; Yao, W.; Cobden, D. H.; Xu, X., Lateral heterojunctions within monolayer $MoSe_2$–WSe_2 semiconductors. *Nat. Mater.* **2014,** *13*, 1096-1101.

58. Duan, X.; Wang, C.; Shaw, J. C.; Cheng, R.; Chen, Y.; Li, H.; Wu, X.; Tang, Y.; Zhang, Q.; Pan, A.; Jiang, J.; Yu, R.; Huang, Y.; Duan, X., Lateral epitaxial growth of two-dimensional layered semiconductor heterojunctions. *Nat. Nanotechnol.* **2014,** *9*, 1024-1030.

59. Yoo, Y.; Degregorio, Z. P.; Johns, J. E., Seed Crystal Homogeneity Controls Lateral and Vertical Heteroepitaxy of Monolayer MoS_2 and WS_2. *J. Am. Chem. Soc.* **2015,** *137*, 14281-14287.

60. Gong, Y.; Lei, S.; Ye, G.; Li, B.; He, Y.; Keyshar, K.; Zhang, X.; Wang, Q.; Lou, J.; Liu, Z.; Vajtai, R.; Zhou, W.; Ajayan, P. M., Two-Step Growth of Two-Dimensional $WSe_2/MoSe_2$ Heterostructures. *Nano Lett.* **2015,** *15*, 6135-6141.

61. Yoshida, S.; Kobayashi, Y.; Sakurada, R.; Mori, S.; Miyata, Y.; Mogi, H.; Koyama, T.; Takeuchi, O.; Shigekawa, H., Microscopic basis for the band engineering of $Mo_{1-x}W_xS_2$-based heterojunction. *Sci. Rep.* **2015,** *5*, 14808.

62. Chen, J.; Zhou, W.; Tang, W.; Tian, B.; Zhao, X.; Xu, H.; Liu, Y.; Geng, D.; Tan, S. J. R.; Fu, W.; Loh, K. P., Lateral Epitaxy of Atomically Sharp WSe_2/WS_2 Heterojunctions on Silicon Dioxide Substrates. *Chem. Mater.* **2016,** *28*, 7194-7197.
63. Kobayashi, Y.; Yoshida, S.; Sakurada, R.; Takashima, K.; Yamamoto, T.; Saito, T.; Konabe, S.; Taniguchi, T.; Watanabe, K.; Maniwa, Y.; Takeuchi, O.; Shigekawa, H.; Miyata, Y., Modulation of electrical potential and conductivity in an atomic-layer semiconductor heterojunction. *Sci. Rep.* **2016,** *6*, 31223.
64. Tsai, M.-L.; Li, M.-Y.; Retamal, J. R. D.; Lam, K.-T.; Lin, Y.-C.; Suenaga, K.; Chen, L.-J.; Liang, G.; Li, L.-J.; He, J.-H., Single Atomically Sharp Lateral Monolayer p-n Heterojunction Solar Cells with Extraordinarily High Power Conversion Efficiency. *Adv. Mater.* **2017,** *29*, 1701168.
65. Zhang, Z.; Chen, P.; Duan, X.; Zang, K.; Luo, J.; Duan, X., Robust epitaxial growth of two-dimensional heterostructures, multiheterostructures, and superlattices. *Science* **2017,** *357*, 788-792.
66. Li, M.-Y.; Pu, J.; Huang, J.-K.; Miyauchi, Y.; Matsuda, K.; Takenobu, T.; Li, L.-J., Self-Aligned and Scalable Growth of Monolayer WSe_2–MoS_2 Lateral Heterojunctions. *Adv. Funct. Mater.* **2018,** *28*, 1706860.
67. Sahoo, P. K.; Memaran, S.; Xin, Y.; Balicas, L.; Gutiérrez, H. R., One-pot growth of two-dimensional lateral heterostructures via sequential edge-epitaxy. *Nature* **2018,** *553*, 63-67.
68. Xie, S.; Tu, L.; Han, Y.; Huang, L.; Kang, K.; Lao Ka, U.; Poddar, P.; Park, C.; Muller David, A.; DiStasio Robert, A.; Park, J., Coherent, atomically thin transition-metal dichalcogenide superlattices with engineered strain. *Science* **2018,** *359*, 1131-1136.
69. Zhang, C.; Li, M.-Y.; Tersoff, J.; Han, Y.; Su, Y.; Li, L.-J.; Muller, D. A.; Shih, C.-K., Strain distributions and their influence on electronic structures of WSe_2–MoS_2 laterally strained heterojunctions. *Nat. Nanotechnol.* **2018,** *13*, 152-158.
70. Sahoo, P. K.; Memaran, S.; Nugera, F. A.; Xin, Y.; Díaz Márquez, T.; Lu, Z.; Zheng, W.; Zhigadlo, N. D.; Smirnov, D.; Balicas, L.; Gutiérrez, H. R., Bilayer Lateral Heterostructures of Transition-Metal Dichalcogenides and Their Optoelectronic Response. *ACS Nano* **2019,** *13*, 12372-12384.
71. Kobayashi, Y.; Yoshida, S.; Maruyama, M.; Mogi, H.; Murase, K.; Maniwa, Y.; Takeuchi, O.; Okada, S.; Shigekawa, H.; Miyata, Y., Continuous Heteroepitaxy of Two-Dimensional Heterostructures Based on Layered Chalcogenides. *ACS Nano* **2019,** *13*, 7527-7535.
72. Zhu, J.; Li, W.; Huang, R.; Ma, L.; Sun, H.; Choi, J.-H.; Zhang, L.; Cui, Y.; Zou, G., One-Pot Selective Epitaxial Growth of Large WS_2/MoS_2 Lateral and Vertical

Heterostructures. *J. Am. Chem. Soc.* **2020,** *142*, 16276-16284.
73. Jia, S.; Jin, Z.; Zhang, J.; Yuan, J.; Chen, W.; Feng, W.; Hu, P.; Ajayan, P. M.; Lou, J., Lateral Monolayer $MoSe_2$–WSe_2 p–n Heterojunctions with Giant Built-In Potentials. *Small* **2020,** *16*, 2002263.
74. Takahashi, Y.; Kobayashi, Y.; Wang, Z.; Ito, Y.; Ota, M.; Ida, H.; Kumatani, A.; Miyazawa, K.; Fujita, T.; Shiku, H.; Korchev, Y. E.; Miyata, Y.; Fukuma, T.; Chen, M.; Matsue, T., High-Resolution Electrochemical Mapping of the Hydrogen Evolution Reaction on Transition-Metal Dichalcogenide Nanosheets. *Angew. Chem.* **2020,** *59*, 3601-3608.
75. Okada, M.; Nagamura, N.; Matsumura, T.; Ando, Y.; Lu, A. K. A.; Okada, N.; Chang, W.-H.; Nakanishi, T.; Shimizu, T.; Kubo, T.; Irisawa, T.; Yamada, T., Growth of MoS_2–Nb-doped MoS_2 lateral homojunctions: A monolayer p–n diode by substitutional doping. *APL Mater.* **2021,** *9* (12), 121115.
76. Wada, N.; Pu, J.; Takaguchi, Y.; Zhang, W.; Liu, Z.; Endo, T.; Irisawa, T.; Matsuda, K.; Miyauchi, Y.; Takenobu, T.; Miyata, Y., Efficient and Chiral Electroluminescence from In-Plane Heterostructure of Transition Metal Dichalcogenide Monolayers. *Adv. Funct. Mater.* **2022,** *32*, 2203602.
77. Vu, V. T.; Phan, T. L.; Vu, T. T. H.; Park, M. H.; Do, V. D.; Bui, V. Q.; Kim, K.; Lee, Y. H.; Yu, W. J., Synthesis of a Selectively Nb-Doped WS_2–MoS_2 Lateral Heterostructure for a High-Detectivity PN Photodiode. *ACS Nano* **2022,** *16*, 12073-12082.
78. Pu, J.; Ou, H.; Yamada, T.; Wada, N.; Naito, H.; Ogura, H.; Endo, T.; Liu, Z.; Irisawa, T.; Yanagi, K.; Nakanishi, Y.; Gao, Y.; Maruyama, M.; Okada, S.; Shinokita, K.; Matsuda, K.; Miyata, Y.; Takenobu, T., Continuous Color-Tunable Light-Emitting Devices Based on Compositionally Graded Monolayer Transition Metal Dichalcogenide Alloys. *Adv. Mater.* **2022,** *34*, 2203250.
79. Nugera, F. A.; Sahoo, P. K.; Xin, Y.; Ambardar, S.; Voronine, D. V.; Kim, U. J.; Han, Y.; Son, H.; Gutiérrez, H. R., Bandgap Engineering in 2D Lateral Heterostructures of Transition Metal Dichalcogenides via Controlled Alloying. *Small* **2022,** *18*, 2106600.
80. Wang, J.; Li, Z.; Chen, H.; Deng, G.; Niu, X., Recent Advances in 2D Lateral Heterostructures. *Nano-Micro Lett.* **2019,** *11*, 48.
81. Chakraborty, S. K.; Kundu, B.; Nayak, B.; Dash, S. P.; Sahoo, P. K., Challenges and opportunities in 2D heterostructures for electronic and optoelectronic devices. *iScience* **2022,** *25*, 103942.
82. Ago, H.; Okada, S.; Miyata, Y.; Matsuda, K.; Koshino, M.; Ueno, K.; Nagashio, K., Science of 2.5 dimensional materials: paradigm shift of materials science

toward future social innovation. *Sci. Technol. Adv. Mater.* **2022,** *23*, 275-299.
83. Kobayashi, Y.; Sasaki, S.; Mori, S.; Hibino, H.; Liu, Z.; Watanabe, K.; Taniguchi, T.; Suenaga, K.; Maniwa, Y.; Miyata, Y., Growth and Optical Properties of High-Quality Monolayer WS_2 on Graphite. *ACS Nano* **2015,** *9*, 4056-4063.
84. Ueno, K., Introduction to the Growth of Bulk Single Crystals of Two-Dimensional Transition-Metal Dichalcogenides. *J. Phys. Soc. Jpn.* **2015,** *84*, 121015.
85. Xu, X.; Pan, Y.; Liu, S.; Han, B.; Gu, P.; Li, S.; Xu, W.; Peng, Y.; Han, Z.; Chen, J.; Gao, P.; Ye, Y., Seeded 2D epitaxy of large-area single-crystal films of the van der Waals semiconductor 2H $MoTe_2$. *Science* **2021,** *372*, 195-200.
86. Sutter, E.; Wang, J.; Sutter, P., Lateral Heterostructures of Multilayer GeS and SnS van der Waals Crystals. *ACS Nano* **2020,** *14*, 12248-12255.
87. Sutter, E.; Unocic, R. R.; Idrobo, J.-C.; Sutter, P., Multilayer Lateral Heterostructures of Van Der Waals Crystals with Sharp, Carrier–Transparent Interfaces. *Adv. Sci.* **2022,** *9*, 2103830.
88. Lee, G.-H.; Yu, Y.-J.; Cui, X.; Petrone, N.; Lee, C.-H.; Choi, M. S.; Lee, D.-Y.; Lee, C.; Yoo, W. J.; Watanabe, K.; Taniguchi, T.; Nuckolls, C.; Kim, P.; Hone, J., Flexible and Transparent MoS_2 Field-Effect Transistors on Hexagonal Boron Nitride-Graphene Heterostructures. *ACS Nano* **2013,** *7*, 7931-7936.
89. Das, S.; Chen, H.-Y.; Penumatcha, A. V.; Appenzeller, J., High Performance Multilayer MoS_2 Transistors with Scandium Contacts. *Nano Lett.* **2013,** *13*, 100-105.
90. Cui, X.; Lee, G.-H.; Kim, Y. D.; Arefe, G.; Huang, P. Y.; Lee, C.-H.; Chenet, D. A.; Zhang, X.; Wang, L.; Ye, F.; Pizzocchero, F.; Jessen, B. S.; Watanabe, K.; Taniguchi, T.; Muller, D. A.; Low, T.; Kim, P.; Hone, J., Multi-terminal transport measurements of MoS_2 using a van der Waals heterostructure device platform. *Nat. Nanotechnol.* **2015,** *10*, 534-540.
91. Lin, M.-W.; Kravchenko, I. I.; Fowlkes, J.; Li, X.; Puretzky, A. A.; Rouleau, C. M.; Geohegan, D. B.; Xiao, K., Thickness-dependent charge transport in few-layer MoS_2 field-effect transistors. *Nanotechnology* **2016,** *27*, 165203.
92. Jiang, J.; Zhang, Y.; Wang, A.; Duan, J.; Ji, H.; Pang, J.; Sang, Y.; Feng, X.; Liu, H.; Han, L., Construction of High Field-Effect Mobility Multilayer MoS_2 Field-Effect Transistors with Excellent Stability through Interface Engineering. *ACS Appl. Electron. Mater.* **2020,** *2*, 2132-2140.
93. Li, S.-L.; Wakabayashi, K.; Xu, Y.; Nakaharai, S.; Komatsu, K.; Li, W.-W.; Lin, Y.-F.; Aparecido-Ferreira, A.; Tsukagoshi, K., Thickness-Dependent Interfacial Coulomb Scattering in Atomically Thin Field-Effect Transistors. *Nano Lett.* **2013,** *13*, 3546-3552.

94. Kojima, K.; Lim, H. E.; Liu, Z.; Zhang, W.; Saito, T.; Nakanishi, Y.; Endo, T.; Kobayashi, Y.; Watanabe, K.; Taniguchi, T.; Matsuda, K.; Maniwa, Y.; Miyauchi, Y.; Miyata, Y., Restoring the intrinsic optical properties of CVD-grown MoS_2 monolayers and their heterostructures. *Nanoscale* **2019,** *11*, 12798-12803.

95. Ogura, H.; Kaneda, M.; Nakanishi, Y.; Nonoguchi, Y.; Pu, J.; Ohfuchi, M.; Irisawa, T.; Lim, H. E.; Endo, T.; Yanagi, K.; Takenobu, T.; Miyata, Y., Air-stable and efficient electron doping of monolayer MoS_2 by salt–crown ether treatment. *Nanoscale* **2021,** *13*, 8784-8789.

96. https://state-doc.readthedocs.io/en/latest/index.html.

97. Morikawa, Y.; Iwata, K.; Terakura, K., Theoretical study of hydrogenation process of formate on clean and Zn deposited Cu(111) surfaces. *Appl. Surf. Sci.* **2001,** *169-170*, 11-15.

98. Hohenberg, P.; Kohn, W., Inhomogeneous Electron Gas. *Phys. Rev.* **1964,** *136*, B864-B871.

99. Kohn, W.; Sham, L. J., Self-Consistent Equations Including Exchange and Correlation Effects. *Phys. Rev.* **1965,** *140*, A1133-A1138.

100. Perdew, J. P.; Burke, K.; Ernzerhof, M., Generalized Gradient Approximation Made Simple. *Phys. Rev. Lett.* **1996,** *77*, 3865-3868.

101. Vanderbilt, D., Soft self-consistent pseudopotentials in a generalized eigenvalue formalism. *Phys. Rev. B* **1990,** *41*, 7892-7895.

102. Otani, M.; Sugino, O., First-principles calculations of charged surfaces and interfaces: A plane-wave nonrepeated slab approach. *Phys. Rev. B* **2006,** *73*, 115407.

103. Maruyama, M.; Nagashio, K.; Okada, S., Influence of Interlayer Stacking on Gate-Induced Carrier Accumulation in Bilayer MoS2. *ACS Appl. Electron. Mater.* **2020,** *2*, 1352-1357.

104. Zhou, D.; Shu, H.; Hu, C.; Jiang, L.; Liang, P.; Chen, X., Unveiling the Growth Mechanism of MoS_2 with Chemical Vapor Deposition: From Two-Dimensional Planar Nucleation to Self-Seeding Nucleation. *Cryst. Growth Des.* **2018,** *18*, 1012-1019.

105. Lee, C.; Yan, H.; Brus, L. E.; Heinz, T. F.; Hone, J.; Ryu, S., Anomalous Lattice Vibrations of Single- and Few-Layer MoS_2. *ACS Nano* **2010,** *4*, 2695-2700.

106. Yamashita, S.; Kikkawa, J.; Yanagisawa, K.; Nagai, T.; Ishizuka, K.; Kimoto, K., Atomic number dependence of Z contrast in scanning transmission electron microscopy. *Sci. Rep.* **2018,** *8*, 12325.

107. Dickinson, R. G.; Pauling, L., THE CRYSTAL STRUCTURE OF MOLYBDENITE. *J. Am. Chem. Soc.* **1923,** *45*, 1466-1471.

108. Schutte, W. J.; De Boer, J. L.; Jellinek, F., Crystal structures of tungsten disulfide and diselenide. *J. Solid State Chem.* **1987,** *70*, 207-209.

109. Li, F.; Feng, Y.; Li, Z.; Ma, C.; Qu, J.; Wu, X.; Li, D.; Zhang, X.; Yang, T.; He, Y.; Li, H.; Hu, X.; Fan, P.; Chen, Y.; Zheng, B.; Zhu, X.; Wang, X.; Duan, X.; Pan, A., Rational Kinetics Control toward Universal Growth of 2D Vertically Stacked Heterostructures. *Adv. Mater.* **2019,** *31*, 1901351.

110. Kim, K. S.; Kim, K. H.; Ji, Y. J.; Yeom, G. Y., Layer Control of 2D-MoS_2 by Atomic Layer Etching and Its Device Characteristics. *ECS Trans.* **2018,** *86*, 69.

111. Amani, M.; Chin, M. L.; Birdwell, A. G.; O'Regan, T. P.; Najmaei, S.; Liu, Z.; Ajayan, P. M.; Lou, J.; Dubey, M., Electrical performance of monolayer MoS_2 field-effect transistors prepared by chemical vapor deposition. *Appl. Phys. Lett.* **2013,** *102*, 193107.

112. Wu, W.; De, D.; Chang, S.-C.; Wang, Y.; Peng, H.; Bao, J.; Pei, S.-S., High mobility and high on/off ratio field-effect transistors based on chemical vapor deposited single-crystal MoS_2 grains. *Appl. Phys. Lett.* **2013,** *102*, 142106.

113. Esaki, L.; Miyahara, Y., A new device using the tunneling process in narrow p-n junctions. *Solid-State Electron.* **1960,** *1*, 13-21.

114. Kim, S.; Myeong, G.; Shin, W.; Lim, H.; Kim, B.; Jin, T.; Chang, S.; Watanabe, K.; Taniguchi, T.; Cho, S., Thickness-controlled black phosphorus tunnel field-effect transistor for low-power switches. *Nat. Nanotechnol.* **2020,** *15*, 203-206.

115. Kim, S.; Myeong, G.; Park, J.; Watanabe, K.; Taniguchi, T.; Cho, S., Monolayer Hexagonal Boron Nitride Tunnel Barrier Contact for Low-Power Black Phosphorus Heterojunction Tunnel Field-Effect Transistors. *Nano Lett.* **2020,** *20*, 3963-3969.

116. Kim, S.; Myeong, G.; Park, J.; Jin, T.; Watanabe, K.; Taniguchi, T.; Lee, C.; Cho, S., Complementary Trilayer–Bulk Black Phosphorus Heterojunction Tunnel Field-Effect Transistor with Subthermionic Subthreshold Swing. *ACS Appl. Electron. Mater.* **2020,** *2*, 3491-3496.

117. Duong, N. T.; Park, C.; Nguyen, D. H.; Nguyen, P. H.; Tran, T. U.; Park, D. Y.; Lee, J.; Nguyen, D. A.; Oh, J. H.; Yu, Y. S.; Jeong, M. S., Gate-controlled $MoTe_2$ homojunction for sub-thermionic subthreshold swing tunnel field-effect transistor. *Nano Today* **2021,** *40*, 101263.

118. Schenk, A.; Krumbein, U., Coupled defect - level recombination: Theory and application to anomalous diode characteristics. *J. Appl. Phys.* **1995,** *78*, 3185-3192.

119. Breitenstein, O.; Altermatt, P.; Ramspeck, K.; Green, M. A.; Zhao, J.; Schenk, A. In *Interpretation of the Commonly Observed I-V Characteristics of C-SI Cells Having Ideality Factor Larger Than Two*, 2006 IEEE 4th World Conference on Photovoltaic Energy Conference, 7-12 May 2006; 2006; pp 879-884.

120. Dolui, K.; Rungger, I.; Das Pemmaraju, C.; Sanvito, S., Possible doping strategies for MoS_2 monolayers: An ab initio study. *Phys. Rev. B* **2013,** *88*, 075420.

121. Movva, H. C. P.; Rai, A.; Kang, S.; Kim, K.; Fallahazad, B.; Taniguchi, T.; Watanabe, K.; Tutuc, E.; Banerjee, S. K., High-Mobility Holes in Dual-Gated WSe_2 Field-Effect Transistors. *ACS Nano* **2015,** *9*, 10402-10410.
122. Sun, Y.; Wang, D.; Shuai, Z., Indirect-to-Direct Band Gap Crossover in Few-Layer Transition Metal Dichalcogenides: A Theoretical Prediction. *J. Phys. Chem. C* **2016,** *120*, 21866-21870.
123. Splendiani, A.; Sun, L.; Zhang, Y.; Li, T.; Kim, J.; Chim, C.-Y.; Galli, G.; Wang, F., Emerging Photoluminescence in Monolayer MoS_2. *Nano Lett.* **2010,** *10*, 1271-1275.
124. Pradhan, N. R.; Rhodes, D.; Zhang, Q.; Talapatra, S.; Terrones, M.; Ajayan, P. M.; Balicas, L., Intrinsic carrier mobility of multi-layered MoS_2 field-effect transistors on SiO_2. *Appl. Phys. Lett.* **2013,** *102* (12), 123105.
125. Chee, S.-S.; Oh, C.; Son, M.; Son, G.-C.; Jang, H.; Yoo, T. J.; Lee, S.; Lee, W.; Hwang, J. Y.; Choi, H.; Lee, B. H.; Ham, M.-H., Sulfur vacancy-induced reversible doping of transition metal disulfides via hydrazine treatment. *Nanoscale* **2017,** *9*, 9333-9339.
126. Tosun, M.; Chan, L.; Amani, M.; Roy, T.; Ahn, G. H.; Taheri, P.; Carraro, C.; Ager, J. W.; Maboudian, R.; Javey, A., Air-Stable n-Doping of WSe_2 by Anion Vacancy Formation with Mild Plasma Treatment. *ACS Nano* **2016,** *10*, 6853-6860.
127. Yang, L.; Majumdar, K.; Liu, H.; Du, Y.; Wu, H.; Hatzistergos, M.; Hung, P. Y.; Tieckelmann, R.; Tsai, W.; Hobbs, C.; Ye, P. D., Chloride Molecular Doping Technique on 2D Materials: WS_2 and MoS_2. *Nano Lett.* **2014,** *14*, 6275-6280.
128. Nonoguchi, Y.; Nakano, M.; Murayama, T.; Hagino, H.; Hama, S.; Miyazaki, K.; Matsubara, R.; Nakamura, M.; Kawai, T., Simple Salt-Coordinated n-Type Nanocarbon Materials Stable in Air. *Adv. Funct. Mater.* **2016,** *26*, 3021-3028.
129. Gokel, G. W.; Goli, D. M.; Minganti, C.; Echegoyen, L., Clarification of the hole-size cation-diameter relationship in crown ethers and a new method for determining calcium cation homogeneous equilibrium binding constants. *J. Am. Chem. Soc.* **1983,** *105*, 6786-6788.
130. Li, S.; Wang, S.; Tang, D.-M.; Zhao, W.; Xu, H.; Chu, L.; Bando, Y.; Golberg, D.; Eda, G., Halide-assisted atmospheric pressure growth of large WSe_2 and WS_2 monolayer crystals. *Appl. Mater. Today* **2015,** *1*, 60-66.
131. http://www.openmx-square.org/.
132. Grimme, S.; Antony, J.; Ehrlich, S.; Krieg, H., A consistent and accurate ab initio parametrization of density functional dispersion correction (DFT-D) for the 94 elements H-Pu. *J. Chem. Phys.* **2010,** *132*, 154104.
133. Grimme, S.; Ehrlich, S.; Goerigk, L., Effect of the damping function in dispersion corrected density functional theory. *J. Comput. Chem.* **2011,** *32*, 1456-1465.
134. Troullier, N.; Martins, J. L., Efficient pseudopotentials for plane-wave calculations.

Phys. Rev. B **1991,** *43*, 1993-2006.

135. Kleinman, L.; Bylander, D. M., Efficacious Form for Model Pseudopotentials. *Phys. Rev. Lett.* **1982,** *48*, 1425-1428.

136. Ozaki, T., Variationally optimized atomic orbitals for large-scale electronic structures. *Phys. Rev. B* **2003,** *67*, 155108.

137. van der Zande, A. M.; Huang, P. Y.; Chenet, D. A.; Berkelbach, T. C.; You, Y.; Lee, G.-H.; Heinz, T. F.; Reichman, D. R.; Muller, D. A.; Hone, J. C., Grains and grain boundaries in highly crystalline monolayer molybdenum disulphide. *Nat. Mater.* **2013,** *12*, 554-561.

138. Chakraborty, B.; Bera, A.; Muthu, D. V. S.; Bhowmick, S.; Waghmare, U. V.; Sood, A. K., Symmetry-dependent phonon renormalization in monolayer MoS_2 transistor. *Phys. Rev. B* **2012,** *85*, 161403.

139. Mak, K. F.; He, K.; Lee, C.; Lee, G. H.; Hone, J.; Heinz, T. F.; Shan, J., Tightly bound trions in monolayer MoS_2. *Nat. Mater.* **2013,** *12*, 207-211.

140. Mouri, S.; Miyauchi, Y.; Matsuda, K., Tunable Photoluminescence of Monolayer MoS_2 via Chemical Doping. *Nano Lett.* **2013,** *13*, 5944-5948.

List of Publications

Main publications

1. **H. Ogura**[†], S. Kawasaki[†], Z. Liu, T. Endo, M. Maruyama, Y. Gao, Y. Nakanishi, H. E. Lim, K. Yanagi, T. Irisawa, K. Ueno, S. Okada, K. Nagashio, and Y. Miyata, "Multilayer In-plane Heterostructures Based on Transition Metal Dichalcogenides for Advanced Electronics", *ACS Nano*, accepted ([†]equal contribution).

2. **H. Ogura**, M. Kaneda, Y, Nakanishi, Y. Nonoguchi, J. Pu, M. Ohfuchi, T. Irisawa, H. E. Lim, T. Endo, K. Yanagi, T. Takenobu, and Y. Miyata, "Air-stable and efficient electron doping of monolayer MoS_2 by salt–crown ether treatment", *Nanoscale*, **13**, 8784-8789 (2021, **Inside back cover**)

Reference publications

1. J. Pu, H. Ou, T. Yamada, N. Wada, H. Naito, **H. Ogura**, T. Endo, Z. Liu, T. Irisawa, K. Yanagi, Y. Nakanishi, Y. Gao, M. Maruyama, S. Okada, K. Shinokita, K. Matsuda, Y. Miyata, and T. Takenobu, "Continuous color‐tunable light‐emitting devices based on compositionally graded monolayer transition metal dichalcogenide alloys", *Adv. Mater.*, **34**, 2203250 (2022)

2. H. Kyakuno, **H. Ogura**, K. Matsuda, and Y. Maniwa, "Ice Nanoribbons Confined in Uniaxially Distorted Carbon Nanotubes", *J. Phys. Chem. C*, **122**, 18493-18500 (2018).

International conferences

1. **H. Ogura**, Y. Nonoguchi, T. Irisawa, T. Endo, H. E. Lim, Y. Nakanishi, and Y. Miyata, "Transport and Optical Properties of Salt-Coordinated Monolayer MoS_2", The 33rd International Microprocesses and Nanotechnology Conference, 2020-21-24, Online, Oral (2020/11)

2. **<u>H. Ogura</u>**, Y. Nonoguchi, T. Irisawa, T. Endo, H. E. Lim, Y. Nakanishi, and Y. Miyata, "Efficient Electron Doping of Monolayer MoS_2 by Salt-Crown Ether Treatment", Materials Research Society Fall Meeting, F.EL04.19.36, Online, Oral (2020/11)

3. **<u>H. Ogura</u>**, M. Kaneda, Y. Nakanishi, Y. Nonoguchi, J. Pu, M. Ohfuchi, T. Irisawa, H. E. Lim, T. Endo, K. Yanagi, T. Takenobu, and Y. Miyata, "Air-stable n-type doping of monolayer MoS_2 by crown-ether complexes", Recent Progress in Graphene and Two-dimensional Materials Research Conference (RPGR), Online, Poster (2021/10)

4. **<u>H. Ogura</u>**, M. Kaneda, Y. Nakanishi, Y. Nonoguchi, J. Pu, M. Ohfuchi, T. Irisawa, H. E. Lim, T. Endo, K. Yanagi, T. Takenobu, and Y. Miyata, "Air-stable, efficient *n*-type doping of MoS_2 by salt–crown ether treatment", The 34th International Microprocesses and Nanotechnology Conference, 27C-2-3, Online, Oral (2021/11)

Domestic meetings (in Japanese)

1. **<u>H. Ogura</u>**, Y. Murai, T. Irisawa, Z. Liu, H. Shimizu, H. E. Lim, Y. Nakanishi, T. Endo, R. Kitaura, and Y. Miyata., "Layer-selective dopant implantation in van der Waals heterostructures", The 59th Fullerenes-Nanotubes-Graphene General Symposium, 1P-23, Online, Poster, (2020/09)

2. **<u>H. Ogura</u>**, M. Kaneda, Y, Nakanishi, Y. Nonoguchi, J. Pu, M. Ohfuchi, T. Irisawa, H. E. Lim, T. Endo, K. Yanagi, T. Takenobu, and Y. Miyata, "Air-Stable, Efficient Electron Doping of Monolayer MoS_2 by Salt-Crown Ether Treatment", The 60th Fullerenes-Nanotubes-Graphene General Symposium, 2P-6, Online, Poster, (2021/03)

3. **<u>H. Ogura</u>**, Y. Nonoguchi, S. Zhang, Y. Nakanishi, H. E. Lim, R. Kitaura, K. Nagashio, and Y. Miyata, "N-type polar transition of p-type MoS_2 by chemical doping", The 61st Fullerenes-Nanotubes-Graphene General Symposium, 1P-67, Online, Poster, (2021/09)

4. **<u>H. Ogura</u>**, M. Kaneda, Y, Nakanishi, Y. Nonoguchi, J. Pu, M. Ohfuchi, T. Irisawa, H. E. Lim, T. Endo, K. Yanagi, T. Takenobu, and Y. Miyata, "Air-stable electron doping of monolayer MoS_2 by crown-ether complexes", The 82nd JSAP Autumn Meeting, 12a-N307-11, Online, Oral, (2021/09)

5. **H. Ogura**, S. Kawasaki, Z. Liu, T. Endo, Y. Nakanishi, H. E. Lim, K. Yanagi, T. Irisawa, K. Ueno, K. Nagashio, and Y. Miyata, "Fabrication and electronic transport properties of multilayer $Nb_xMo_{1-x}S_2/MoS_2$ in-plane heterostructures", The 62nd Fullerenes-Nanotubes-Graphene General Symposium, 3-11, Online, Oral, (2022/3)

6. **H. Ogura**, S. Kawasaki, Z. Liu, T. Endo, Y. Nakanishi, H. E. Lim, T. Irisawa, K. Nagashio, and Y. Miyata, "Fabrication and electronic transport properties of multilayer $Nb_xMo_{1-x}S_2/MoS_2$ in-plane heterostructures", The 69th JSAP Spring Meeting, 23a-E101-8, Online, Oral, (2022/03)

7. **H. Ogura**, S. Kawasaki, Z. Liu, T. Endo, M. Maruyama, Y. Gao, Y. Nakanishi, H. E. Lim, K. Yanagi, T. Irisawa, K. Ueno, S. Okada, K. Nagashio, and Y. Miyata, "Fabrication and characterization of multilayer in-plane heterostructures based on transition metal dichalcogenides", The 63rd Fullerenes-Nanotubes-Graphene General Symposium, 2P-9, Tokyo metropolitan Univ., Poster, (2022/9)

8. **H. Ogura**, S. Kawasaki, Z. Liu, T. Endo, M. Maruyama, Y. Gao, Y. Nakanishi, H. E. Lim, K. Yanagi, T. Irisawa, K. Ueno, S. Okada, K. Nagashio, and Y. Miyata, "Fabrication and characterization of tunnel diodes based on two-dimensional semiconductors", The 16th Joint Research Meeting of MEXT National Projects on Condensed-Matter Science, Online., Oral, (2022/11)

Award

1. Young Scientists Award, The 63rd Fullerenes-Nanotubes-Graphene General Symposium (2022/10)